Dissertation
submitted to the
Combined Faculties for the Natural Sciences and for Mathematics
of the Rupertus Carola University of
Heidelberg, Germany
for the degree of
Doctor of Natural Sciences

presented by

Diplom-Physicist: Zoltán Kovács
born in: Sopron, Hungary
Oral examination: 11th January 2006

Test of the Infrared Wide-field Camera OMEGA2000 and its Application for an Extragalactic Survey

Referees: Prof. Dr. Klaus Meisenheimer

Prof. Dr. Matthias Bartelmann

Zusammenfassung

OMEGA2000 ist eine Weitfeld-Nahinfrarot-Kamera, angebracht im Primaerfokus des 3.5m-Teleskopes auf Calar Alto. In der Fokalebene befindet sich ein 2k×2k HAWAII-2 CCD-Detektor, der in dem Wellenlängenbereich vom z- bis zum K-Band empfindlich ist. In dem ersten Teil der Dissertation beschreiben wir unsere Anstrengung, die Funktionsweise des HAWAII-2 Detektors zu optimieren. Dafür haben wir drei Exemplare aus der HAWAII-2-Familie getestet und miteinander verglichen. Um die Ergebnisse der Durchmusterung COMBO-17 mit Hilfe von OMEGA2000 zu höheren Rotverschiebungen zu erweitern, wurde eine tiefe Durchmusterung "MANOS", genannt auch COMBO-17+4, geplannt. Die gegenwärtig vorhandenen Daten beschränken das ursprüngliche Projekt auf die COMBO-17+2 Nahinfrarot-Durchmusterung. In dem zweiten Teil der Arbeit besprechen wir die ersten Ergebnisse von COMBO-17+2 NIR. Wir präsentieren hier die Rotverschiebungsverteilung der hellen Infrarotgalaxien im COMBO S11 Feld und analysieren die Anzahlentwicklung von vier Galaxientypen, die auf Grund von Ruhesystem-Farben definiert sind. Wir stellen einen Rückgang fest in der Zahl der alten elliptischen und der entwickelten Spiral-Galaxien bei der Rotverschiebung Dies steht in Ubereinstimmung mit früheren Ergebnissen. Für die "Extrem Roten Objekten" (EROs) im COMBO S11 Feld, die durch $R - H < 4$ ausgewählt wurden, beobachten wir ähnliche Rotverschiebungsverteilung und Häufungssignal, wie sie auch aus den anderen Durchmusterungen abgeleitet wurden. In unserer Auswahl von ERO's sind keine Galaxien mit heftiger Sternentstehung enthalten, was die Ergebnisse der frühere Beobachtungen bestaetigt. Die vollständige Abwesenheit der Sternentstehungssysteme kann auch eine Folge der ausgewählte Spektralschablonenbibliothek sein, die für die Multi-Farben Klassifikation in der COMBO-17+2 NIR eingesetzt wurde.

Abstract

OMEGA2000 is a prime-focus, near-infrared, wide-field camera, mounted on the 3.5m telescope at Calar Alto. The camera uses a 2k×2k HAWAII-2 Focal plane array with a sensitvity from z to K band. In the first part of the thesis, we discuss the work aimed at optimizing the operation of the HAWAII-2 detector installed in the camera. We tested the operation of three speciemen from the HAWAII-2 family and compared their performances with each other. The MANOS Deep Field Survey, called COMBO-17+4 NIR, is planned to to extend the results of the COMBO-17 project to higher redshifts by using this camera. The currently available data restricted the original project to the COMBO-17+2 NIR survey. In the second part of the thesis we discuss the results produced by COMBO-17+2 NIR. We present the redshift distribution of bright infrared galaxies observed in the COMBO S11 field and analyse the evolution of their number counts for four galaxy types defined by their restframe colors. We find a decline in the number of the old elliptical and evolved spiral galaxies at $z > 1.5$, whereas the acively star-forming galaxies become the dominating population at $z > 1$. This is in a broad agreement with earlier results. For Extremely Red Ojects (EROs) in the COMBO S11 field selected with $R - H < 4$, we measure similar redshift distribution and clustering signal to those derived in other surveys. Our ERO sample does not contain starburst galaxies, confirming the results of earlier observations. The total absence of the star-forming systems may also be attributed to the spectral template library used in the COMBO-17+2 NIR multi-color classification.

Contents

I Test of the wide-field Infrared Camera OMEGA2000 **11**

1 OMEGA2000 Instrument **13**

1.1 Cryostat . . . 14
1.2 Optics . . . 15
1.3 Baffle system . . . 16
1.4 Filter Mechanism . . . 17
1.5 Detector Mount . . . 18
1.6 The Readout Electronics and Control Software . . . 18

2 The HAWAII-2 Focal Plane Array **23**

2.1 Design and Operation of the HAWAII-2 FPA . . . 23
2.1.1 Infrared detectors . . . 24
2.1.2 Layout of the HAWAII-2 FPA . . . 26
2.1.3 Internal Architecture and Operation of the HAWAII-2 FPA . . . 27
2.2 The Readout modes of HAWAII-2 FPA . . . 29
2.2.1 The General Readout Scheme of the Detector . . . 30
2.2.2 Single Pixel Read (spr) . . . 32
2.2.3 Reset Level Read (rlr) . . . 32
2.2.4 Non-correlated Sampling or Single Correlated Read (rr) . . . 33
2.2.5 Correlated Double Sampling or Double Correlated Read (o2dcr) . . . 33
2.2.6 Correlated Double Sampling with Fast Reset (fcr) . . . 34
2.2.7 Line-interlaced Read (lir) . . . 35
2.2.8 Multiple End-point Read (mep) . . . 35
2.2.9 The choice of the readout modes for scientific operation . . . 37

3 Optimizing of the Operation of HAWAII-2 FPA **39**

3.1 Optimizing of the Detector Readout . . . 39
3.1.1 The Choice of the Output Mode . . . 40
3.1.2 Application of different modes for the idle cycles . . . 40
3.1.3 Fine tuning of the Analog Signals . . . 41
3.1.4 Optimal Design of the Basic Timing . . . 42
3.2 Improving of the Image Quality . . . 45
3.2.1 Transient Features in the Images . . . 45
3.2.2 Artifacts caused by internal Couplings . . . 47

4 Performance of the HAWAII-2 FPA **51**
4.1 Noise Properties of the Image Sensor . . . 51
4.1.1 Photon Shot Noise . . . 52
4.1.2 Reset Noise . . . 52
4.1.3 Readout Noise . . . 54
4.1.4 The Photon Transfer Curve . . . 55
4.1.5 Feedthrough and crosstalk . . . 60
4.1.6 Fixed Pattern Noise (FPN) . . . 60
4.1.7 Photo-Response Non-Uniformity and Quantum Efficiency . . . 61
4.2 Dark current . . . 65
4.2.1 Dark current shot noise . . . 67
4.2.2 Dark current non-uniformity . . . 67
4.3 Bad and hot pixels . . . 70
4.4 Linearity . . . 71

II Using OMEGA2000 for the MANOS Deep Field Survey **73**

5 The MANOS Deep Field Galaxy Survey: COMBO-17+4 NIR **75**
5.1 The COMBO-17 Project . . . 76
5.1.1 The COMBO-17 Survey . . . 77
5.1.1.1 Observations . . . 77
5.1.1.2 Photometry . . . 77
5.1.2 Multi-color Classification . . . 78
5.1.2.1 Classification Scheme . . . 78
5.1.2.2 The Classification Libraries . . . 79
5.1.3 Scientific Results of COMBO-17 and Other Deep Field Surveys . . . 80
5.1.4 Limitations of the COMBO-17 Survey . . . 82
5.2 The COMBO-17+4 NIR Project . . . 82
5.2.1 Motivations for COMBO-17+4 NIR Project . . . 82
5.2.2 Observations . . . 84
5.2.3 Data Reduction . . . 86
5.2.3.1 Bad Pixel Correction . . . 88
5.2.3.2 Dark Current Subtraction . . . 88
5.2.3.3 Correction of Mirror Reflection . . . 88
5.2.3.4 Flatfielding . . . 89
5.2.3.5 Sky Subtraction or Fringe Pattern Correction . . . 90
5.2.4 Photometry . . . 91
5.2.5 Multi-color Classification Including 2 NIR Bands . . . 91
5.2.5.1 Comparison of the Redshift Measurements . . . 92
5.2.5.2 High-redshift Galaxies with an Increase in the Redshift . . . 97
5.2.5.3 High-redshift Galaxies with a Decrease in the Redshift . . . 101
5.2.5.4 Galaxies with Large Redshift Variation . . . 106

5.2.5.5 Galaxies at $z \lesssim 1$ with Moderate Redshift Variation 108
5.2.6 Concluding Remarks 112

6 Scientific Results of the COMBO-17+2 NIR Project 115
6.1 Astrophysical Discussion of the Results 115
6.1.1 The Galaxy Sample 116
6.1.2 The Distribution of Infrared Bright Galaxies above $z \sim 1.1$ 117
6.1.3 Comparison to the Previous Results 125
6.2 Studying of Extremely Red Objects in the COMBO-17+2 NIR Project 126
6.2.1 ERO Selection 127
6.2.2 Testing of the Spectral Templates for EROs 128
6.2.3 The Redshift Distribution of EROs 131
6.2.4 The Nature of EROs 137

Introduction

Infrared Astronomy is the study of the infrared radiation emitted from objects in the Universe. All of the celestial objects radiate some amount of energy in the infrared wavelength regime. Studying the infrared part of their emitted energy provides interesting information on their physical properties and helps us to understand the astrophysical processes associated with them. The infrared regime lies between wavelengths of about 1 and 300 μm. It is usually divided into 3 spectral regions: near (0.7-4 μm), mid-infrared (4-40 μm), and far-infrared (40-350 μm).

Many objects in the universe which are much too cool and distant to be detected with visible light, can be studied in the infrared wavelength range. These include cool stars, clouds of dust particles around stars, nebulae, interstellar molecules, brown dwarfs, planets, and evolved galaxies. In space, there also are many regions which are hidden from optical telescopes because they are embedded in dense regions of gas and dust. However, infrared radiation can pass through dusty regions of space without being significantly scattered. Infrared astronomy can observe optically hidden parts of our galaxy and regions of newly forming stars.

In the infrared regime we can gather information about the early Universe and study the evolution of galaxies as well. As a result of the Big Bang, the universe is expanding and most of the galaxies within it are accelerating away from each other. This recession of galaxies away from the Milky Way causes a redshift in the in the wavelength of the light emitted from these galaxies. At large redshifts, all of the ultraviolet and much of the visible light is shifted into the infrared part of the observed spectrum. So the study of infrared light from these distant sources is important. Telescopes observing in infrared regime can locate more galaxies, which are at a sufficiently large distance as to be indetectable with visible light. Therefore infrared astronomy will provide a great deal of information on how and when the universe was formed and what the early universe was like. In addition, it allows us to observe the old stellar component in evolved massive elliptical galaxies. Such discoveries may help to find new constraints on the theories about galactic evolution. It is believed that the bulk of most galaxies is composed of cool stars. Infrared telescopes can see these cool stars very clearly since they emit more infrared than visible frequencies of light. Thus infrared astronomy will play a role in determining the mass of the universe.

Infrared detectors are also well suited to looking at distant objects, such as quasars. These unusual objects with incredibly high red shifts may be the most distant (and therefore the oldest) objects in the universe. Observing them in visible light is very difficult since the quasars' red shifts have stretched their visible light into the infrared part of the spectrum, but this makes them ideal targets for an infrared telescope. Both the determination of the universe's mass and the observation of quasars assist cosmologists in refining the big bang theory - the currently

accepted description of the evolution of the universe.

Unfortunately the Earth's atmosphere causes a problem for ground based infrared observations. The atmosphere lets visible light, most radio waves, and small wavelength ranges of infrared light through whereas the rest is absorbed by water vapor and carbon dioxide. The atmosphere itself radiates strongly in the infrared as well, often producing a more intensive infrared background noise than the light of the objects in space being observed. This atmospheric infrared emission peaks at a wavelength of about 10 microns. The observers can use only a few windows in the infrared wavelength regime with both high sky transparency and low sky emission. These windows, called J, H and K bands, are mainly at Near Infrared (NIR) wavelengths below 4 microns. All the ground based NIR observations are adapted to these windows and obtain information from only these wavelength intervals.

Astronomers in the 1970s began making observations of the sky using infrared detectors, but in order to produce an image they needed long exposures. Because of the small size and therefore the small field of view of the infrared sensors, they produced small pieces of mosaics that had to be fit together to form a larger image with low resolution. The situation improved in the 1980s when large infrared detectors were developed for military use. Astronomers were able to adapt these new instruments for their own purposes. The new devices are tuned to specific near or far infrared wavelengths. Combined with satellite technology, these new imaging devices are extending to prospects of the observation of the Universe. Nowadays infrared detector technology has a rapid development. Astronomers use InSb and HgCdTe detectors for the 1 to 5 micron range, which are much more sensitive then the traditional infrared CCDs. The development of infrared array detectors from the 1980's to now has been increasing the sensitivity of infrared observations to a great extent. During this time detector arrays were introduced, as a combination of several single detectors. They, together with the sophisticated optical systems built in cameras, allow astronomers to produce high resolution images containing tens of millions of pixels.

Infrared instrumentation at Calar Alto is essential for German and Spanish astronomy in the northern hemisphere. In recent years, the MPIA and Calar Alto Observatory have made a great leap in the development of infrared instrumentation and astronomy. The principal instruments used until 2003 were Omega Cass and Omega Prime. These cameras have 1k×1k HAWAII-1 HgCdTe arrays manufactured by Rockwell Science Center in the USA. These were the largest available arrays of their type at the time, and the Omega Prime camera still has one of the largest field of view (6.8 arcmin) on a 4m class telescope for infrared astronomy. However, this is small compared to optical cameras (e.g. 33 acrmin for the Wide Field Imager on MPG/ESO 2.2m at La Silla), and only now are larger arrays being fabricated. As a continuation of these achievements, the MPIA started the OMEGA2000 project. In the framework of this project the OMEGA2000 instrument has been built and mounted on the 3.5m telescope in Calar Alto. The OMEGA2000 is a wide field NIR imaging camera, which uses a 2k×2k HAWAII-2 HgCdTe Focal Plane Array from Rockwell. The camera was successfully installed and is already in operation, producing valuable data in observations runing in the last two years.

The goal of this doctoral thesis is to present the work I made as a participant in the OMEGA2000 projects and as a scientific user of the instrument. As a project member, I had the technical task to implement and test the operation of the OMEGA2000 camera and as an

astronomer I carried out observations with the wide field imager, reduced, evaluated, and interpreted the observed data. According to this twofold task, the thesis consists of two parts. The first part is devoted to the technical side of the project - discussing how to impelement and optimize the operation of the HAWAII-2 Focal Plane Array (FPA) installed in the OMEGA2000 instrument and to test its performance. The first part of thesis starts with an overview on the HAWAII-2 detector, describing its architecture and operation. Then I give the detailed specifications of this work, where we discuss the solutions of the problems related to the operation of the camera. We also describe the methods and techniques applied to optimize the detector operation. MPIA had an opportunity to test three specimen of this type of FPA which were used in different scientific projects and compare their performance. In the end of the first part we also present the results of the performance tests of these detectors. The second part of the thesis presents a scientific application of the OMEGA2000 instrument. This application was the COMBO-17+2 NIR survey, a preliminary study of the MANOS Deep or COMBO-17+4 NIR project. MANOS Deep Field Survey was planned to extend the results of the COMBO-17 galaxy survey, which provided reliable photometric redshifts derived from an optical data set of 17 filters for about 25,000 galaxies in three fields. The aim of COMBO-17+4 NIR survey is to extend the statistics of various astrophysical properties in this galaxy sample to higher redshifts and to improve the measurement of these properties by supplementing the optical data set of the COMBO-17 survey with NIR band data of 4 filters. In the preliminary survey the OMEGA2000 camera produced NIR data in two bands for a COMBO-17 field which already have a full set of optical data. In the second part of the thesis we review the results of the COMBO-17 survey and discuss the technical and astrophysical results of the preliminary survey. We analyze the improvement in the measurement due to the NIR-band extention and the increase of the number of filters, comparing the measurement process based on only optical data with that based on the optical and the NIR-band data. Due to the still limited depth of the NIR observations, the original plan to extent the results of the COMBO-17 survey to higher redshifts was postponed. We restricted the aim of thesis to the study of objects which are especially bright in H band. Therefore we discuss the preliminary results produced by COMBO-17+2 NIR survey in astrophysical context. We present the redshift distribution of bright infrared galaxies selected from the COMBO-17 sample and analyse the redshift evolution of their number counts for four galaxy types defined by their restframe colors. As a special astrophysical application related to the bright infrared sources, we study the sample of the Extremely Red Oject (EROs) detected in the COMBO-17+2 NIR survey and complete the thesis with some results on their properties and nature, which were derived from survey data.

Part I

Test of the wide-field Infrared Camera OMEGA2000

Chapter 1

OMEGA2000 Instrument

The OMEGA2000 instrument is a prime focus near infrared (NIR) wide-field camera mounted on the 3.5 m telescope at Calar Alto in Spain (Fig. 1.1). The camera uses a HAWAII-2 2kx2k HgCdTe Focal Plane Array (FPA), which is a new generation of the large format NIR image sensors developed by the Rockwell company. The instrument, designed particularly for survey observations, has an excellent optical quality and high sensitivity over a wide field. In order to archive an outstanding performance of OMEGA2000, many requirements must be met by the optical, mechanical, and the electronic components of the camera system. The first chapter reviews the set-up and operation of these carefully designed and produced mechanisms. In the first section we begin with a short account of the mechanical design of the dewar containing the camera system. The cryogenic optical system, consisting of a four-lens focal reducer located in

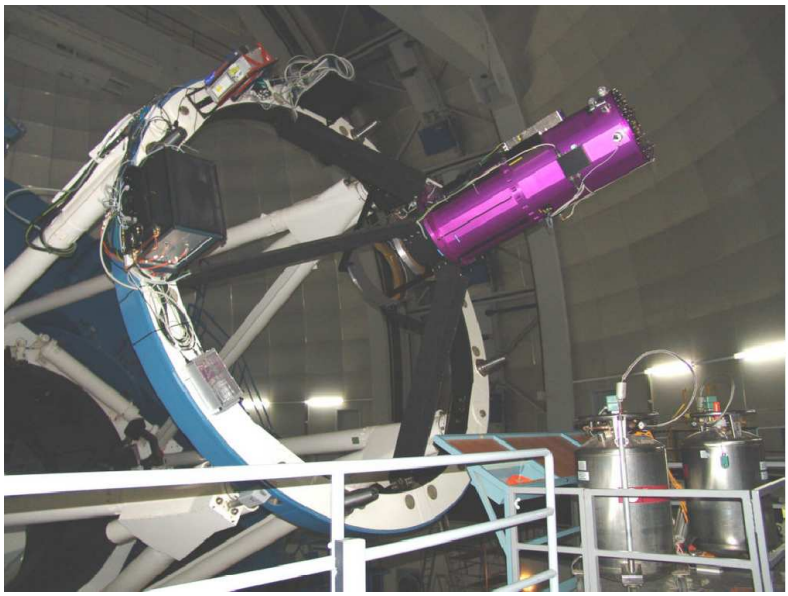

Figure 1.1: The OMEGA2000 NIR camera mounted on front ring (In Röser, 2004).

the prime focus, will then be discussed briefly in the second section. The third section presents the mechanical design of the filter wheels and the warm mirror baffle system as well. The chapter is ended with a concise description of the multi functional data acquisition system and control software of OMEGA2000, which performs the readout and the data saving simultaneously at a

high data rate.

1.1 Cryostat

One of the most important problems in ground based Infra Red (IR) imaging is to reduce the photon noise from the background. A significant part of this noise is from the bright sky, which is predominantly OH air-glow at nights in the wavelength regime below 3 μm. The thermal radiation from the warm telescope mirrors, structure, and dome is dominant longwards of about 2.2 μm, causing problems for the K-band imaging. In an effort to insulate the detector and the optics of OMEGA2000 from the latter, they are enclosed in a cryostat and cooled by liquid nitrogen to the operating temperature, 77 K (Baumeister et al., 2002). The cryostat contains three shields nested into each other whose purpose is to reduce the thermal radiation (Fig. 1.2). The liquid nitrogen is stored in two vessels, which can be filled on the telescope through the upper side of the dewar. The inner vessel is directly connected to the inner radiation shield and the outer one to the second shield. The outer shield is passive, since it is not thermally connected to the vessels. The lower end of the inner vessel also serves as a base for the cold plate of the detector unit. Both vessels are filled up to a level which allows a tilt angle of the telescope for taking the service position. After filling up the vessels, the dewar keeps the cold parts at thermal equilibrium for about 34 hours. In order to control the axial and radial shrinkage of the vessels and the shields, epoxy spacers carrying the axial loads are attached to the vessels. This allows the inner parts to be supported flexibly in the axial direction and rigidly in the radial one.

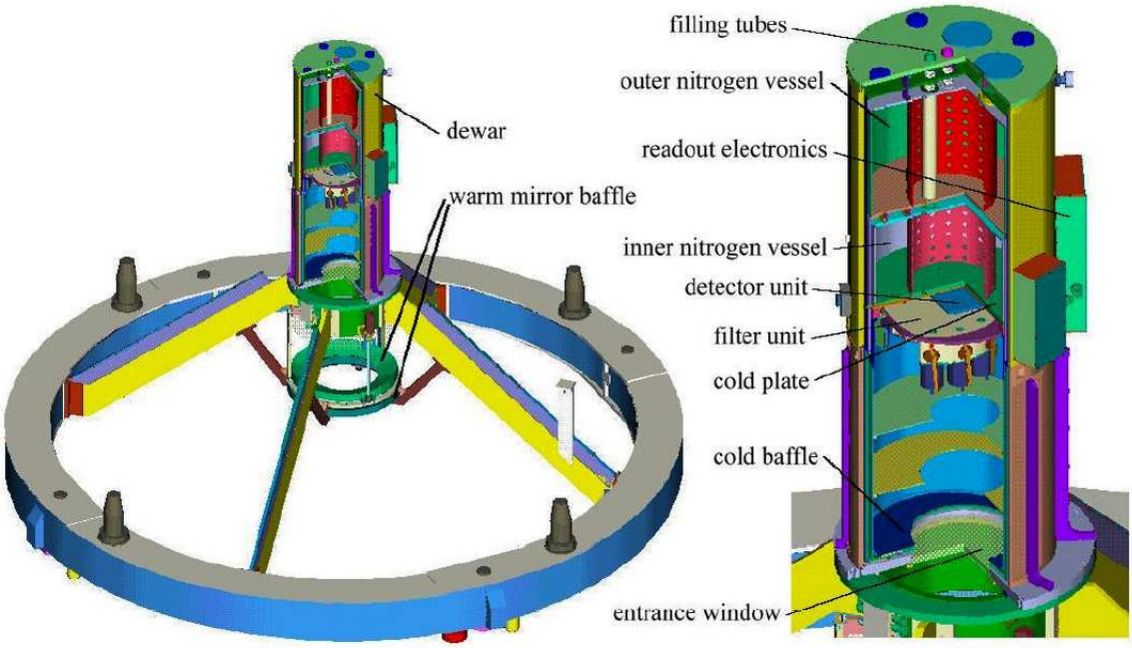

Figure 1.2: The OMEGA2000 cryosat mounted on front ring (In Baumeister et al., 2002).

1.2 Optics

Since the primary science goal was for OMEGA2000 to be a IR wide field imager, producing high quality images with the largest reasonable pixel scale, it is placed at the prime focus of the telescope. The optics consists of a cryogenic focal reducer providing a 15.4 × 15.4 arcmin field of view with a resolution of 0.45 arcsec/pixel (Baumeister et al., 2002). It has four corrector lenses made of CaF_2, fused silica (FS), BaF_2 and ZnSe with diameters between 106 and 150 mm, which are achromatic between 850 and 2500 nm (Fig.1.3). Each lens is fixed by a spring-loaded retainer ring in a single assembly. To achieve an excellent optical image quality and to minimize

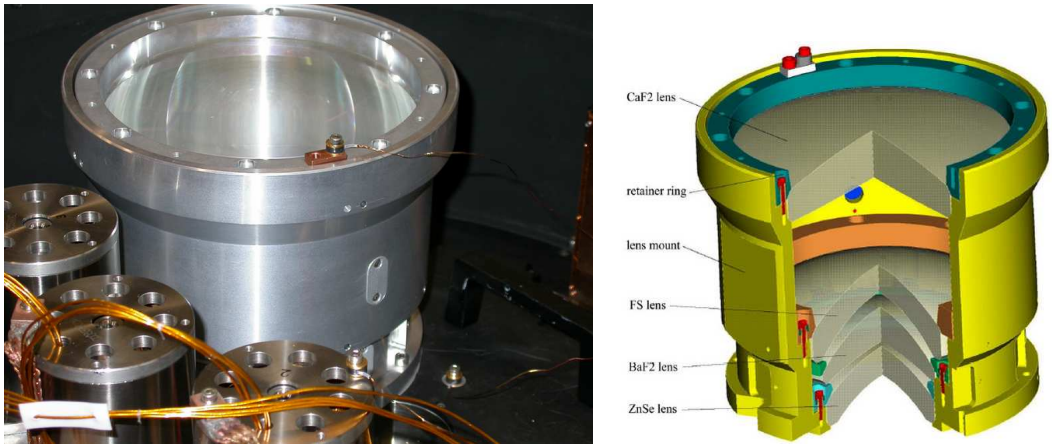

Figure 1.3: Four lens reducer with spring loaded cryogenic lens mount (In Baumeister et al., 2002).

the lens diameters, the focal reducer unit is located in the dewar, as close to the detector as possible. This means it is cooled down to a temperature of about 80 K, so the most difficult task of the lens mount design was to make sure that the lenses survive cooling and at the same time achieve the tight tolerances required for high optical quality. As a solution to this problem, chamfers with angle of 45° are used for both outer edges of each lens, the lens mount and the retainer ring. The lenses sit on the conical surfaces of the mount and the retainer keeps them in this position. Temperature changes result in diameter changes in the parts and lenses can slide on the chamfer surfaces relative to each other, which leads to an axial displacement. Tests have shown that changes in the accurately aligned lens positions (±0.01mm) caused by multiple cooling cycles and changes in dewar orientation cannot be measured down to the accuracy of ±0.005mm. With these tolerances, the optical quality produced by the focal reducer together with the dewar window completely fulfills the requirements. To determine the optical distortion, during the operation of the camera distances between a star at the center and all the other objects in the field of view were calculated both from the measured positions on the detector and directly from the differences of the RA and DEC positions. The ratio of the two distance measurements was plotted as a function of distance from the field center. The center to corner image distortion was measured to 0.12" for the maximum distance of 600", which is less than one pixel (Fig. 1.4). This is an exceptionally low distortion level. However scattered light and reflections could be seen in the flat-field images, which were attributed to the shining aluminum

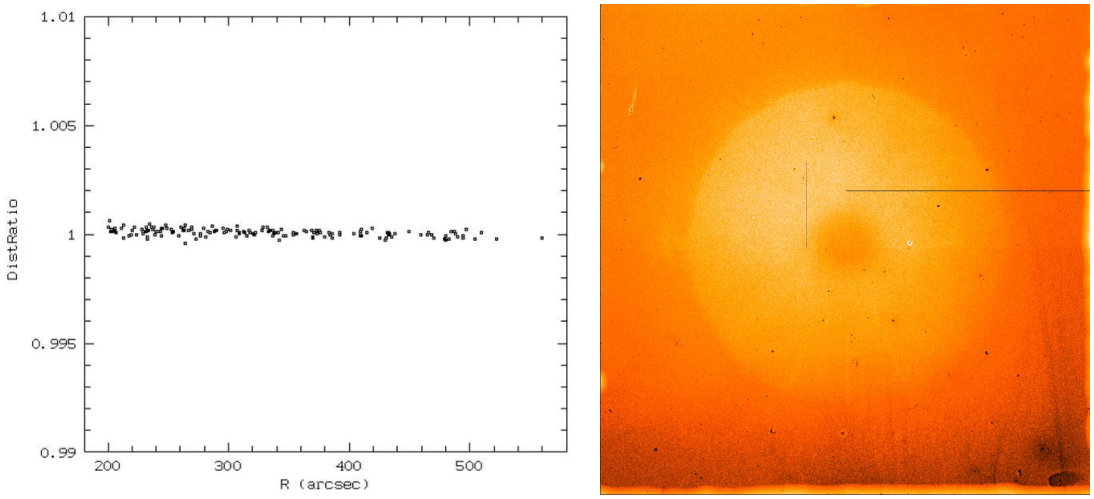

Figure 1.4: The left hand panel shows the center to corner image distortion of the OMEGA2000 optics (In Röser, 2004) and the right hand panel is a flatfield frame with the ghost image of the primary mirror.

surface of the optics mount. The largest accessible areas were covered to reduce the scattering but the bevels defining the lens positions could not be painted and they were still reflecting surfaces. There were also reflections between the filter surface and the innermost lens producing ghost images of the primary mirror in the flatfields (Fig. 1.4).

1.3 Baffle system

The OMEGA2000 was designed without a cold pupil or re-imaging optics. This means the camera has no cold-Lyot-stop, which would be able to prevent the detector from receiving the thermal radiation from the warm telescope structure and dome. While only the sky background is significant for J and H band imaging, the surrounding thermal noise causes problems in K band without re-imaging. As a solution, OMEGA2000 is equipped with a baffle system to minimize the amount of background radiation reaching the detector in the K band (Baumeister et al., 2002). The baffle system consists of one cold and two warm mirror baffles (Fig. 1.5). The cold baffle is located inside the dewar to reduce thermal background emitted by the surroundings of the telescope pupil. The position of the cold baffle is as far from the detector as possible but the distance between them is limited by the size of the dewar window, feasible dewar dimensions, and a maximum tolerated central obscuration. The warm baffles of the camera are annual sections of an oblate ellipsoid with the edges of the cold baffle as the foci. The first baffle (diameter 750 mm) is at a fixed position and does not vignette the field of view. The second baffle has a smaller inner diameter and it is designed to vignette the entire field of view uniformly. It prevents the detector from seeing the warm surroundings, which improves the S/N ratio in the K band. For J and H band observations, the baffle can be moved closer to the dewar to a position where it does not vignette at all (Bailer et al., 2000).

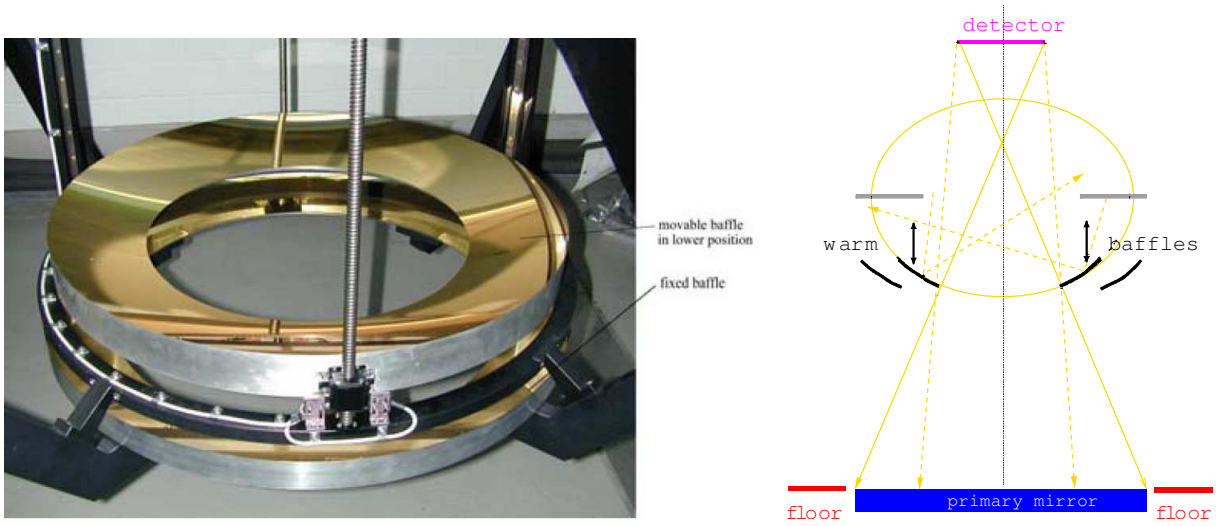

Figure 1.5: The warm baffles of OMEGA2000 (In Baumeister et al., 2002) and the working principle of the movable warm baffle (In Röser, 2004).

1.4 Filter Mechanism

The OMEGA2000 contains 17 filters of 3 inch diameter for wavelengths between 0.8 and 2.4 μm and one closed blank, which are distributed over three filter wheels. The filter unit containing the wheels, the cryogenic stepper motors and the locking/cooling mechanisms is placed between the detector and the focal reducer. Each wheel, mounted on a cryogenic ball bearing, contains seven equally spaced locking positions (six for filters and one free opening) and each filter position has a 3-bit magnet arrangement for determining the selected filter by three Hall sensors. The filters can be repositioned with an accuracy of less than 22 arcsec. With the pixel size of the HAWAII-2 detector of 18μm, this angle corresponds to 0.78 pixels at the outer edge of a filter.

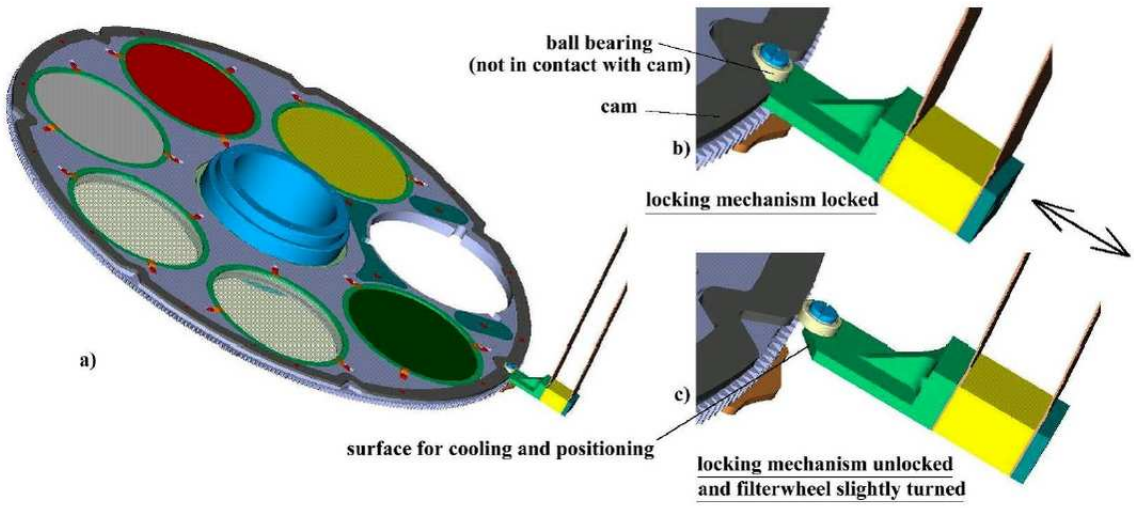

Figure 1.6: The filter wheel with its spring mechanism for positioning and cooling (a), mechanism locked (b) and unlocked (c) (In Baumeister et al. 2002).

1.5 Detector Mount

The detector fanout board holds a Zero Insertion Force (ZIF) socket mount for the HAWAII-2 detector, which allows us to connect the HAWAII-2 chip without any friction on the pins. Before the chip is inserted, a lever on the side of the ZIF socket is moved, pushing all the sprung contacts apart so that the chip can be inserted with very little force. The lever is then moved back, allowing the contacts to close and grip the pins of the FPA. The central pins of the chip carrier and the socket are used for thermal contact, whereas the outer two rows on each side are electrical contacts. The detector unit consists of a rigid aluminum base plate or "cold plate" which carries the fanout board on 12 identical cylindrical supports (Fig. 1.7). A spring-loaded cooling mechanism is used to cool the detector. A copper bar, which is preloaded by springs, presses an indium foil against the central detector pins.

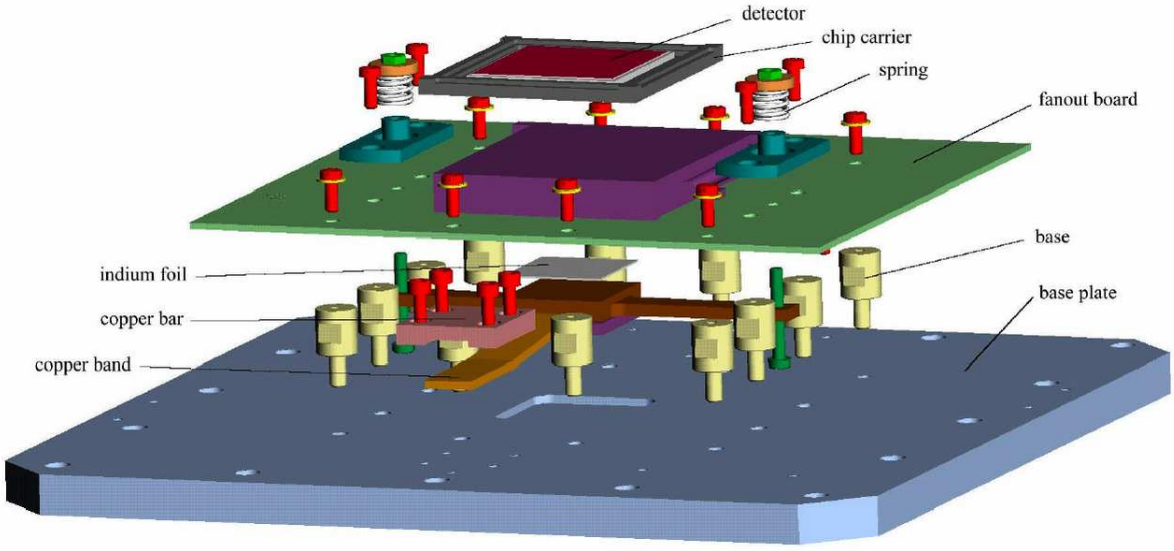

Figure 1.7: The detector unit with the base plate, fanout board, detector and its cooling mechanism (In Baumeister et al., 2002).

1.6 The Readout Electronics and Control Software

The general readout electronics at MPIA were designed not for only OMEGA2000 but a number of different instruments, including MIDI and LUCIFER. Although the electronics contain universal functional units, they were configured to fit the particular requirements. The data acquisition system of the OMEGA2000 consists of several hardware layers through which the data transfer is controlled: the hardware components located in the dewar, the detector front-end electronics, the data acquisition and control electronics, and a computer data interface connected to the network via I/O ports (Fig. 1.8). The video outputs of the HAWAII-2 FPA from the fanout board (first layer) go to the front-end electronics consisting of two preamplifier boards and clock drivers via 32 channels and the amplified signals organized in four cables are sent to the readout electronics containing eight boards of AD converters, which receive the video signals. The output range of the amplified video signal is 3.5 - 4.5 V. After the amplification, subtraction and an

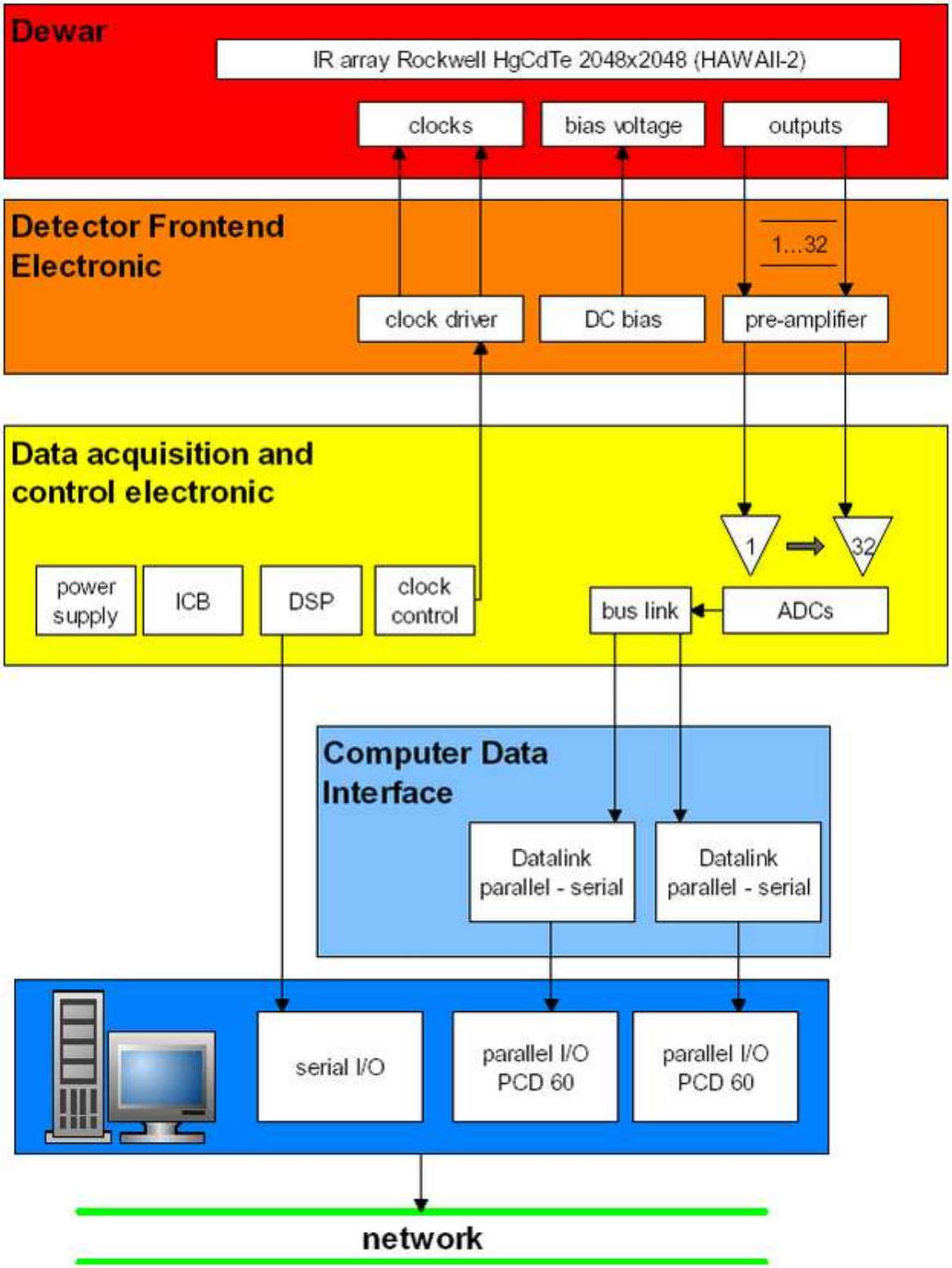

Figure 1.8: The block diagram of the read-out electronics of OMEGA2000 (In Röser, 2004).

AD conversion the range of the video output is ±32767, which is mapped into the range 0-65535 ADU. Thus, one count represents about 76 μV (Fig. 1.9).

A Digital Signal Processor (DSP) clocks the readout process of the chip and the timing of the data transfer through control channels and triggers the AD conversions. These tasks are implemented as control patterns in the instruction tables and macros handled by the DSP. The patterns are sequences of control signals of the chip and the instruction tables consist of linear sequences and loops of instructions which determine the timing and repetition of these patterns. The macros for the pattern generator contain instructions for more general purposes such as running instruction tables in the DSP memory or controlling the DSP itself. The digitized video outputs from two BUSLINK cards, via FDDI cables, arrive at a signal converter which transforms them to a proper data format for a Sun workstation. The DSP is controlled by a microprocessor

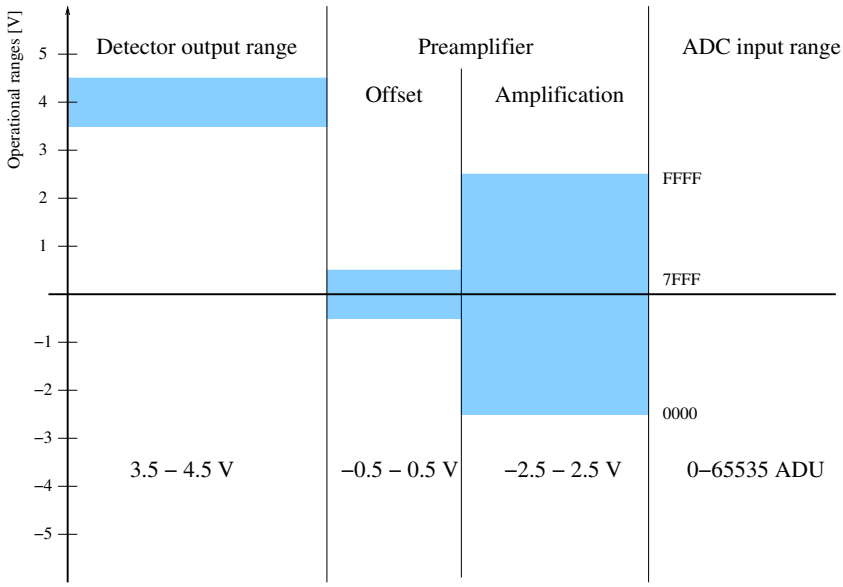

Figure 1.9: The conversion range between the analog output of HAWAII-2 detector, 3.5-4.5 V, and digitized data, 0-65535 ADU.

which communicates with the IR control software running on the workstation.

The data acquisition and control software used for OMEGA2000 is the Generic Infra-Red camera Software (GEIRS) developed for the general readout electronics. The software is able to sustain a high data transfer rate continuously, have data visualization control, and save the data in time to hard disks. These tasks have been implemented by efficient organization of shared data buffers and parallel processing with optimal usage of the multiprocessor capabilities. Besides the command line prompt, the control software has a graphical user interface with control panels and a display for the video output. The parameters of the readout process can be set and modified in the control panels (Fig. 1.10). Each readout mode is implemented in corresponding instruction tables, which the control software can load and send to the DSP. The parameter files of GEIRS contain these instruction tables, different clock and control patterns for the 1 and 8 output modes, and macros calling the instruction tables in different output, readout and idle/non-idle modes. The control software stores the parameters in variables, such as the integration time, the repetition number of readout, the actual readout and output mode or the filter and baffle

positions. During the initialization process of the clock and control patterns, the instruction tables and the macros required for the actual output and readout modes are sent to the DSP by the software.

If a parameter is changed via the control panel, the software reinitializes the electronics and sends the new instruction tables and macros to the readout electronics before starting any readout process. The readout frames are stored in a memory buffer and saved interactively or by GEIRS commands. The commands of the control software can be organized batches, i.e., in predefined series of readout commands with given integration times, repetition counter and other commands to synchronize the different steps or move the telescope. We used the environment of GEIRS to test and characterize different HAWAII-2 detectors but the observations were carried out with MIDAS utilities controlling the camera software.

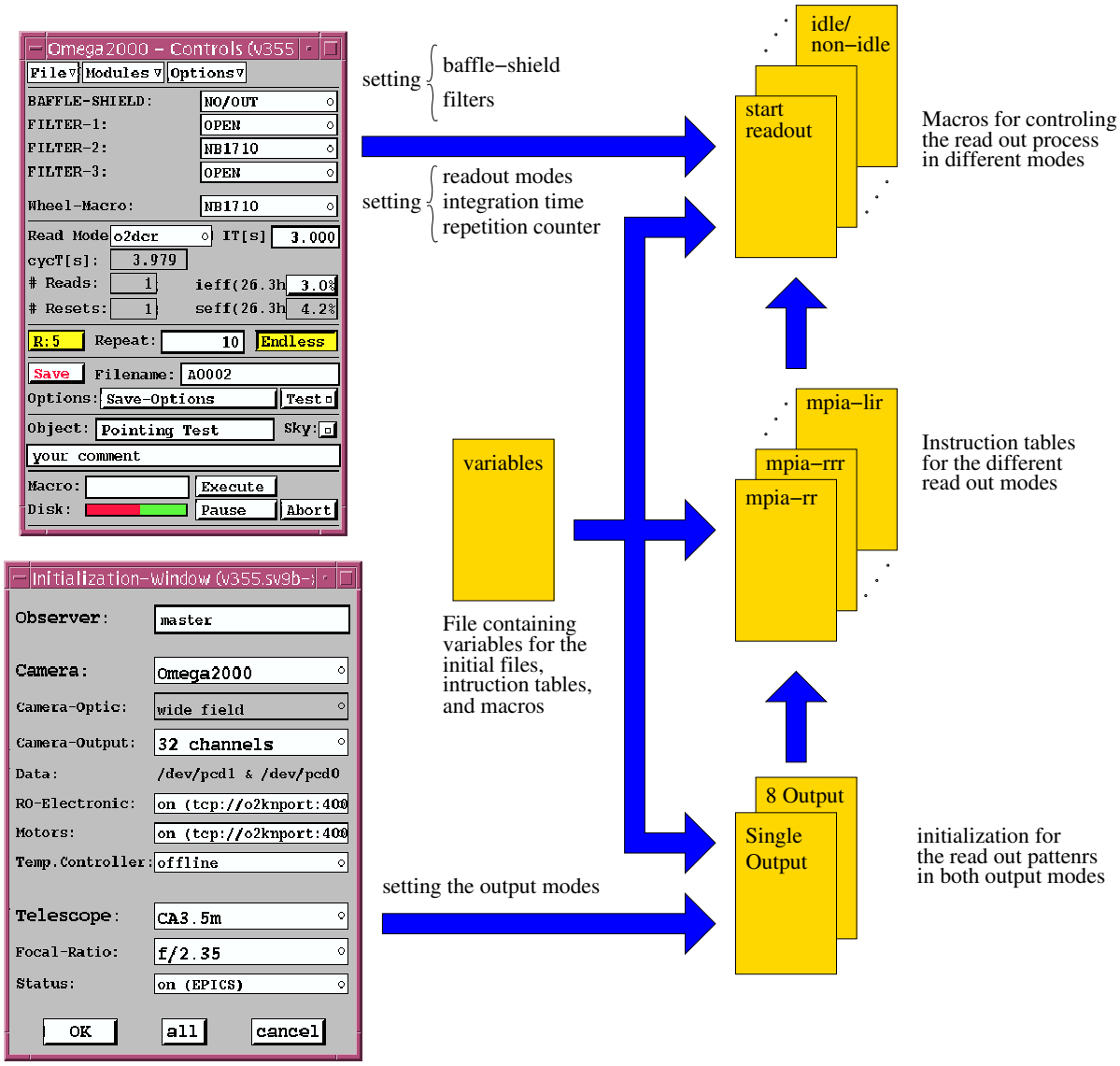

Figure 1.10: The scheme of the control interface of GEIRS. The two main control panels of GEIRS are shown in the left hand side. The files containing the macros, instruction tables, files for initialization, and variables for the readout electronics are represented with yellow boxes. whereas the blue arrows indicate their dependencies on each other.

Chapter 2

The HAWAII-2 Focal Plane Array

In the history of the developement of InfraRed (IR) image sensors several architectures of different properties and performances were born with various advantages and drawbacks. In this chapter we introduce the basic concepts of wide-spread IR detector families, considering their layouts and operations. This helps us to present the HAWAII-2 Focal Plane Array (FPA) applied for the OMEGA2000 instrument and understand the principles of its operation. The first section of this chapter starts with comparison of the Charged-Couple Device (CCD) and Complementary Metal Oxide Semiconductor (CMOS) architectures developed for the IR imagers and goes on to describe the layout and readout architecture of the HAWAII-2 sensor in details. In the second section, all the readout modes of the detector are presented which the team of the OMEGA2000 project implemented for engineering or scientific purposes. The optimization of the different readout modes will be discussed in the subsequent chapter, as an issue which determines the detector performance.

2.1 Design and Operation of the HAWAII-2 FPA

CCD sensors had been fairly widespread in IR imaging until the mid eighties when CMOS detectors started to supersede the traditional technology. It was due to the fact that CMOS technology allows simplification of the sensor interface and increase of on-chip integration while enhancing the performance of infrared detectors to a great extent. As a result of this development, a continuously broadening family of the HAWAII Focal Plane Arrays (FPA) has been brought to the market recently by Rockwell Science Center. The HAWAII-2 FPA, the latest member of this family, is the largest high-performance detector available for infrared astronomy at the moment (Fig. 2.1). With an array size of 36×36 mm^2 and 2048×2048 pixel format, it provides unrivaled spatial resolution and sensitivity and is a good candidate to satisfy the requirements of the next generation scientific projects.

Here, we present the setup and operation of the HAWAII-2 detector in three sections. In order to give an overview on the motivations which lead to the design of the HAWAII-2 FPA, we start with a short comparison of the CMOS technology that makes the HAWAII-2 image sensor so outstanding in its category within the traditional CCD paradigm. In the second section there is a brief summary on the design issues of the HAWAII-2 layout. In the last section we describe internal architecture of the chip circuits and their operation.

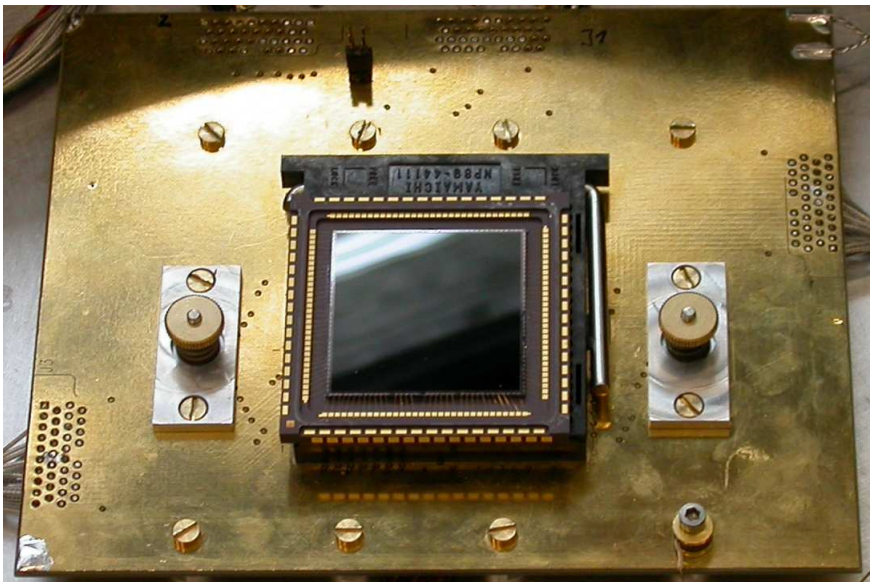

Figure 2.1: HAWAII-2 FPA mounted on its fanout board (Photo: Peter Bizenberger).

2.1.1 Infrared detectors

In a general setup of IR detectors a photosensitive semiconductor layer is grown on a transparent substrate. Incident photons are absorbed in this semiconductor material and generate charge carriers, which are collected in the well capacities of each pixel during the integration time. In the readout process the accumulated charge is transferred to the pixel row and column shift registers, where a sense node capacitance converts it to photo-voltage. The CCD chips, the traditional solution in the IR imaging, operate according to the above described passive pixel sensor (PPS) sheme. They absorb photons and store charge in the same bulk material with a simple pixel layout and use an external amplifier circuit for data acquisition.

However, this architecture has some drawbacks. The amplification of the video output by off-chip circuits causes the readout noise of the large format CCD chips to be dominated by the wide band thermal noise of the output amplifier and the excess noise of the video electronics. Both noise sources can be minimized by maximizing the conversion gain, i.e., minimizing the sense node capacitance but this approach has its limits. If the photo-voltage is read before and after the integration and only the difference of these values is sampled as a video signal, some the reset noise and the $1/f$ noise can be mitigated but the thermal noise remains the same. Another problem is the leaking of the collected charges from a pixel to the adjacent ones in case of saturation, which smears the photo-signal over the area of that pixel group. Normally the saturation of the whole chip is avoided during the operation of CCDs but pixel arrays alway contain hot pixels which can be saturated even if the exposure time is short enough to prevent the saturation of the normal pixels. It is hard for CCDs to avoid the smear-off effect caused by hot pixels. Besides these problems, the readout process of CCDs is destructive, i.e., the collector capacitance in pixels has to be recharged to measure the voltage of the pixels, which might affect the charge collection.

While CCD imagers use only passive pixel sensors (PPS), CMOS detectors can have either

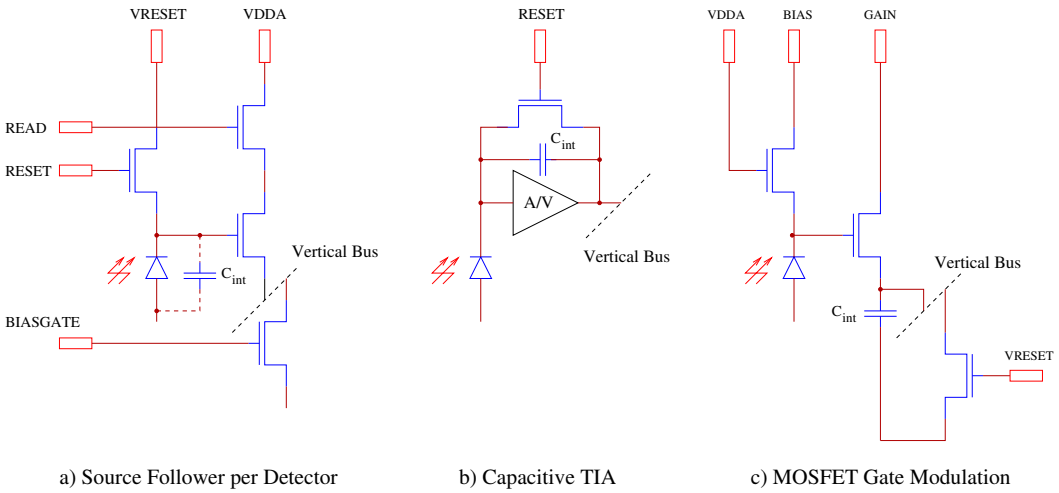

Figure 2.2: Low noise APS Circuits for hybrid and monolithic FPAs. SF detectors (a), CTI Amplifiers (b) and the solution of MOSFET Gate Modulation (c) (In Hodapp, 2000).

active or passive pixel based architectures. Active pixel sensors (APS) with a higher on-chip integration can amplify photo-voltage at each pixel before reading out. They therefore provide a more efficient readout noise reduction. Depending on the degree of on-chip integration there are three different types of APS (Fig. 2.2). The simplest is the source follower detector (SFD) using three transistors. Two of them are for accessing and reseting the pixel and the third provides amplification. Capacitive TransImpendance Amplifiers (CTIA) have a fourth transistor besides the SF amplifier to amplify voltage further and have a negative feedback to suppress the kTC noise generated by setting the detector. The resetting of the integration capacitance also produce kTC noise but a fifth transistor can reduce it by modulating the gain of the video signal. Hence the APS consisting of five transistors achieves the lowest output read noise, about 1 e^-, depending on the combination of detector, feedback and integration capacitance. Nevertheless, if the total capacitance consisting of the detector capacitance and input capacitance of a three-transistor APS is in the order of 10 fF the read noise produced in a double correlated read is only in the order of 10 e^-. It is therefore the most advantageous to implement a three-transistor SFD by the virtue of its relatively simple pixel layout and good performance (Hodapp et al., 1995).

The APS design allows for the usage of the reverse bias mode, where the capacitance of each pixel is completely charged by applying a constant reset voltage in the whole array. Incoming photons discharge the capacitances of pixels, reducing the voltage measured on them. The photo signal is inverse proportional to the remnant charges or voltages. Saturated pixels are completely discharged without causing any leakage in the adjacent pixels, which is a further advantage of the CMOS technology, compared to CCDs. Another advantage of using the APS scheme, is the non-destructive readout, i.e, the preservation of charges in the pixel capacitances, in which the voltage on pixels can be measured without affecting the charge collection. However, the simple pixel architecture is very important because it allows for minimazation of the gap between the optically sensitive regions of the pixels, called photo-sites. This increases the optical collection efficiency, characterized by the fill factor, to as high an extent as possible. The passive pixel based imagers have pixels consisting of only one photo-diode and a MOSFET switch, which allows for

a high fill factor. The pixels of APSs contains many components, making the gaps between them large. This bulkiness reduces the fill factor considerably, even in the case of the more compact three-transistor SFD. However, this problem can be solved by application of a hybrid layer structure for signal detection and readout functions, which separates them instead of using a single bulk material. The gap between the unit cells is thereby reduced, which results in a higher fill factor of the sensor. The HAWAII FPA family belongs to the first generation products of hybrid technology for IR imagers and the next sections will describe its latest member, the HAWAII-2 FPA, in details.

2.1.2 Layout of the HAWAII-2 FPA

Besides the capability to optimize the optical fill factor efficiently, there are other advantages of the hybrid structure. The photosensitive layer can be grown separately from the multiplexer layout itself, which allows fine tuning of the composition and thickness of the stratum. The properties of the detector material are optimized so that it could meet various requirements of the operation (Hodapp, 2000).

A CdTe layer is grown on a lattice-matched sapphire substrate by metal organic chemical vapor deposition and the result, due to Hg vacancies, is a p-type semiconductor material (Fig. 2.3). The band gap of HgCd can be adjusted by controlling the molar fraction of the Hg and Cd and the uniformity and thickness by controlling the melt temperature during the evaporation. This fine tuning also allows reduction of the number of defects in the photosensitive layer whose presence decreases the performance of the detector. The band gap determines the cut-off frequency of the detector and the spectral response of the HAWAII-2 is 0.85-2.6 μm (the sapphire substrate is transparent for visible and infrared radiation to beyond 5.5 μm). The photosensitive layer must be thick enough to absorb as much IR radiation as possible, i.e., few times greater than the absorption length of IR photons. Nevertheless, its thickness should be no more than the diffusion length of minority charge carries generated by absorbed photons in order to avoid diffusing of the minority carriers into neighboring pixels, which causes image blurring, or their recombination before they can be collected, reducing the quantum efficiency. HAWAII-2 has a

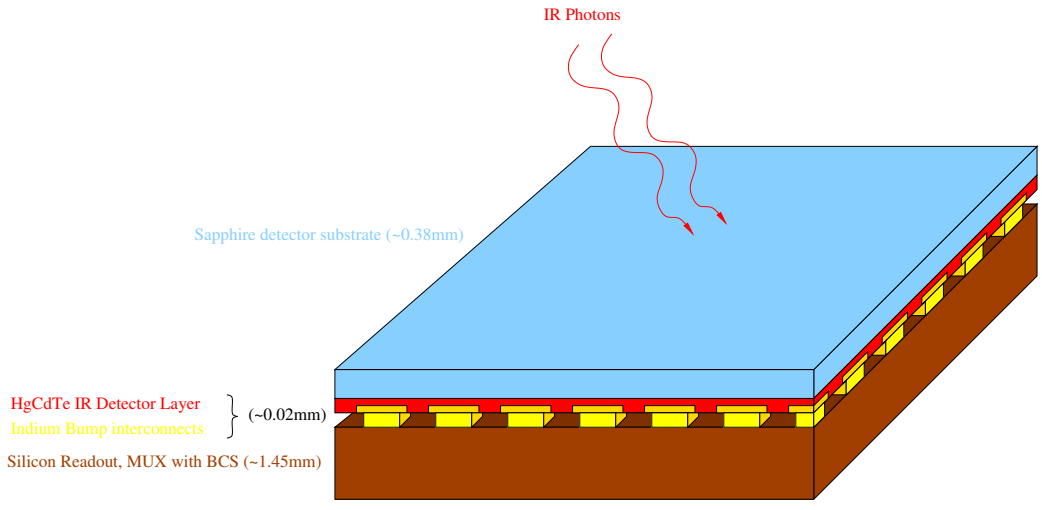

Figure 2.3: The cross-sectional view of HAWAII-2 (in Kozlowski et al., 1998).

~ 10 μm thick photosensitive layer, which meets these requirements.

An important issue is the thermal and mechanical interface between the detector array and the silicon multiplexer. As the chip is cooled down to its operation temperature (77K), high mechanical pressure allowing tight thermal contact between its two main parts can cause high mechanical stress between them owing to their different thermal expansion coefficients. Weak mechanical forces applied to clamp the two parts reduce thermal coupling, which makes the detector temperature difficult to control. The choice of sapphire as a substrate makes this problem less severe, since its thermal expansion coefficient matches that of the silicon MUX. reasonably well. The application of indium columns as inter-connectors and backfilling the hybrid with epoxy futher mitigates the problem. Additionally, the HAWAII-2 array is mounted on a pin-grid chip carrier. While its outer pins provide electric connection, all its inner pins are used to connect the chip carrier thermally. The hybrid sandwich structure also allows an optimal design of the multiplexer of HAWAII-2, which is an array of MOSFET switches with SF amplifiers separated by other MOSFET switches. This kind of architecture has a minimal glow during its operation because the voltage can be lowered below 5 V. The multiplexer contains SF amplifiers for all unit cells of the detector layer (Fig. 2.5).

The pixel array is organized in a CMOS read architecture, which consists of four electrically independent quadrants (1k×1k pixels) with either 1 or 8 outputs per quadrant (Fig. 2.4). Each quadrant contains a horizontal and a vertical shift register for addressing the pixels in the array. During the detector readout, the horizontal register is clocked in the fast direction and the vertical register in the slow direction. All of the four quadrants are operated in parallel (Haas, 2002).

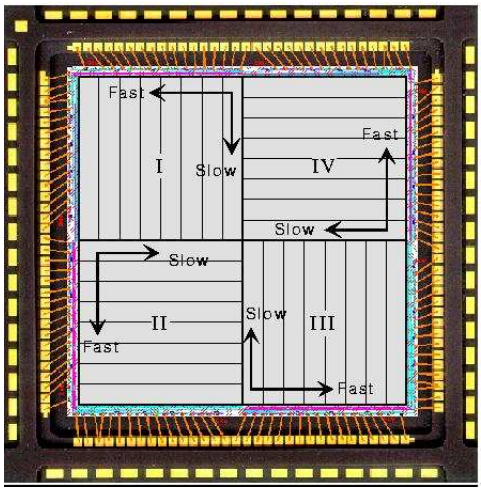

Figure 2.4: The quadrant and channel layout of HAWAII-2 (In Haas, 2002).

2.1.3 Internal Architecture and Operation of the HAWAII-2 FPA

The internal architecture of the HAWAII-2 FPA shown in Fig. 2.5 consists of three main parts: the unit cell, the shift registers, and the output SF amplifier. These functional units are controlled with thirteen logic signals and they also have two power supplies and three DC biases.

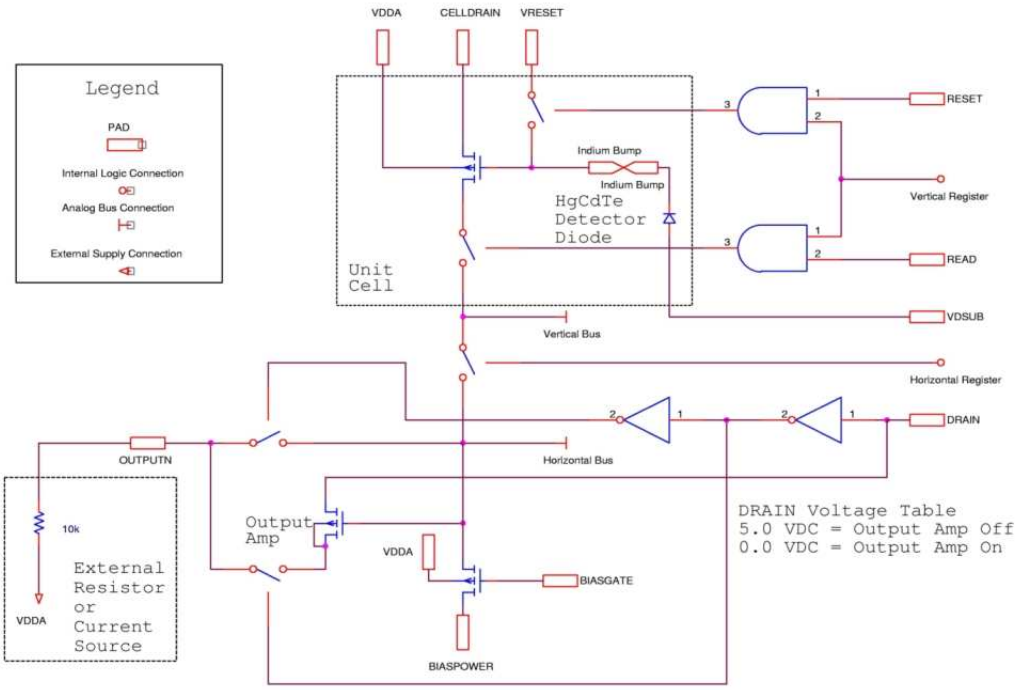

Figure 2.5: HAWAII-2 internal architecture (In Haas, 2002).

The unit cell consists of the HdCdTe detector diode, the drain transistor and MOSFET switches for reset and read and its basic control inputs are the digital signals READ and RESET and the bias voltage CELLDRAIN. The multiplexer is connected to the unit cell via the horizontal and vertical shift registers. The horizontal register has four basic clocks (CLK1/2 and CLKB1/2) and the control signal LSYNC for line synchronization. Two of the basic clocks (CLK1 and CLKB1) provide the same clock signals and the other two (CLK2 and CLKB2) are the complement of them. The readout of a pixel takes one full clock cycle, i.e., two clock edges per pixel. The register is reset by lowering LYSNC. When LSYNC goes high, the register is released and a single bit starts shifting down in the register. The vertical register is controlled by two external clocks, FSYNC and VCLK (frame synchronization and vertical clock). FSYNC has an active low state and it is pulsed once every frame. This pulse is propagated down in the vertical register by ticking of VCLK, i.e., a single positive pulse on VCLK addresses on row of the multiplexer for readout or reset. The control signals RESET and READ are for the line reset and read function of the multiplexer. RESET is an active high clock resetting all of the pixels in the selected row to the voltage set by VRESET. If READ is high then video signals from the current row are transferred to the vertical buses, which are inputs to the horizontal register. In turn, the horizontal register controlled by transmission gates produces input signals to the output SF amplifier.

There are two biases that can be adjusted for the SF amplifier, BIASGATE and VRESET. BIASGATE is the voltage gate of the "pull-up" P-FET for the SF amplifier and BIASPWR is the source voltage of the P-FET. The speed and the dynamical range of the unit cell SF can be adjusted by changing BIASGATE. VRESET is the reset voltage applied to the full array during the reset operation. Although external circuits can also be used instead of the output

Signal Name	Minimum	Nominal	Maximum	Comment
VDD	TBD	5.0	5.5	Digital Power Supply, must be $\leq$ VDDA
VSS	0.0	0.0	0.0	
MUXSUB	0.0	0.0	0.0	
VDDA	TBD	5.0	5.5	Analog and input protection network power supply, must be $\geq$ all other voltages
DSUB		0.0		
DRAIN	0.0	0.0,5.0	5.5	Output amplifier selection and amplifier drain voltage (5.0=Off chip amplifiers)
CELLDRAIN	0.0	0.0	5.5	
Bias Voltages				
BIASPOWER	TBD	5.0	5.5	
BIASGATE	0.0	3.5	5.5	Current control for unit cell
VRESET	0.0	0.5 to 1.0	5.5	PACE bias voltage range

Table 2.1: Nominal Bias Voltages for the HAWAII-2 (In Haas, 2002).

SF amplifier by raising the DRAIN signal, the latter is applied for OMEGA2000 configuration because of its more advantageous noise properties. When the internal SF amplifier operates, all the outputs are pulled up by using an external resistor so as to provide a proper bias for the amplifier.

The self-emission from these amplifiers can be minimized by turning them off during integration via the READ signal, which means the gate of the unit cell access P-FET is pulled "high" when not in use. This occurs when the READ input clock is "low", hence disconnecting all of the column buses from the gate of the SF amplifier. The gate will be pulled up via the BIASPWR bias input.

2.2 The Readout modes of HAWAII-2 FPA

There are three output modes available for the chip, which can be controlled via the readout patterns. In the *Single Output Mode* all data is routed to only one channel per quadrant. If the chip is set to *Eight Output, Unshuffle Mode* the data is spread across all the output channels of the detector, namely eight per quadrant. Each output provides data from 128 consecutive columns. The *Eight Output, Shuffled Mode* is similar to the previous one, except the data from each block of 128 columns is cyclically shifted to the next output bus. In normal operation of OMEGA2000 the *Eight Output, Unshuffled mode* is preferred because of its high speed. These output modes are controlled by the digital inputs O1 and O2, which can be set at the initialization of the whole readout process (Tab. 2.2). The background limit will be reached in broad-band imaging with HAWAII-2 array on OMEGA2000 in a few seconds. Series of images are therefore required to achieve sufficient S/N, so it is very important that the array can be read out with minimal dead time. The minimal integration time is given by the duration time of readout for a complete frame, which is on the order of one second for all readout modes. There are several readout

Output Mode	**O1**	**O2**
Single Output Mode	1	0
Eight Output, Unshuffled Mode	0	0
Eight Output, Shuffled Mode	0	1

Table 2.2: Output Mode Control Signals for HAWAII-2 (In Haas, 2002).

modes feasible for OMEGA2000 but some of them are used only for engineering function. This section will describe all of these modes in details. First we give an overview on how the readout process of the HAWAII-2 FPA is organized. Then we present the readout modes of the FPA which were to be implemented for the operation of the OMEGA2000.

2.2.1 The General Readout Scheme of the Detector

The HAWAII-2 chip is built up in electrically independent quadrants and they are controlled in parallel. This means the sequence of the control signals sent the HAWAII-2 chip by the readout electronics contains a readout patten only for one quadrant and this sequence is distributed in multiplexer to each quadrant in parallel. Therefore, the basic scheme of a readout mode consists of a reset and readout of a full quadrant and not the whole array. The implementations of all the readout modes are based on this general scheme for each quadrant, as shown in the timing diagrams in Figs. 2.6 and 2.7. Here, the frame synchronize signal, called FSYNC, has a pulse (negative logic) before starting the readout of the frame, indicating its beginning. The line synchronize signal, called LSYNC, is set high (positive logic) at the beginning of each row, which shifts the vertical shift register (slow direction) and allows to scan through the lines in the vertical direction. The pixel clocks CLK1, CLKB1, CLK2, and CLKB2 are clocking the vertical shift register (fast direction), scanning the actual row addressed by the horizontal register. The algorithm implementing this basic timing can be written as:

$$
\begin{array}{llll}
1. & \textit{once} & & \textbf{FSYNC} \ \& \ \textbf{LSYNC} \ \& \ \textbf{RESET} \\
2. & 1024/128 & \textit{times} & \textbf{Pixel CLK} \ \& \ \textbf{SCON} \\
3. & 1022 & \textit{times} & \textbf{FSYNC} \ \& \ \textbf{LSYNC} \ \& \ \textit{jump to step } 2. \\
4. & 1024/128 & \textit{times} & \textbf{Pixel CLK} \ \& \ \textbf{SCON}
\end{array}
\tag{2.1}
$$

This sequence of control patterns contains a loop scanning through each row of the array (the second and the third line), in which the clocking and pixel readout are repeated 1024 or 128 times according to the *Eight* or *One Output Mode*. Here, SCON denotes the pixel readout, that is the input signal of the A/D converter for starting the conversion of the video signal.

The readout process of the HAWAII-2 chip is organized in *readout cycles*, which are defined as sequences of control patterns providing a complete image. Of course they have different timing patterns for different readout modes. In the non-correlated modes the readout cycle is a complete readout of the full array with or without resetting the array. Whereas for the modes applying double correlated sampling the readou cycle refers to two frames which are needed to produce a complete image: the readout of the reset level and the readout of the integrated signal. The readout cycles therefore consist of different control sequences, depending on the readout mode.

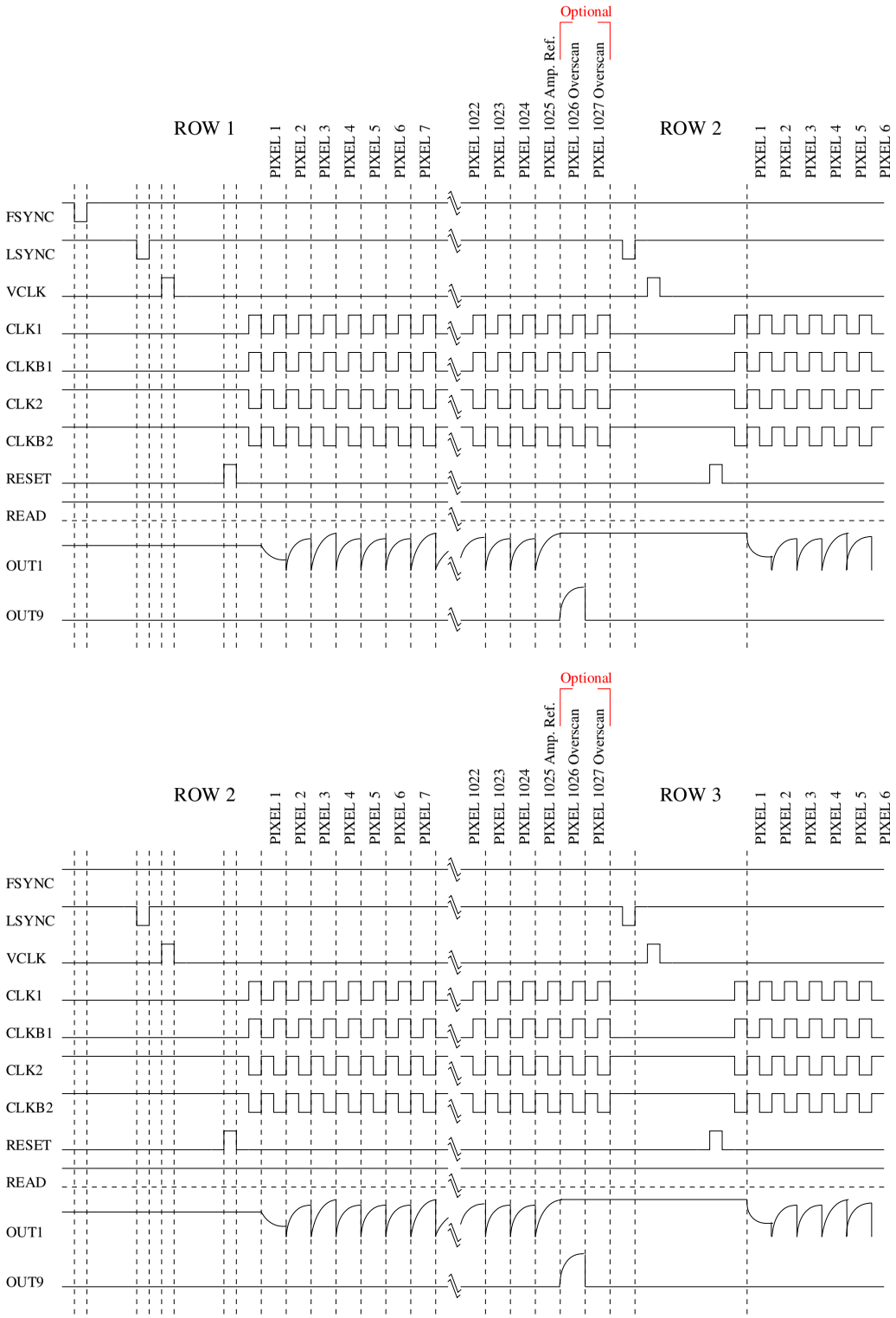

Figure 2.6: Timing diagrams for the readout of the first and second rows of HAWAII-2 FPA quadrant (In Haas, 2002).

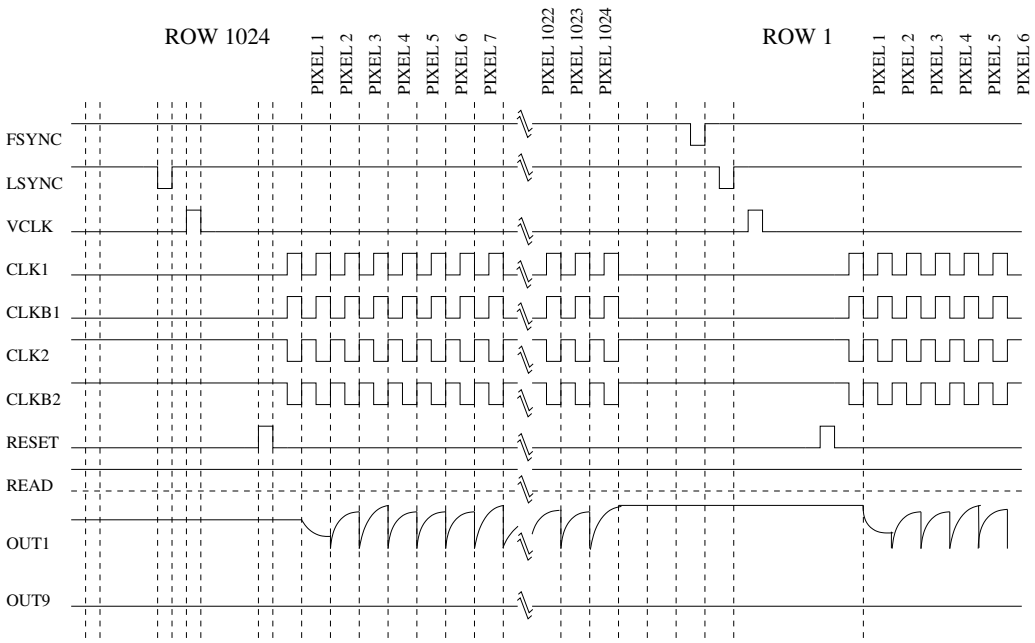

Figure 2.7: Timing diagram for the readout of the last and first rows of HAWAII-2 FPA quadrant (In Haas, 2002).

Each mode can be characterized with its efficiency, that is the ratio of integration time to the duration time of the readout cycle.

In order to increase the efficiency of the readout modes, we tried to maximize this ratio. There are three readout modes, the single pixel read, the reset level read and single correlated read, which are non correlated modes and used only for testing the operation of the chip. The double correlated read with two different implementation of the resetting, the line interlace read, and multiple end point read provide different solutions to operate the chip for scientific applications. We describe these read out modes in the following and compare them with each other in terms of their advantages and disadvantages.

2.2.2 Single Pixel Read (spr)

The read out cycle starts a full frame reset then only one pixel is read out in each channel or quadrant depending on whether the *Four* or *Eight Output Mode* is used. As a result, the data of a full channel or a quadrant consists of the value of only one arbitrarily chosen pixel. This mode is only for engineering purpose and used to test the stability of the readout process, comparing the data transfer of the same pixel value with that of the abruptly changing video signal due to the transient states in beginning the readout process of a whole quadrant.

2.2.3 Reset Level Read (rlr)

The readout of the reset level of a complete frame has the simplest readout scheme: we reset the full array then read it out. For HAWAII-2 FPA a line reset is implemented, which means that one reset pulse always resets each pixels in a line of the array and the chip needs 1024 pulses to reset the full array while clocking through the horizontal shift register. It allows the reset-readout

cycle to be accomplished in two ways. Either the whole array is reset and then read out or the reset-readout cycle is run line by line: one line is reset and then read out and the next line is reset and read out and so on up to the last line. The latter way means the whole array is reset and read quasi-simultaneously. In the first case the elapsed time between resetting and reading out of the same pixel is equal to the resetting time of the full array. The reset-readout scheme is faster in the second case, where each row is read out immediately after being reset (Fig. 2.8). The timing diagram of the integrated signal represents only the theoretical reset-readout scheme where the reset means a complete frame reset which is followed by the readout of the full array. As the video signal is sampled after resetting contains the reset noise and reset bias this readout mode has only engineering purpose for studying the the line reset scheme in a simple readout process of one frame.

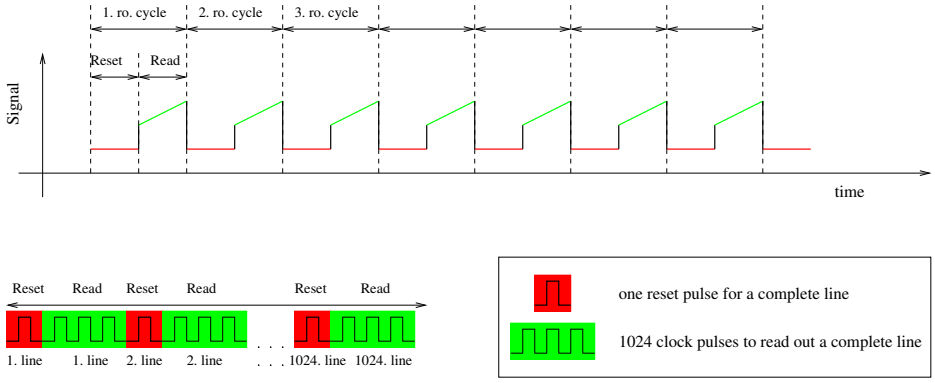

Figure 2.8: The timing diagrams of the signal (upper) and the control pattern (lower) for the reset level read (reset-read).

2.2.4 Non-correlated Sampling or Single Correlated Read (rr)

In the normal operation of the image sensor there is some exposure time between the frame reset and the readout of the full array so that more photo signal can be collected. The readout cycle of non-correlated sampling implements this reset-integration-read scheme (Fig. 2.9). Here, the reset is separated from the readout process by integration, which prevents the application of the fast reset method. Since the exposure lasts from the resetting of the first line of pixels until their readout, the resetting time of the full frame should be added to the integration time to obtain the total exposure time. The integrated frame contains not only the signal collected during exposure but also the reset bias and noise as in the previous mode, therefore this readout scheme is also applied only for engineering function.

2.2.5 Correlated Double Sampling or Double Correlated Read (o2dcr)

The Correlated Double Sampling (CDS) is introduced to eliminate reset bias which is present in any image taken in the previous readout mode. This scheme consists of a complete frame reset, a readout of the full array, an integration and a readout of the complete integrated frame. The reset and the first readout of the frame are not simultaneous, i.e., a slow reset is applied (Fig. 2.10). The output signal is obtained by the subtraction of the reset frame from the integrated

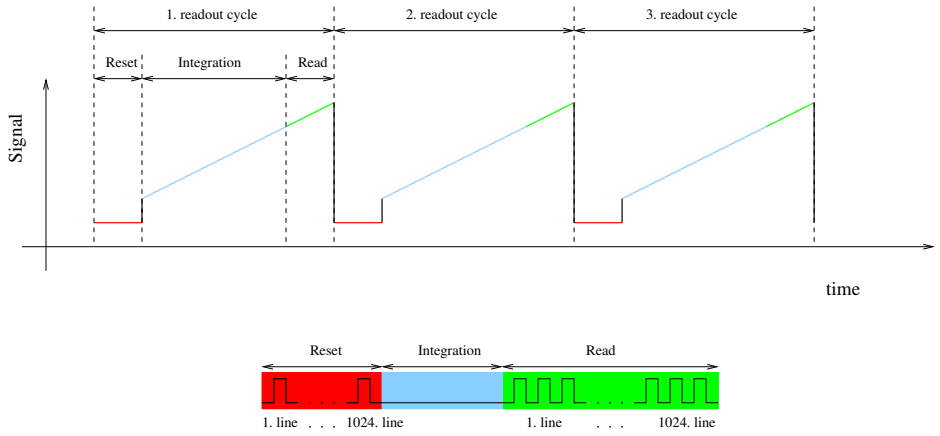

Figure 2.9: The timing diagrams of the signal and the control pattern for non-correlated sampling (reset-read).

one, which eliminates the reset bias from the signal value. Since the whole array must be clocked three times (one full frame reset and two readouts of the full frame) the efficiency of this readout scheme is only 33% at the minimum integration time.

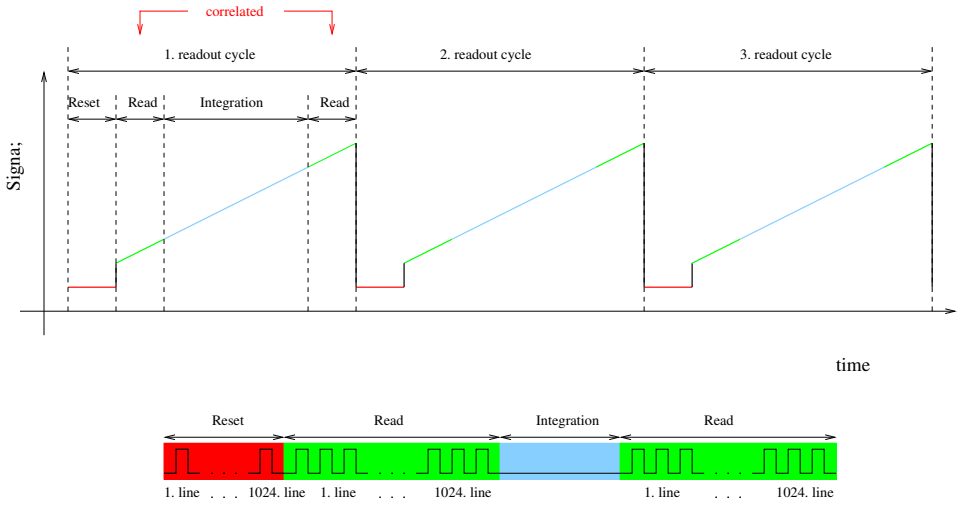

Figure 2.10: The timing diagrams of the signal and the control pattern for CDS (reset-read-read).

2.2.6 Correlated Double Sampling with Fast Reset (fcr)

The CDS can also be implemented with the fast reset scheme. This means that the reset and the readout of the reset level are carried out simultaneously and followed by the integration and the readout of the integrated video signal (Fig. 2.11). The result frame is provided by subtraction of the reset level from the integrated signal. Since the whole array is clocked only two times - once for the reset with the first readout and once for the second readout, the efficiency of this readout scheme is 50% for the minimal integration time. This readout mode was planned for scientific operation

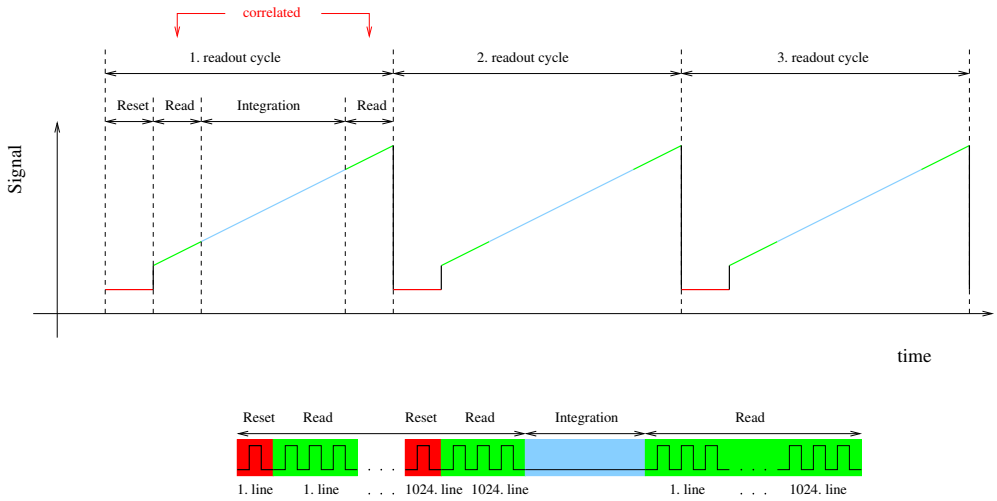

Figure 2.11: The timing diagrams of the signal and the control pattern for CDS with fast reset (reset-read-read).

2.2.7 Line-interlaced Read (lir)

The technique of the line interlaced read should guarantee the a more stable operation of image sensors because each line in the frame is read out twice before and after the integration. The readout cycle of this mode consists of two main parts: the clocking through the full array with a read-reset-read scheme and the integration (Fig. 2.12). The read-reset-read scheme means that each line in the complete frame is read out, reset and read out again, where the second readouts provide the reset level of the detector. The integration completes the first readout cycle then the second readout cycle starts with its read-reset-read scheme. The integrated photo signal is obtained by the first readouts of this scheme and the second readouts, after resetting, provide the reset levels for the next readout cycle. The result frame is produced by subtracting the reset level obtained in the first cycle from the integrated signal read out in the second one. The second cycle is also completed by integrating of the photo signal and a third readout cycle starts, which provides the integrated signal for the second cycle. Concerning the result frames, the reset level of the first frame comes from the first readout cycle and its integrated signal value form the second cycle. The reset level of the second frame comes from the second cycle and its integrated signal value from the third cycle, etc. As can be seen, the readouts of the lines in the adjacent readout cycles are interlaced in contrast to the previous modes, where each cycle carried out a complete readout of a frame line by line. After reading the whole array there is a pause if the integration time is above the minimal value and the cycle is repeated for as many images as required. Essentially no time is wasted, and for any integration time the efficiency of this mode is almost 100%. Since the line-interlaced mode also provides correlated double sampling, it is also used for scientific purpose.

2.2.8 Multiple End-point Read (mep)

This read out mode is similar to the double correlated read but here the readout cycle contains $2 \times n$ readouts instead of two. After the complete frame reset the full array is read out n times

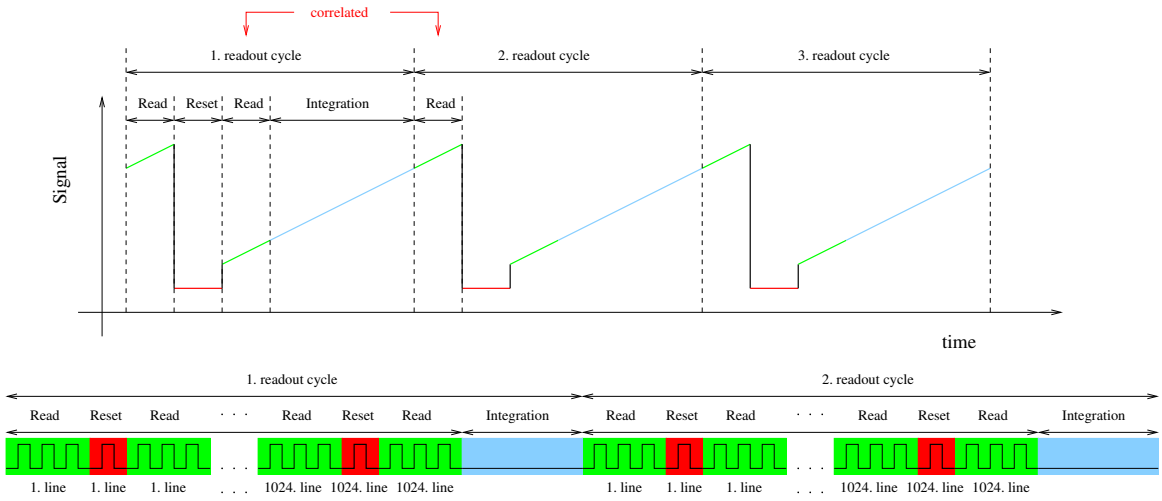

Figure 2.12: The timing diagrams of the signal and the control pattern for the line-interlaced read.

and the average of the n frames provides the bias values of the pixels after reset. After the integration the complete array is read out n times again and the average of these frames is taken as the integrated signal (Fig. 2.13). The video signal is the difference of the two averaged frames. Since the averaging of more frames helps to reduce the readout noise in the image, this read out mode provides a more accurate flux detection, which is advantageous for scientific purpose. This solution allows the chip to have a stable operation as well but the duration of one readout cycle is on order of seconds even if a fast reset is implemented, which may cause the minimal integration time to be too long.

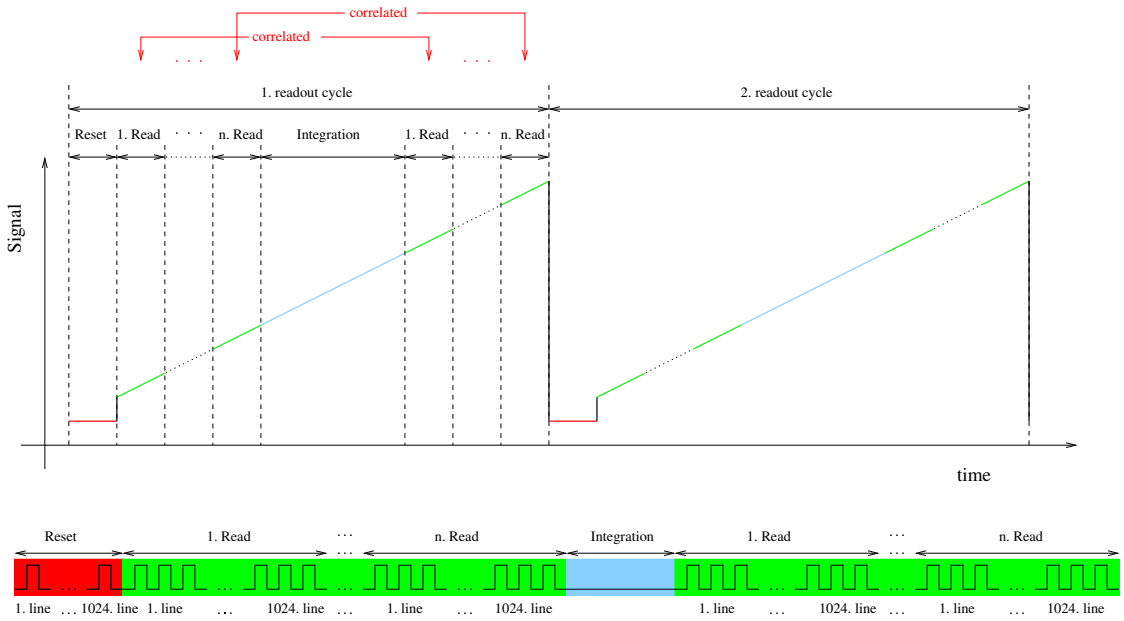

Figure 2.13: The timing diagrams of the signal and the control pattern for the multiple end-point read.

2.2.9 The choice of the readout modes for scientific operation

The aim of the technical part of this doctoral thesis was to implement and test the readout modes for HAWAII-2 FPA descried above. Since there were varius readout modes available for scientific purposes, we tested them in order to choose the one of them allowing for the best performance of the detector. We used several criteria to measure the performance. The most important criterion we used to compare the different solutions with each other was the image quality produced in these readout modes. The multiple-end point read with the averaging of the measured pixel vaules provides a stable operation of the HAWAII-2 chip and the best image quality, comparing with the other readout modes in the same conditions.

Considering the efficiency of the readout modes, the line-interlaced read is the favorable with its almost 100 % efficiency comparing with the Correalted Double Sampling with normal reset and fast reset providing efficiencies of 33% and 50% for the minimal readout time. The multiple-end point read have also only an efficiency of 33% or 50%, depending on the realization of normal or fast reset. However, the readout time of the full array is a critical parameter as well and its length depends on the scheme of the readout mode. The minimal readout time is longer in the line-interlaced mode than that of the CDS with and without fast reset which may be enough to saturate the detector in K-band imaging. This problem is more pronounced for the multiple-end point read, where the readout time is even longer. Therefore the implementation of these readout modes involves an optimization of the readout process aiming for the reduction of the readout time of the full array as much as possible. The efficiency and the readout time together give the effective time needed to produce an image during observations. By increasing the efficiency and the reducing the readout time, we also reduce this effective time, which is important for an optimal usage of the telescope time.

Thus the performance of the HAWAII-2 image sensor operating in these readout modes is measured in terms of the three criteria, the image quality produced in a stable detector operation, the efficiency of the detector operation, and an optimal readout time of the FPA. A compromise between the best image quality, the maximal efficiency, and the shortest readout time results in the best choice of the readout modes. In the next chapter we present our solutions to the implementation of these readout modes together with their tests, where we consider the techniques which can facilitate the optimal performance of the detector with respect to the three criteria mentioned above.

Chapter 3

Optimizing of the Operation of HAWAII-2 FPA

In this chapter we present results related to the optimization of the camera operation for the OMEGA2000 instrument. The aim of this optimization was to achieve the best possible performance of the HAWAII-2 FPA installed in the camera. The OMEGA2000 NIR wide field imager was designed for a background-limited operation, which determined the possibilties for the implementation of its optimal readout process. A very slow operational mode of the imager could not be a goal, even if it would assure a stable operation with favorable noise-properties, since a readout of full HAWAII-2 array taking too long might saturate the detector with the incident signal, especially in the K-band imaging. Therefore, the main task was to achieve as fast and stable operation of the HAWAII-2 detector as possible while keeping its readout noise below the photon shot noise of the background and producing the best possible image quality. This task constituted the technichal part of this dissertation and we will discuss it in this chapter. In the fist section of the chapter we concentrate on the optimal design of the readout process and investigate how the maximal attainable frame rate for the HAWAII-2 FPA can be realized. In the second section, we present the techniques applied for optimization of the camera operation and consider the problems related to the image quality produced at high data rate and then describe the solutions to these problems. As a result of these optimizing techniques, the OMEGA2000 camera could operate at an appropriate frame rate, i.e., the $K-$band imaging was feasible, and the image quality was also satisfactory for scientific purposes. MPIA had the opportunity to test the operation of OMEGA2000 camera with three different HAWAII-2 focal plane arrays with the serial numbers #37, #48 and #77. Here, we describe the probelms occurred in the operation of these specimen installed in the OMEGA2000 camera and discuss their solutions. The tests of the camera performance with the various image sensors after optimization of readout process will be presented in the next chapter.

3.1 Optimizing of the Detector Readout

In the previous chapter presenting the HAWAII-2 FPA, we saw that the operation of the chip is based on several factors. Its different output modes or the different implementations of the readout process provide some free parameters for the optimization of the camera operation. In an

optimal design of the control of HAWAII-2 FPA, all the free parameters in readout process of the array had to be fine-tuned so that the best performance of the image sensor could be achieved. These free parameters are incorporated in different possibilities to implement the operation of the chip, such as the choice of the output mode, application of different mode of the idle cycles of the image sensor, adjustment some of the *analog signals* operating the chip and implementing of an optimal timing of the readout process, i.e., design an optimal pattern for its *digital control signals*. In the followings these possibilities will be discussed. We start with the considerations related to the choice of the output mode of the data transfer from the HAWAII-2 chip. Then we present the solution of the handling of idle cycles in the readout process of the FPA. It is followed by a brief summary on the on fine-tuning of the analog controls signals of the chip and we finish this section with the discussion how we found the optimal design of the clocking of the digital control signals of the HAWAII-2 FPA.

3.1.1 The Choice of the Output Mode

The first step for the optimal design of the readout process was and the choice of the output mode. As described in the previous chapter, the HAWAII-2 chip has three output modes, the Single Output Mode, the Eight Output, Unshuffle Mode and the Eight Output, Shuffled Mode. Since in the Single Output Mode only one channel is used for the data transfer, the array operates at a lower data rate than in the other two modes. In the specifications obtained from the Rockwell Company the maximal data rate (or frame rate) of the HAWAII-2 FPA is 100 kHz (or 0.25 Hz) for the Eight Output Modes. This gives a readout time of 4 s for a full frame with CDS and it is even more in the Single Output Mode. The Shuffled Mode with eight outputs was provided for the detector so that accidental stripe patterns in the images due to systematic effects could be eliminated. However, the shuffling increases the data transfer time and we expected the systematics effects will be suppressed by the dominating background noise.

Therefore we implemented only the Single Output Mode and the Eight Output, Unshuffled Mode for the purpose of the detector test. We created two sequences of instructions initializing the readout process of the detector for both the modes. The digital inputs O1 and O2 of the HAWAII-2 FPA for controlling its output modes are set to the proper values (see Tab. 2.2) in these sequences sent to the HAWAII-2 chip by the readout electronics.

Although we preferred the Eight Output Modes to the Single Output Mode for scientific operation of the HAWAII-2 FPA by virtue of its speed, some artifacts due to the higher data transfer rate appeared in the frames and these unwanted effect could only be reduced by applying the Single Output Mode. This was the case during the scientific operation of HAWAII-2 FPA #77, where a gradient appeared in its each quadrant in the Eight Output Mode. This will also be discussed in the last section of this chapter.

3.1.2 Application of different modes for the idle cycles

We saw in the previous chapter that the readout process of the HAWAII-2 chip is organized in units, so called readout cycles. Each readout cycle provides a complete image information, i.e., one or two frames depending on the readout mode. However, the control patterns of these cycles can implemented without reading the pixel values as well, where the full array can be clocked

through without sampling the video signal. The difference between the implementations of the control patterns is the presence or the absence of the start of conversion signals (SCON) sent to the A/D converters. The other control signals are all the same in the both cases so they operate the chip in the same way. The readout cycles implemented without the sampling of the video signal are called *idle cycles*. Since the HAWAII-2 FPA can run in idle cycles between the readouts without any interrupt, the idle cycles are useful to stabilize the state of the image sensor. If the readout of the FPA is started and finished without changing its operation, we can avoid the transient feature in the video signal due to the modifying the state of chip circuits.

There are two solutions applied to start of the readout process in idle-mode: the idle-wait and idle-break mode. In the first mode the software waits for the end of the current idle-cycle before starting the readout of the chip while in idle-break mode it interrupts the running of the actual idle-cycle and starts the readout immediately. The camera uses the idle-wait mode for normal operation, which assures the stable operation of the chip. However, if a series of frames with long integration times are taken the idle cycles between the readouts have also long duration times, which causes a long dead time in the readout process. In order to avoid this dead-time, the idle break mode should be used, in which the control software always stops the long idle cycles and starts the readout. We used idle-break mode to take series of dark frames of the HAWAII-2 chips with longer integration times increased up to 1000 s.

3.1.3 Fine tuning of the Analog Signals

In the previous chapter on the operation of the HAWAII-2 FPA the role of the analog control signals of the chips are discussed, among others. These analog signals, namely the bias voltages of the detector, can also be used to optimize the operation of the image sensor. The task is then to adjust them in the range of their nominal values and check performance of the detector with different timings of the digital control signals.

As seen in the Table 2.1, two of the bias voltages, BIASPWR and BIASGATE, have nominal values of 5 V and 3.5 V, respectively. In fact, BIASPWR should not be changed since it is the source voltage of the P-FET for accessing the unit cell. Nevertheless, BIASGATE can be modified in its nominal range (0-5.5V) without any problem, which changes the current control for the unit cell. By fine-tuning the current control, the speed and the dynamical range of the SF amplifier can be adjusted. The other analog input is VRESET, the reset level of the unit cells, which has a nominal range between 0.5 and 1 V. This means the BIASGATE and VRESET can be used together to find an optimal range of the operation of the detector. In order to assure a fast operation, the speed of the discharging of the unit cell should be increased. If fact the P-FET with BIASPWR and BIASGATE is a voltage driven current source and the current is proportional to the difference in the voltage between BIASPWR and BIASGATE (Fig. 2.5). By decreasing BIASGATE with constant BIASPWR, e.g. 5 V, the current discharging the unit cell capacitance can be increased. As a consequence, if BIASGATE is adjusted to a lower value, it increases the speed of the operation. The minimal value of BIASGATE could be 0V in its nominal range. However, at about its nominal value, 3.5 V, the P-FET starts to saturate and cannot increase the discharging current. Thus its optimal value must be in the near of the nominal one. Besides increasing the rate of the discharging, a smaller reset value could also make

shorter the discharging time. It means the value of VRESET should be set as small as possible. On the other hand the video signal must have a maximal dynamical range which allows us to measure the video signal more precisely. This requirement maximizes the value of VRESET. A trade-off between these two requirements gives roughly the values of the analog inputs. An optimal dynamical range, which takes about 4 μs, VRESET is set its maximal value, 1V, and BIASGATE is adjusted to 3.2 V. These values were used for the operation of the HAWAII-2 FPA in the OMEGA2000 camera.

3.1.4 Optimal Design of the Basic Timing

Besides the choice of the output mode with the fastest data transfer and the fine-tuning of the bias voltages, the main task was to design an optimal basic timing for the readout of HAWAII-2 sensor. As a goal of this task, we wanted to ensure a detector limited operation of the OMEGA2000 camera, i.e., we reduced the time needed for the readout of the full FPA while the operation of the chip had to remain stable. Hence, the main purpose for optimizing the pixel readout cycle was to increase the sampling frequency of the video signal to an upper limit beyond which the sampled signal would be distorted due to the interference and the transient behavior of the circuit components. Here, we discuss the solutions we applied to achieve this detector limited operational mode.

As already described in the previous chapter presenting the HAWAII-2 FPA, it operates in reverse bias mode. It means the capacitance of each pixel in the array is charged by applying a reset voltage and the charge carriers induced by the incident IR photons discharge these capacitances in an amount proportional to the number of the photo charges. The video signal is the voltage measured on the capacitances after discharging. The theoretical upper limit of the sampling and clocking frequency of the video singal of the HAWAII-2 FPA is determined by its transient time. After pulling the video signal up with the reset voltage at the beginning of the readout cycle of a pixel, we cannot sample the signal until it has reached its stable value, which takes about 4 μs with an optimal dynamical range adjusted with 1 V reset voltage and 3.2 V bias-gate voltage. The readout cycle time of one pixel is therefore altogether minimum 6 μs corresponding to a clock frequency of 166 kHz. Since the readout cycle of a pixel starts at the rising edge of the clock signal but the video signal is pulled up only at the falling edge, it allow us to increase the clocking frequency. We can use not only the time period of the low state of the clock signal (between the falling and rising edges) but also that of the high state of the clock signal (between the rising and falling edges) in the next cycle to cover the whole transient time of the video output. By applying a shorter low state of the clock signal, the next readout cycle will start earlier and the video output can be sampled before the falling edge of the clock signal in the next readout cycle. As a result, we have a readout cycle with a shorter duration time.

Fig. 3.1 compares the original readout process using the normal triggering with this solution. The FSYNC pulse (plotted with magenta in both the oscilloscope screens) controls the start of the readout of the full array with negative logic. The cycle time of a pixel readout spans the time axis from the first rising edge of the clock signal (plotted with green color) to the second one. The left hand panel shows the normal triggering where the cycle time covers the whole time needed for the video signal (plotted with yellow color) to decrease to its stable value after its

pulling-up. The transient time of the video output is delimited with the orange vertical markers. Here, the SCON signal (plotted with purple color) triggers the sampling of the video output at the end of the first readout cycle. The right hand panel displays the triggering delayed until the second falling edge of the clock signal. In this case, the video singal is also sampled in its stable state (SCON pulse plotted with magenta) but the next readout cycle starts (rising edge of the second clock pulse) before the video signal reaches its stable value. The only difference between the two pictures in Fig. 3.1 is the position of the FSYNC pulse. By positioning the trigger of the sampling in the second readout cycle, we eliminate the dead time between the sampling and the pulling up of the video output. As a result, we can decrease the cycle time in the second case.

Figure 3.1: The left hand panel displays the normal triggering of the video signal conversion of the first pixel in the FPA and the right hand one the triggering with delay. The clock signal (CLK1) is plotted with green color, the output singal of the video amplifier with yellow, the start signal of the sampling (SCON) with purple, and the frame synchronization signal (FSYNC) with magenta.

Another possibility to minimize the cycle time is to decrease the transient time of the video signal. It is about 4 μs when the signal RESETEN is high, i.e., we reset the column bus to cell-drain while there is no readout. If RESETEN is low the voltage difference between the pixels and the cell-drain becomes smaller, which decreases the transient time to roughly 2 μs. Thus, a minimal value of symmetric clock signal is reduced to $2 \times 2\mu\text{s} = 4\mu\text{s}$, i.e. the clock frequency can be 250 kHz. Although a stable video signal is sampled with all the methods, we used a pixel readout time of 6 μs (166 kHz) because ramps and stripes appeared at the edge of the frames taken with higher clock frequency. This problem will be discussed in the next section.

With a pixel readout time of 6 μs, the readout time of a full quadrant is $128 \times 1024 \times 6$ μs $= 786{,}432$ $\mu\text{s} \approx 0.79$ s in the Eight Output Mode and eight times more in the Singe Output Mode. This gives the minimal time needed to readout the HAWAII-2 FPA since its quadrants are read in parallel. However, the readout modes implemented for the OMEGA2000 camera contain more steps than a simple readout of the full array. Thus, the minimal readout time of the camera's readout modes is inherently longer than a read of the full array. In order to determine the time elapsed in a readout cycle of a given readout mode, we had to sum up the duration times of all the instructions used in that readout cycle. Since it was an important criteria to avoid the usage of any built-in interpeter making more complicated GEIRS (the control software of the OMEGA2000 instrument), this task had to be implemented with an externally runing program. I wrote a simple interpreter which processed the content of the instruction tables

Readout Mode	Min. readout time [s] Single Output Mode	Min. readout time [μs] Eight Output Mode
Single pixel read (spr)*	15.9	2,065,076
Reset level read (rlr)	6.31	799,945
Non-correlated sampling (rr)	6.31	792,249
CDS (o2dcr)	6.32	799,970
CDS with fast reset	6.32	799,945
Line interlaced read (lir)	12.6	1,599,771

Table 3.1: The minimal redout times of the implemented readout modes of HAWAII-2 FPA.
* For the single pixel read this value depends on the position of the pixel to read out. Here, we read out the 10.-th pixel located in the 6.-th line of each quadrant.

used for the various readout modes and calculated the total duration time of the readout cycle from the duration times of the instructions organized in loops. We could determine the minimal integration times for each implemented readout mode with this interpeter, which are shown in Tab. 3.1. In the table, the first three readout modes are for engineering purposes. The minimal readout times of the reset level read and the non correlated sampling are only negligibly higher than the theoretical limit. We need much longer time for the single pixel read depending on the position of the pixel specified to read out. The series of the line synchronization signals applied for reaching a given pixel of the array in each quadrant is very time-demanding, which increases the minimal readout time considerably for this mode. However, this time is critical only for the other three readout modes as they are to be used for scientific applications. CDSs with and without fast reset in the Eight Output Mode have minimal integration times of about 0.8 s, which are short enough to avoid the saturation of the FPA in K-band imaging. These readout modes in the Single Output Mode with ~ 6.3 s provide acceptable readout times for J- or H-band observations but cannot be applied in K-band surveys. In spite of that, the line-interlaced read is the most efficient readout mode and produces the minimal overhead between the frame readouts. The minimal frame readout time is 1.6 s in the Eight Output Mode, which still allows us to use this mode in J- and H-band imaging but might cause problems in K band. The Singe Output Mode is not available for the the line interlaced read because its minimal readout time is very long, 12.6 s, and during this time the HAWAII-2 FPA will saturate in all broad NIR bands. Altough the multiple end-point read with its frame averaging provides the most accurate photon flux detection, we did not implement it since this mode has the longest readout time. In the multiple-end point mode we need to read out at least four frames in order to produce one averaged image, which, considering the theoretical limit of the minimal frame readout time, gives a readout cycle time of 4×0.79 s $= 3.16$ s for the Eight Output Mode. This long duration time would make the application of this readout mode difficult even in J and H bands.

In this section we have considered how to design the basic timing of the readout process of the HAWAII-2 chip optimally. With the techniques described above, we minimized the duration time of the frame readout cycles of each readout mode implemented for the FPA. For the optimal design, there are three readout modes available for the OMEGA2000 camera for the scientific observations. In the Eight Output Mode the readout using CDS with or without fast reset can be applied in all NIR bands, while in the case of the line interlace read we must check if the properly

positioned baffle reduces the background noise enough to avoid the saturation of the detector in K-band imaging. The OMEGA200 instrument is still able to operate with both types of CDS in Single Output Mode but only for J and H-band surveys. The line interlaced read cannot be used in Single Output Mode. In the next section we present the test result of the operation of the HAWAII-2 FPA in these available readout modes and examine the quality of the imaging the camera produces. This will help us to chose the optimal configuration of the readout and output modes, thereby providing the best image quality for scientific purpose, without any feature or artifact.

3.2 Improving of the Image Quality

Even if the video signal is sampled correctly, artifacts might appear in the images, due to the transient effects in electric circuits operating at high clock frequency. Other unwanted couplings between the different parts of the electrical circuits can also degrade the image quality. In this section we consider these problems together with the techniques applied to eliminate these artifacts. The first part presents the problems due to the transient behavior of the electrical circuits of the HAWAII-2 FPA and the solutions to eliminate the artifacts related to the transient phenomena. In the second part we describe the problems caused by internal couplings between the electrical circuits of the FPA and the readout electronics. We also describe the solutions to this problem.

3.2.1 Transient Features in the Images

We saw in the previous section that the transient phenomena of the electrical signals limit the time resolution of the readout process. The video signal cannot be sampled until it reaches its stable value and this imposes a time constraint on the pixel readout. Besides this transient feature, there is another effect related to the video signal which must also be considered. In the beginning of each line, indicated by a pulse of LSYNC, a drift in the video signal can be measured, even if we sample the signal in the stable range. Fig. 3.2 showing the control singals and the video output of the HAWAII-2 FPA demonstrates this feature. The left hand panels shows the start of a frame readout after resetting the full array. In the left hand side of the oscilloscope screen we can see the video signal measured in the last few pixels in the whole frame to be reset. The FSYNC pulse, plotted with magenta, starts the readout of the next frame. The right hand side of the screen shows this readout process, where the video signal of the first few pixels are increasing only gradually up to the average value of the local area in the next frame. The right hand panel shows the same phenomena but after the integration of the video signal. Here, the video output is not active during the integration and has a gradual increase in its value for the first few pixels, as in the previuos case.

Since the same drift occurred both after reset and after integration, it should not cause any problem for the readout modes with CDS. By subtracting the reset frame from the integrated one, the gradient in the pixel values could be eliminated if the rate of the drifts were the same in both frames. However, narrow stripes appeared at the border of the image as a result of the subtraction, indicating that the drift rates were different. Since the amplitude of this difference

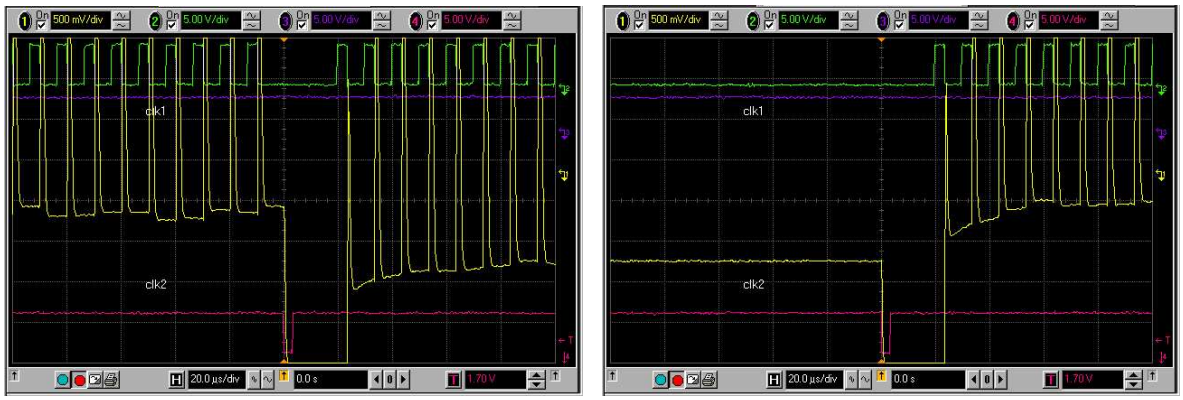

Figure 3.2: The left hand panel shows the drift in the video signal after reset and the right hand one displays it after integration. The clock signal (CLK1) is plotted with green color, the output singal of the video amplifier with yellow, and the frame synchronization signal (FSYNC) with magenta.

was on the order of 100 mV, representing about 1300 ADU, it became dominant only in low signal level, as demonstrated in Fig. 3.3.

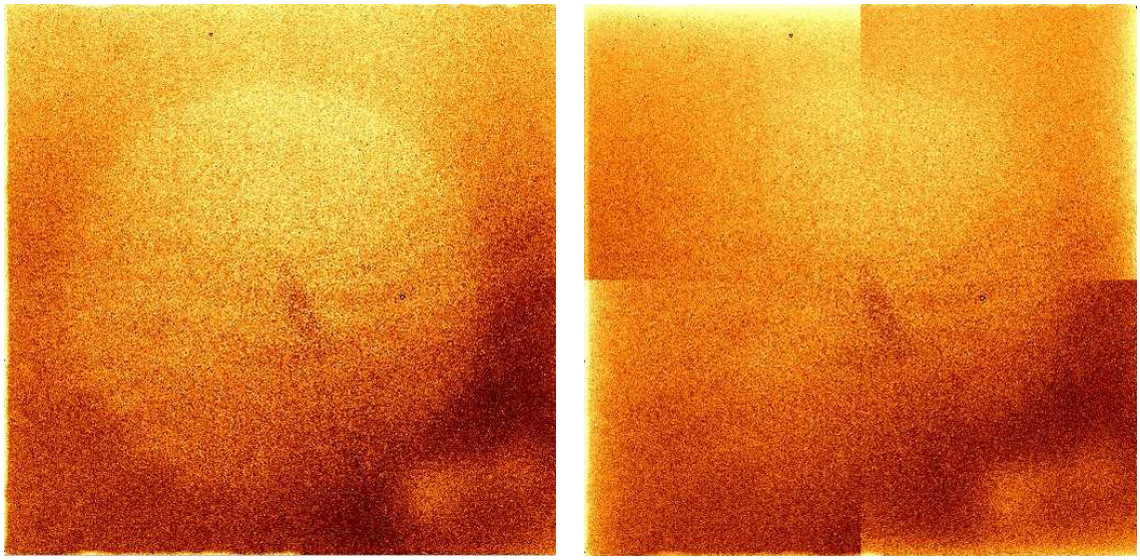

Figure 3.3: The left hand panel shows a frame taken with the FPA #37 with higher incident flux, 20,000 ADU on the average, and the right hand one displays a frame taken with the weakly irradiated detector, producing only $\sim$ 5000 ADU. The latter exhibits drifts at the outer edges of the quadrants.

A similar behavior was observable for the last pixels in each row, where the signal value was considerably higher than the average signal of the previous pixels. Fig. 3.4 shows the readout of the last few pixels in a row. The last pixel value is on the order of 100 mV, i.e., $\sim$ 1300 ADU, higher the those of the previous pixels in the same row. The origin of this anomaly is hard to explain. While in the previous case, the drift was due to the transient features of the electrical circuits after changing their state, this explanation does not apply to this situation. The triggering of line synchronization signal at the end of readout cycle of the last pixel cannot

effect on the pixel value already at the beginning of the readout cycle. In any case, this difference did not cause any feature in the frames taken in the readout modes with CDS, since it was only a bias value superposed in the reset frame, which could be eliminated by subtracting it from the integrated frame.

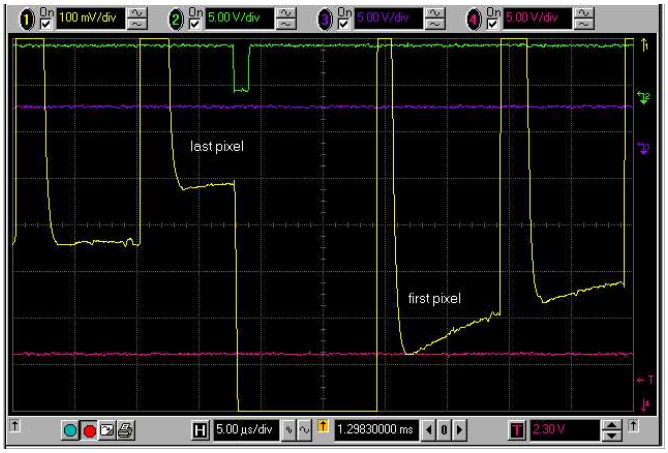

Figure 3.4: The deviation of the value of last pixel from those of the previous pixels in an arbitrary row of the array. The the line synchronization signal LSYNC is plotted with green color, the output singal of the video amplifier with yellow.

3.2.2 Artifacts caused by internal Couplings

All the implemented readout modes were tested with the three HAWAII-2 FPAs operating . with clock frequencies between 150 and 250 kHz and we checked the quality of the images they produced. The noise statistics of the frames taken with different clock rates did not change dramatically but some artifacts degrading the image quality appeared at higher clock frequencies. In the case of FPA #37 and FPA #77 , a typical problem was that the different groups of channels had different offsets in the frames of low signal level taken in CDS mode with fast reset (Fig.3.5). With slow reset or in line-interlaced mode, only a gradient or a ramp in the pixel values appeared in the quadrants but this artifact had a non-linear behavior, i.e., it did not scale with the average signal level. We used slower clock rates down to 150 kHz but the ramps could not be eliminated. This phenomenon might be caused by some unknown coupling problem between the multiplexer of the detector and the data bus of the readout electronics. Whatever the cause, we did not observe any similar feature in the images produced with the FPA #48 in the traditional CDS with the clocking frequency of 166 kHz.

In the case of the specimen #48 another issue emerged. Here, the readout in CDS mode with fast reset also caused some drift in the dark fames which could be observed in each channel (Fig. 3.6). This indicated that there is drift in the reset level along the rows of the pixel array in all the quadrants. The drift was not present in the traditional CDS mode, so we used this mode in the the science run, even though it is more time-consuming because of its less efficient readout scheme.

The observations carried out with two of the HAWAII-2 detectors are listed in Tab. 3.2. FPA #48 was used for the observations in September 2003 and OMEGA2000 provided data of good

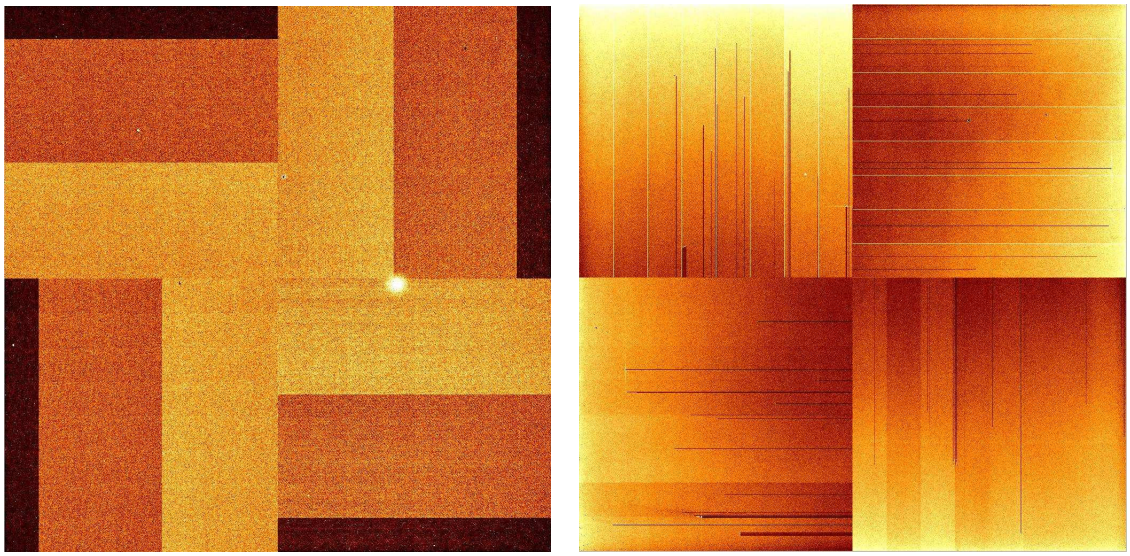

Figure 3.5: Dark frames produced by the FPA #37. The left hand panel shows a image taken with fast reset and the right side one displays an image taken in conservative CDS mode.

Observation	Used filters	FPA
September 2003	J_1, H, K	#48
November 2003	J_1, H	#77
April 2004	J_1, J_2, H	#77

Table 3.2: Observations with two specimen of the HAWAII-2 FPA in the OMEGA2000 camera.

quality. In November 2003 and in April 2004, the camera was operating with the FPA #77 in the Single Output Mode because the ramps present in the frames were less steep in this mode. The ramps could not be completely flatfielded out, but the preliminary results of the data reduction were satisfying. The one drawback was the increased overhead due to the slower output mode.

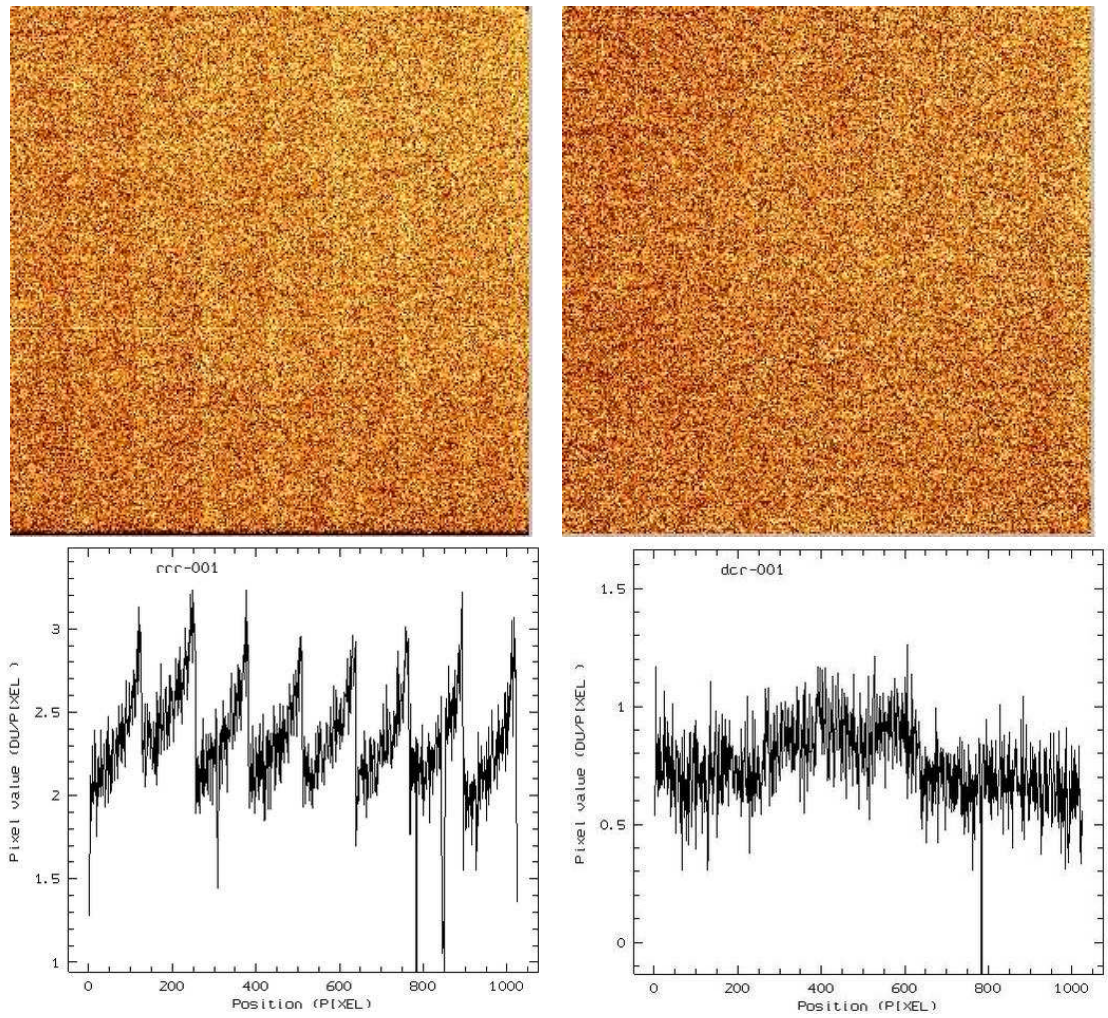

Figure 3.6: The two upper panel display the right lower quadrants of the dark frames taken in CDS mode with fast reset (left hand panel) and in conservative CDS mode (right hand panel) with FPA #48. The lower panels give cross sectional views of the summed signal values over the whole arrays for the same frames.

Chapter 4

Performance of the HAWAII-2 FPA

In this chapter we present the results of the detector tests and discuss the performance of the HAWAII-2 FPAs operating in the OMEGA2000 camera. In order to give a comprehensive view of the performance of a detector, we have to test its operation by measuring its various properties. As we optimized the operation of the HAWAII-2 FPA in the OMEGA2000 camera, we carried out a series of tests with the three specimen of HAWAII-2 FPAs, #37, #48, and #77, to characterize their most important properties. During the tests, we measured and compared their noise properties, dark current statistics, quantum efficiency and linearity, providing a more comprehensive view on the performance of this detector family.

4.1 Noise Properties of the Image Sensor

In astronomy the goal of the imaging is to measure the photon flux, i.e., the rate at which photons impinge on each point in the field of view. Focal plane arrays are therefore designed and manufactured in that way to reach as maximal sensitivity to illumination as possible. However, there is always a wide variety of features and artifacts appearing in the captured images, which was not present in the incoming photon flux. These unwanted features and artifacts superimposed on the input signal by the imaging system are specified as noise degrading the image quality. Besides the sensitivity, another aim of the detector design is to minimize or control the sources of noise, since noise is what ultimately limits the overall performance of a camera. In an ideal digital camera, the performance is limited by the photon noise or the noise of the image sensor and not by that of the system electronics.

The noise sources are usually classified in two categories: *temporal or random noise sources* and *spatial or pattern noise sources*. The temporal or random noise is not constant from frame to frame in the image and it can be reduced by applying longer exposure time for a frame, i.e., increasing the signal-to-noise ratio, or averaging successive frames. Statistical momenta, such as the average, root mean square and median, are useful tools to describe the statistical properties of random noises. Typical temporal noises are the shot noise, reset noise, output amplifier noise and dark current shot noise. The spatial noise does not change significantly from frame to frame and it cannot be reduced by increasing the exposure time or averaging successive frames. However, frame subtracting and gain or offset correction techniques are able to reduce some kinds of spatial noise. The pattern noise is described in terms of the variation in the signal values of

the individual pixels under uniform illumination. This kind of noise has major components, such as fixed pattern noise, photo-response non-uniformity and dark current non-uniformity. In this section we give a short overview on some of the noise types

4.1.1 Photon Shot Noise

There exists a noise source which is not associated with the intrinsic properties of light detection systems but with the discrete nature of photons. The random arrival of the photons at any detector causes a random generation of the photo-electrons in the detector material and therefore an inevitable statistical fluctuation in the rate of the photo-charge accumulation and in turn in the video signal. The shot noise of the photons draws a fundamental limit on the performance of imagers and it is important to determine its contribution to the total noise of the system. This type of noise does not depend on the frequency of the light illuminating the detector, so it is a white noise.

If the photon flux incident on a unit area of the sensor during a unit time is $I(t)$, then the number of photons received on that unit area during the exposure time between t_0 and t_1 is

$$n = \int_{t_o}^{t_1} I(t)dt \ . \tag{4.1}$$

Since the shot noise has a Poisson statistical distribution, i.e., the time between photon arrivals is specified by Poisson statistics, the uncertainty in the number of photons collected during the given period of time is

$$\sigma_{shot} = \sqrt{n} \ . \tag{4.2}$$

The useful data range of HAWAII-2 resides between 0 and 65535 and its linear regime is measured to be up to about 40,000 ADU for each specimen, as we will see it in the Section 4.4. Since the output signal conversion gains of the detectors are roughly $5e^-$/ADU, their linear full well capacities are about $200,000e^-$. If we take the quantum efficiency of the photo sites to be almost unity, the average number of photons in the incoming flux has the same order and the shot noise will be $\sigma_{shot} = \sqrt{200,000} = 400$ ($\sim$ 100 ADU). We use only about two third of the full dynamical range of the detector for the observations. Therefore, the shot noise of the signal coming from the target objects typically $\sqrt{2/3}$ times smaller than σ_{shot} derived for the full dynamical range, which gives about 80 ADU. This value should be compared with the infrared background noise so that we could determine whether the observations will be limited by the shot noise of the singal or by the background.

4.1.2 Reset Noise

As mentioned in the previous chapter, a typical active pixel sensor applies a source-follower amplifier with a sense node capacitance to convert the photo-generated signal from the charge domain to the voltage domain. In the beginning of every readout cycle each pixel of the camera is reset to some reset level, V_{res}. It means that the sense node capacitance is charged through the resistance of the reset MOSFET channel to reach the voltage V_{res}. Nevertheless, there is always an uncertainty in this voltage due to thermal noise generated by the MOSFET channel

resistance. This uncertainty is referred to as the reset noise and it depends on not only the temperature but also the noise equivalent bandwidth (NEB) Δf of the channel. The latter is defined defined by the expression

$$\Delta f = \frac{1}{|A(0)|^2} \int_0^\infty |A(f)|^2 df \quad , \tag{4.3}$$

where $A(f)$ the transfer function of the cannel, and it gives the cut-off frequency of an ideal filter with a power spectral density equivalent to a real one. Any real filter can be replaced by its ideal pair if its response to the white noise superimposed on its input has the same power spectral density as the real filter. The definition of the noise equivalent bandwidth can be seen in Fig. 4.1, where this cut-off frequency of the ideal filter has the value for which the two shaded areas are equal. Then the RMS of the reset voltage is expressed as

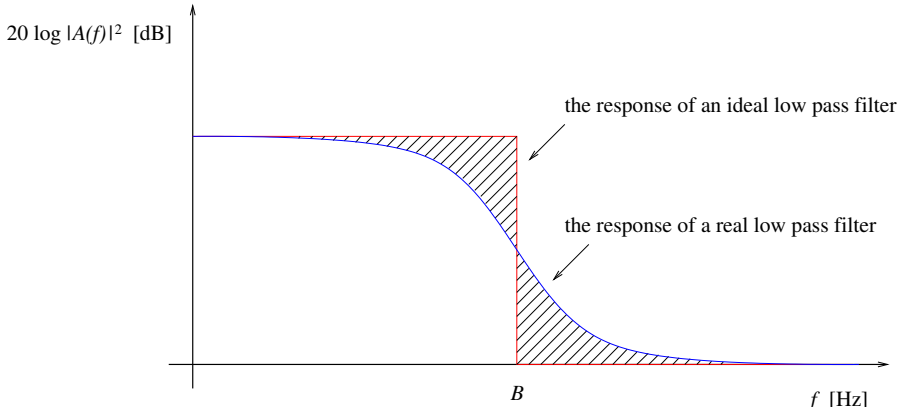

Figure 4.1: The definition of the noise equivalent bandwidth. The shaded areas are equal.

$$\sigma_{res} = \sqrt{4kT\Delta f R} \quad , \tag{4.4}$$

where k is Boltzmann's constant, T is the temperature and R is the effective channel resistance. Normally a RC low pass filter with the transfer function

$$A(f) = \frac{1}{1 + j(f/f_0)} \qquad f_0 = \frac{1}{2\pi RC} \quad , \tag{4.5}$$

provides a good approximation of the noise channel models for resetting of the output nodes of CCDs or Active Pixel Sensors. Its noise equivalent bandwidth has the simple form

$$\Delta f = \int_0^\infty \left| \frac{1}{1 + j(f/f_0)} \right|^2 df = \int_0^\infty \frac{1}{1 + (f/f_0)^2} df = \frac{\pi}{2} f_0 \tag{4.6}$$

that is

$$\Delta f = \frac{1}{4RC} \quad , \tag{4.7}$$

which can be substituted in Eq (4.4) and we obtain that

$$\sigma_{res} = \sqrt{\frac{kT}{C}} \quad . \tag{4.8}$$

It is more convenient to express this value in terms of electrons so that we can compare it with the number of electrons accumulated in the well capacitance. Since the accumulated charge in the sense node capacitor is $nq = CV_{res}$, where n is the number of electrons, q is the fundamental charge and C is the sense node capacitance, the RMS of the reset noise in terms of electrons is

$$\sigma_{res} = \frac{\sqrt{kTC}}{q} \quad . \tag{4.9}$$

Because the two free parameters are only the temperature and the sense node capacitance in this equation, the reset noise is also called kTC noise. By reducing the free parameters, the reset noise can be decreased. The tradeoff is that the lower the sense node capacitance, the smaller the dynamical range of the photo-sites. According to the specification of HAWAII-2 detector, its unit cells have a sense node capacitance of 28-35 fF (Haas, 2002). Therefore, at the temperature of 77K we expect a maximal reset noise generated on the sense node capacitance to be $\sigma_{res} \approx 40e^-$, i.e., about 10 ADU. This value is one order less in magnitude than the expected photon shot noise, hence it is negligible in the background limited operation of the imagers.

4.1.3 Readout Noise

The two primary sources of the readout noise of the imaging sensors are the *thermal* and the *flickering noise* generated in the output amplifier. The thermal noise is a white noise, i.e., it is independent of the operation frequency of the circuit, while the flickering noise is frequency dependent. This means their contribution to the total readout noise is varying in different domains of the frequency scale.

Thermal or White Noise

Not only the reset MOSFET but also the transistor of the output amplifier of the detector has a resistance that causes thermal noise. This kind of white noise, sometimes called Johnson noise, can be described with a similar expression in volts as the reset noise,

$$\sigma_{th} = \sqrt{4kT\Delta f R_{out}} \qquad [\mathrm{V}] \ , \tag{4.10}$$

but here the resistance R_{out} denotes the output impedance of the source follower amplifier. If the g is the gain of the image sensor, then the thermal noise in electrons can be written as

$$\sigma_{th} = \frac{\sqrt{4kT\Delta f R_{out}}}{g} \qquad [e^-] \ . \tag{4.11}$$

With the output impedance of a few Ohms and about the same noise equivalent bandwidth as the reset noise has, this noise for the HAWAII-2 detector with a gain of $\sim 4\mu\mathrm{V}/e^-$ has the same order as its reset noise.

Flicker or $1/f$ noise

Another natural noise source in electrical circuits produces a noise with an amplitude approximately inversely dependent on the frequency. It is called flicker or $1/f$ noise because of its

frequency dependence. The higher clock frequency a system is driven on, the lower the noise, hence it causes no problem for fast readout circuits and it can only be the dominant noise component for the imagers operated with low pixel rate. Quantitatively, if we increase the clock frequency by one order of magnitude then the noise power decreases also by a factor of 10 and the RMS of the noise current is

$$\sigma_{1/f} = i_s \sqrt{\frac{\Delta f}{f}} \quad , \tag{4.12}$$

where i_s is the signal current, Δf is the noise equivalent bandwidth of the output amplifier and f is its operational frequency. The typical source of the 1/f noise is any junction in the circuits, namely the traps of electron states at the silicon-oxide interface of the MOSFET switches. The variations of the electron states exhibit different characteristic time constants related to the different charge traps and the superposition of these variations, each with its own time constant, generates the $1/f$ noise spectrum.

If the detector is clocked slowly the 1/f noise is the natural noise limit but by increasing the frame rate at the 1/f corner frequency the device becomes white noise limited.

4.1.4 The Photon Transfer Curve

An efficient analysis for the noise characteristics of an imager is to determine its photon transfer curve, which provides the read noise floor, the conversion gain, the full well capacity and the dynamical range of the detector. Such a plot can be obtained by taking a series of flatfielded images with different exposure times, or with different signal intensities, and measuring the mean and the variance of the pixel values in a fixed area of all the images. The photon transfer curve then, is the graph of the variance as a function of mean pixel values. The method of determination of the read noise and the gain from this plot is very simple. The conversion gain of an image sensor is defined as the ratio of the number n_e of the photo generated electrons to the video signal s in ADU,

$$g = \frac{n_e}{s} \qquad \left[\frac{e^-}{\mathrm{ADU}}\right] \quad . \tag{4.13}$$

Since the number of the photoelectrons also exhibits a Poisson's distribution caused by the photon shot noise, its variance can be expressed in the term of the gain and the video signal

$$\sigma_e^2 = n_e = gs \quad . \tag{4.14}$$

The major noise components of a bias subtracted image should be this random noise exhibiting Poisson statistics and the readout noise of the detector. By adding their standard deviations in quadrature, we obtain the noise of the total signal in electrons,

$$g\sigma_s = \sqrt{\sigma_e^2 + \sigma_{ro}^2} \quad , \tag{4.15}$$

or the the variance of the total signal

$$\sigma_s^2 = \frac{1}{g} s + \frac{1}{g^2} \sigma_{ro}^2 \quad , \tag{4.16}$$

which is a relation between the variance and average signal intensity. In fact, the photon transfer

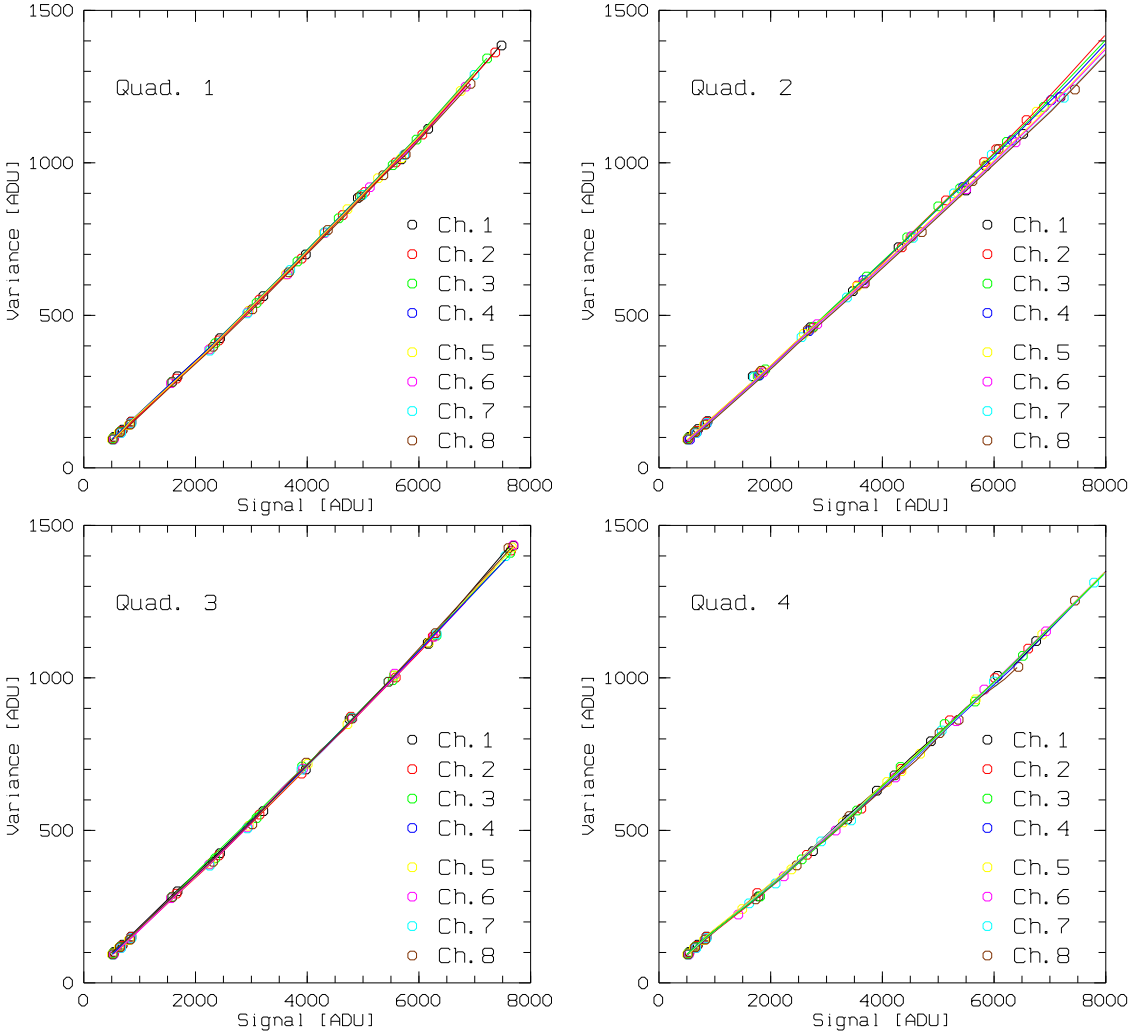

Figure 4.2: The photon transfer curve for each quadrant of the FPA #37.

curve is not linear but it has different characteristic regimes. In the first regime, at lowest signal values, the operation of image sensors is dominated by the readout noise and the curve is flat. The intersection of the transfer curve and ordinate axis gives the theoretical value of the readout noise floor, $(\sigma_{ro}/g)^2$. As the signal level increases, the camera operation becomes shot noise or background limited. This is the second regime, where the photon transfer curve has a slope of g^{-1}, i.e., its tangent determines the signal conversion gain of the detector. The third range represents the pattern noise limited operation of the imager. Here, the noise is proportional to the signal level, which means the slope of the photon transfer curve is unity in the log-log plot.

In order to determine the readout noise and the gain of the HAWAII-2 detectors, flatfield images were taken with constant illumination through a narrow band filter (NB1083) with different exposure times. After flatfielding them, the median and the variance of the pixel values in each channel of the arrays were measured in the frames and averaged for each quadrant. These values gave the photon transfer curves of the imager. The first, readout noise limited regime was very small compared to the shot noise limited one. Even if the detectors were very weakly illuminated, on the order of 1000 ADU, the operation of the imagers were shot noise limited.

Quad./Ch.	Fitted $(1/g)$	g (e^-/ADU)	Fitted $(\sigma_r/g)^2$	σ_r^2 (ADU)
Quad. 1				
Ch. 1.	0.1786	5.60	1.7130	53.7
Ch. 2.	0.1773	5.64	2.1369	67.98
Ch. 3.	0.1751	5.71	3.5764	116.65
Ch. 4.	0.1755	5.70	2.9699	96.42
Ch. 5.	0.1733	5.77	3.9987	133.14
Ch. 6.	0.1679	5.96	4.5716	162.17
Ch. 7.	0.1775	5.63	1.9586	62.17
Ch. 8.	0.1713	5.84	3.5667	121.55
Quad. 2				
Ch. 1.	0.1966	5.09	-2.0739	-
Ch. 2.	0.1892	5.29	1.1052	30.87
Ch. 3.	0.1843	5.43	3.1954	94.08
Ch. 4.	0.1882	5.31	0.7883	22.26
Ch. 5.	0.1849	5.41	1.4673	42.92
Ch. 6.	0.1905	5.25	-2.1159	-
Ch. 7.	0.1815	5.51	1.4328	43.49
Ch. 8.	0.1826	5.48	0.6488	19.46
Quad. 3				
Ch. 1.	0.1864	5.36	5.9957	172.56
Ch. 2.	0.1818	5.50	0.2913	8.81
Ch. 3.	0.1883	5.31	3.8819	109.48
Ch. 4.	0.1862	5.37	2.9250	84.37
Ch. 5.	0.1849	5.41	2.7540	80.55
Ch. 6.	0.1908	5.24	-1.0344	-
Ch. 7.	0.1862	5.37	0.7624	21.99
Ch. 8.	0.1813	5.52	2.2328	67.93
Quad. 4 3				
Ch.1.	0.1945	5.14	2.4648	65.15
Ch.2.	0.1934	5.17	1.9898	53.2
Ch.3.	0.2007	4.98	-2.1223	-
Ch.4.	0.1976	5.06	-1.9213	-
Ch.5.	0.1874	5.34	3.3340	94.94
Ch.6.	0.1922	5.20	1.9204	51.99
Ch.7.	0.1933	5.17	-1.2340	-
Ch.8.	0.1924	5.20	-3.2398	-

Table 4.1: The gain g and the readout noise σ_r measured for each channel of the HAWAII-2 FPA #37.

Quad./Ch.	Fitted $(1/g)$	g (e^-/ADU)	Fitted $(\sigma_r/g)^2$	σ_r^2 (ADU)
Quad. 1				
Ch.1	0.2344	4.27	1.9979	36.35
Ch.2.	0.2301	4.35	1.8634	35.20
Ch.3.	0.2201	4.54	1.8648	38.51
Ch.4.	0.2330	4.29	1.7869	32.90
Ch.5.	0.2415	4.14	1.8383	31.53
Ch.6.	0.2418	4.14	1.8636	31.87
Ch.7.	0.2202	4.54	1.6704	34.46
Ch.8.	0.2482	4.03	1.8523	30.06
Quad. 2				
Ch.1.	0.2029	4.93	1.5180	36.86
Ch.2.	0.2121	4.72	1.7969	39.96
Ch.3.	0.2039	4.90	1.7956	43.19
Ch.4.	0.2352	4.25	1.7484	31.60
Ch.5.	0.2404	4.16	1.6821	29.12
Ch.6.	0.2451	4.08	1.6565	27.57
Ch.7.	0.2489	4.02	1.6740	27.03
Ch.8.	0.2476	4.04	1.7355	28.32
Quad. 3				
Ch.1.	0.2130	4.70	1.0705	23.60
Ch.2.	0.2143	4.67	1.0794	23.52
Ch.3.	0.2037	4.91	1.1203	27.00
Ch.4.	0.2304	4.34	1.2721	23.97
Ch.5.	0.2013	4.97	1.3732	33.88
Ch.6.	0.2258	4.43	1.5482	30.36
Ch.7.	0.2114	4.73	1.5859	35.49
Ch.8.	0.2169	4.61	1.3775	29.29
Quad. 4				
Ch.1.	0.2077	4.81	1.5186	35.20
Ch.2.	0.2483	4.03	1.1290	18.32
Ch.3.	0.2319	4.31	1.4456	26.87
Ch.4.	0.2067	4.84	1.4966	35.04
Ch.5.	0.2444	4.09	1.5238	25.52
Ch.6.	0.2451	4.08	1.6973	28.25
Ch.7.	0.2465	4.06	1.7926	29.50
Ch.8.	0.2306	4.34	1.8150	37.60

Table 4.2: The gain g and the readout noise σ_r measured for each channel of the HAWAII-2 FPA #48.

Quad./Ch.	Fitted $(1/g)$	g (e^-/ADU)	Fitted $(\sigma_r/g)^2$	σ_r^2 (ADU)
Quad. 1				
Ch.1.	0.2059	4.86	2.1565	50.8
Ch.2.	0.2102	4.76	1.4323	32.48
Ch.3.	0.2166	4.62	3.2364	69.01
Ch.4.	0.2084	4.8	0.2134	4.92
Ch.5.	0.2041	4.9	-2.2312	-
Ch.6.	0.2066	4.84	3.8764	90.83
Ch.7.	0.2200	4.54	2.3432	48.4
Ch.8.	0.2082	4.8	5.6544	130.41
Quad. 2				
Ch.1.	0.1883	5.31	1.3214	37.26
Ch.2.	0.1872	5.34	-2.4325	-
Ch.3.	0.1957	5.11	3.2784	85.59
Ch.4.	0.1921	5.21	2.4324	65.93
Ch.5.	0.1983	5.04	6.3476	161.45
Ch.6.	0.1946	5.14	1.7654	46.63
Ch.7.	0.1887	5.3	8.5436	239.82
Ch.8.	0.1971	5.07	-1.3221	-
Quad. 3				
Ch.1.	0.1942	5.15	4.5435	120.45
Ch.2.	0.1956	5.11	3.4656	90.54
Ch.3.	0.2059	4.86	-1.4324	-
Ch.4.	0.2105	4.75	2.4343	54.92
Ch.5.	0.1966	5.09	0.8776	22.71
Ch.6.	0.2043	4.90	2.3243	55.7
Ch.7.	0.2028	4.93	1.4355	34.91
Ch.8.	0.2102	4.76	4.3463	98.35
Quad. 4				
Ch.1.	0.2234	4.48	1.9615	39.32
Ch.2.	0.2352	4.25	2.7455	49.63
Ch.3.	0.2256	4.43	6.8767	135.07
Ch.4.	0.2101	4.76	-1.2423	-
Ch.5.	0.2089	4.79	4.3651	100.01
Ch.6.	0.2122	4.71	2.5433	56.5
Ch.7.	0.2132	4.69	3.1213	68.66
Ch.8.	0.2274	4.40	1.6456	31.81

Table 4.3: The gain g and the readout noise σ_r measured for each channel of the HAWAII-2 FPA #77.

The transfer curves for all the three arrays had very similar characteristics. Fig. 4.2 shows the photon transfer curve for each channel of the FPA #77. The gain and the readout noise statistics derived from this curve are listed in Tab. 4.1, whereas Tabs. 4.2 and 4.3 display these values for the specimen #48 and #77. The gains of the detectors were 4-5 e^-/ADU and their values at zero gave a readout noise of 10 e^- on the average, as expected (Hodapp, 2000).

4.1.5 Feedthrough and crosstalk

Although the flicker noise is not a problem for the electric circuits driven with high frequency, unwanted signals might appear in data transfer of one part of the circuit due to the operation of another part. The feedthrough of digital signals from the clock and the control lines into the analog parts of the circuit can deform the output waveform. The feedthrough is normally the result of the varying loads due to the different signal levels and the variability in the clock edge placement due to jitter. Besides the high frequency control and clock signals the high data transfer rate also causes similar problems: the crosstalk between some analog channels can produce moderate distortion in the waveform of the video output. The noise associated with the feedthrough and crosstalk is roughly a function of square root of the clock frequency.

The pixel clock of HAWAII-2 FPA operates at 160kHz, which is high enough to produce some crosstalk events. Although bright stars can saturate the detector during its operation, resetting of the full array prevents this high excess in the pixel values from causing any residual image effects in the following image of the dithering. Nevertheless, the saturated pixels generate a crosstalk between the data transfer lines of the different channels of the quadrant in which they are situated. The data lines of the channels are organized in parallel and there might be an interference between the data lines transferring the high video signal and the neighboring ones. As a result of this crosstalk, a series of spots with the distances of 128 pixels from each other appears in the whole quadrant, corresponding to each channel. The average values of the spots were lower than the background signal and their difference was a few percent, which is large enough to degrade the photometric correctness at the places they are situated. These spots could not be measured in the raw images but they were well discernible in the reduced frames (Fig. 4.3). This effect was a general feature of the operation of all the HAWAII-2 detectors which were tested and it should be considered for the choice of pointing positions in any field of the observations.

4.1.6 Fixed Pattern Noise (FPN)

There is a noise type which does not depend on the illumination of the detector and exhibits fixed patterns instead of random properties. This type of noise, called *fix pattern moise*, is normally due to operation of the sensor circuitry. In spite of the carefully performed growing process of the sensor layer structure, there may be variations in the detector dimensions, the doping concentrations, the contamination during the fabrication and the characteristics of the MOSFETs. These non-uniformities in the physical properties of the photo-sites also cause variations in the voltage between the MOSFET components in the unit cells and in the column circuits. The output voltage can further distorted by repeating irregularities in the array clocking and, in very large arrays, resistive drops in the reset buses may lead to a fall in the reset voltage. As a result

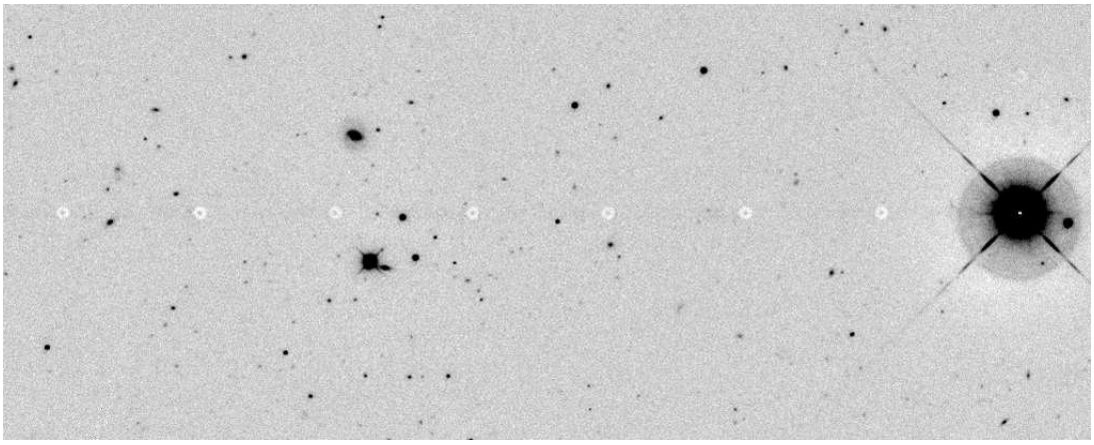

Figure 4.3: A series of pots caused by the cross talk during the transfer of the high signal values of saturated pixels.

of all these effects, a spatial variation can be measured in the output voltage produced by the pixels over the entire array even if in the absence of illumination. This spatial noise has a fixed pattern, which does not change appreciably image to image.

A typical fixed pattern noise of the HAWAII-2 FPAs is the difference of the bias levels in the 32 channels after resetting the detector, which appears in the frames taken in uncorrelated readout mode. This spatial noise besides other the noise features superimposed on the reset level can be eliminated by applying the double correlated readout mode.

4.1.7 Photo-Response Non-Uniformity and Quantum Efficiency

The non-uniformity of the pixel properties also results in a variation of their sensitivity to light. Besides the properties, such as the detector dimension, the doping concentration and the thicknesses of the over-layers, the sensitivity of the photo-sites depends on the illumination, both on its intensity and its frequency. This variation in the response of the pixels to the photo signal is called *photo-response non uniformity* (PRNU).

The image sensor technology uses some important quantities for the adequate characterization of the sensitivity of the detectors. The first one is the *responsivity* R, defined as the ratio of the electrical output signal i_s of the detector to the IR incident radiation power P,

$$R(\lambda, f) = \frac{i_s(\lambda, f)}{P(\lambda, f)} \quad , \qquad [\mathrm{AW}^{-1}] \quad , \tag{4.17}$$

where λ and f are the wavelength and the modulation frequency of the irradiaton of the imager, respectively. For unmodulated signals (f =const.), the responsivity is called *spectral response*, which describes the wavelength dependence of the response function of detectors. For a fixed wavelength of the incident radiation, i.e., when photons fall in with the same energy, the *Responsive Quantum Efficiency* η (or RQE) of the image sensors can also be introduced as the ratio of number of the detected photons to the number of the incident ones. It gives the relative efficiency in which incident photons are collected and converted into electrons or an electric output signal.

In Figs. 4.4, 4.6, and 4.6 we show the RQE of HAWAII-2 FPAs #37, #48, and #77 mea-

sured in J, H, and K bands by the Rockwell company together with the histograms of flatfield images taken with the same detectors mounted in the OMEGA2000 camera. We used dome flats which were taken with the $J_1(\lambda/\Delta\lambda$=1190/80nm), H and K filters installed in the OMEGA2000 instrument. Since the IR sources illuminating a screen for the flatfielding in dome of the 3.5 m telescope were not calibrated and we cannot measure the incident photon flux needed to derive the RQE of the image sensors. We therefore give the histrograms of the dome flats normalized with their median for a qualitative comparison between the sensitivies of the three detectors. When the histograms of the flatfield frames are compared with each other, the difference between the distribution of the sensitivity of the imagers can be established: the narrow peak of the histogram belonging to FPA #48 shows that this chip has the most uniform distribution of the sensitivity. The left wing of the histogram of FPA #37 indicates a higher non-uniformity in its upper left quadrant while the broad, less pronounced bump in the histogram of FPA #77 is caused by a global variation of the quantum efficiency in the whole array.

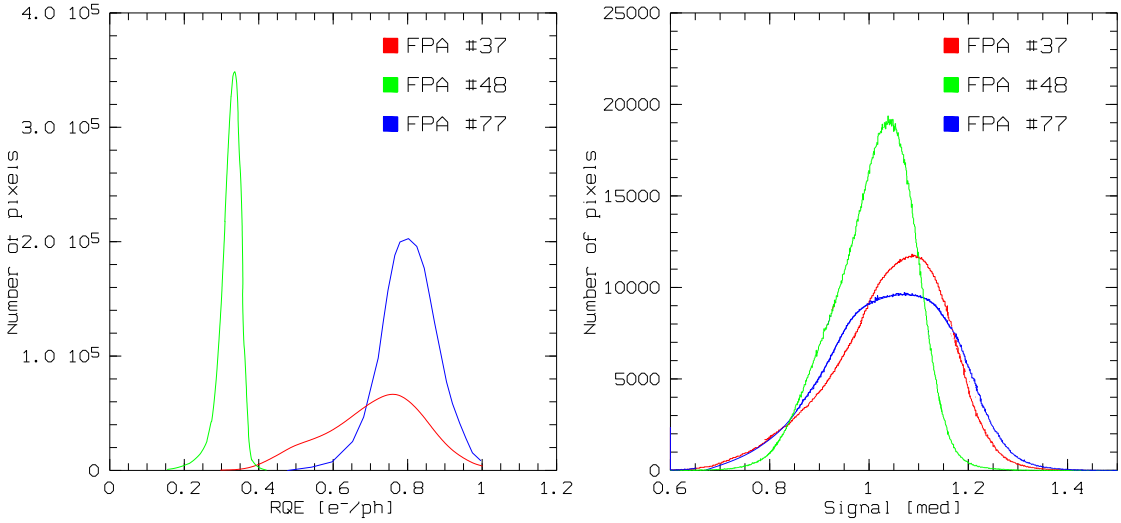

Figure 4.4: The left hand panel shows the Responsive Quantum Efficincy (REQ) of the HAWAII-2 FPAs, #37, #48, and #77 measured in J band by the Rockwell company. Theright hand panel displays the histograms of the flatfield images taken in J_1 band with with the same detectors installed in the OMEGA2000 camera.

By comparing the histograms of the normalized flatfield images with those of the RQE for each detector in each NIR band, we see the characteristics of RQE measured by the Rockwell company are similar to the distributions of the pixel values in the dome flats. The RQE histograms exhibit similar shapes and broadenings to those of the measured intensities in normalized flatfield images. In Fig. 4.7 we illustrate the different distributions of the pixel values by presenting the the flat field images for each detector.

However, neither the responsivity nor the RQE gives any information about the noise properties of image sensors, hence they cannot indicate their sensitivity. We need a quantity which can characterize not only the sensitivity of the detectors but also describe the noise degrading the quality of the measured signal. In an ideal imager the noise of the input signal, i.e., the photon shot noise σ_{ph} of the incident radiation is the only one noise source. The S/N of the

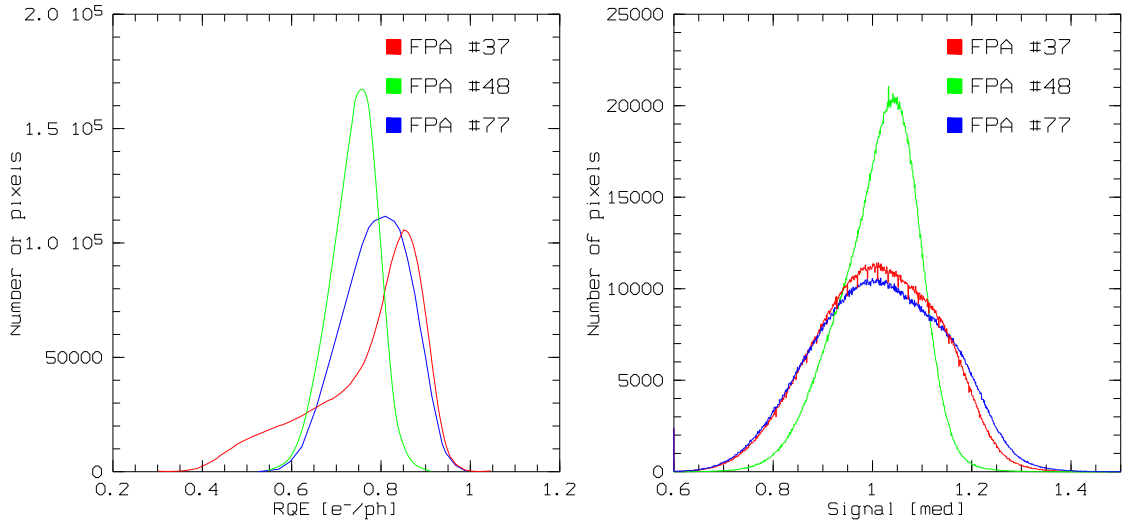

Figure 4.5: The left hand panel shows the Responsive Quantum Efficiency (RQE) of the HAWAII-2 FPAs, #37, #48, and #77 measured in H band by the Rockwell company. The right hand panel displays the histograms of the flatfield images taken in H band with the same detectors installed in the OMEGA2000 camera. .

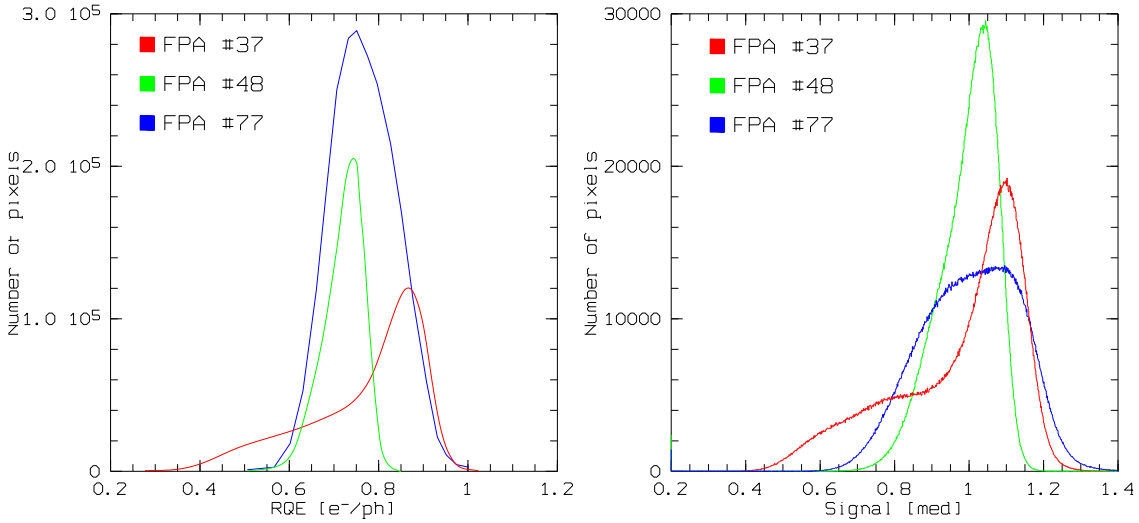

Figure 4.6: The left hand panel shows the Responsive Quantum Efficiency (RQE) of the HAWAII-2 FPAs, #37, #48, and #77 measured in K band by the Rockwell company. The right hand panel displays the histograms of the flatfield images in K band with the same detectors installed in the OMEGA2000 camera.

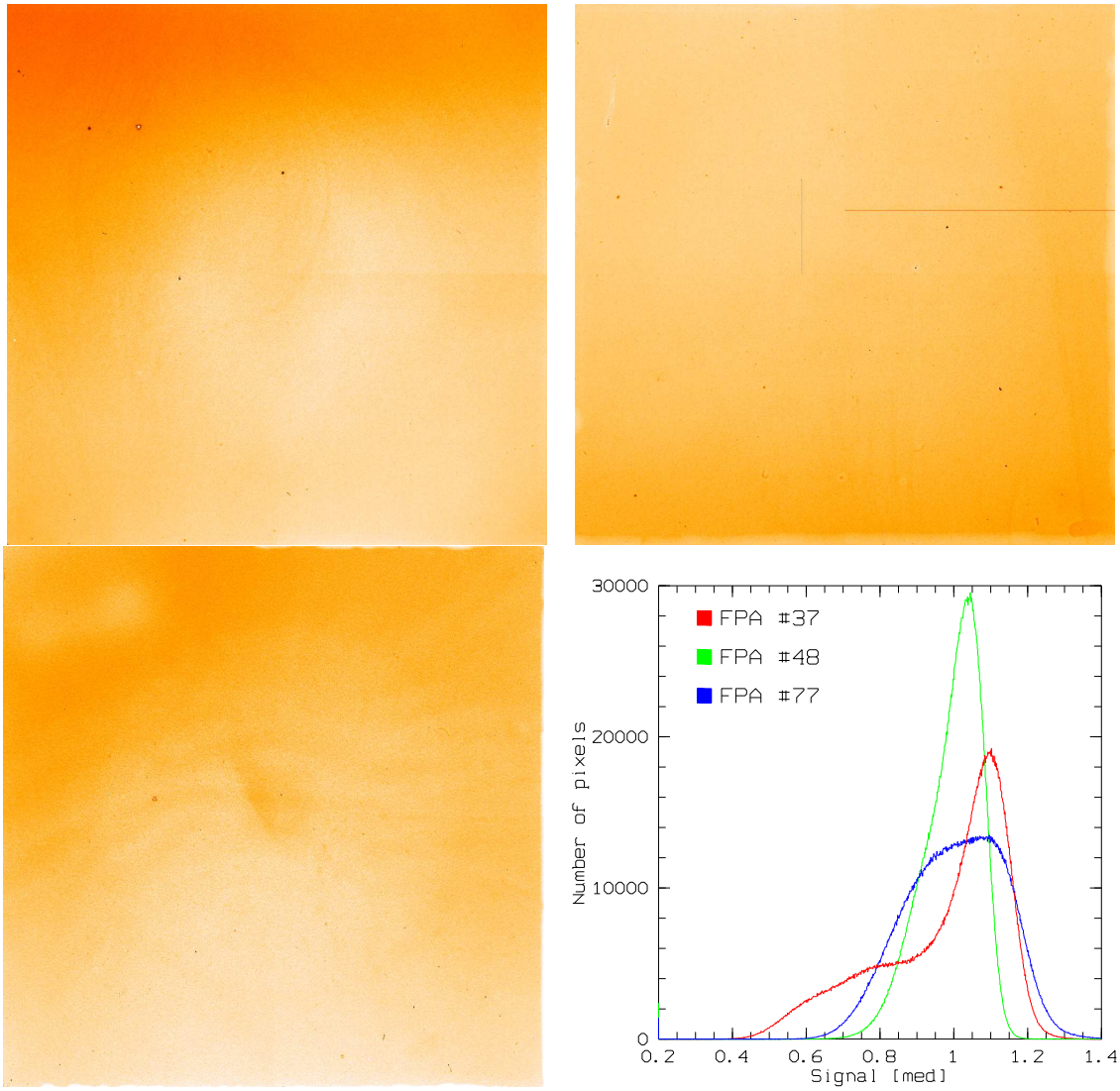

Figure 4.7: Flatfield images of FPA #37 (upper-left), #48 (upper-right) #77 (lower-left) taken with K filter and their histograms (lower-right)

ideal detector, by virtue of the Eq. (4.2), is given by

$$S/N_{ph} := s/\sigma_{ph} = n/\sqrt{n} = \sqrt{n} \tag{4.18}$$

where n is the number of the incident photons. A real image sensor has other noise sources, such as the dark current, reset, and readout noise, all of which decrease the theoretical S/N. The *Detective Quantum Efficiency* (DQE) of a real detector is defined as the square of the ratio of two S/Ns, the S/N of the output singal S/N_{out}, and that of the input radiation S/N_{in},

$$DQE := \left(\frac{S/N_{out}}{S/N_{in}}\right)^2 = \left(\frac{S/N}{S/N_{ph}}\right)^2 \tag{4.19}$$

which measures the effectivity of a real image sensor relative to that of idealized, noiseless photon-detecting system. If a calibrated IR source is used to adjust the incident flux, then the photon shot noise S/N_{ph} is also given and the average DQE can be calculated by measuring the S/N of the output signal.

Since the European Space Observatory (ESO) is determined the wavelength dependency of the RQE of the HAWAII-2 family. The quantum efficiency in the measurements was obtained by varying the temperature of a blackbody and measuring the photon response of the detector for different levels of photon flux. The filter transmission curves used to derive the photon fluxes were also measured at 77 K, the operational tempererature of a HAWAII-2 detector. For the known photon flux with Poissonian noise statistics, S/N_{ph} could be derived. The photon transfer curves of HAWAII-2 imagers were also determined, which provided their readout noise floors and gains. The gains were used to convert the detector singal to electrons. The ratio of the measured singal to the readout noise provided the S/N of the output. In Fig. 4.8, the average RQE of each FPA was measured in J, H and K broad bands and more detailed wavelength dependence of the RQE measured by ESO, which are consistent with the histograms

The average RQE given here is only an integrated value of the RQE distribution over the whole HAWAII-2 arrays. In order to obtain a more detailed characterization of quantum efficiency over the full pixel arrays, DQE maps have to be created for the NIR broad bands. Perhaps the most effective technique for mapping the DQE is to apply celestial signal sources. The OMEGA2000 camera needs only to scan a specified field containing many calibrated sources in a fine grid of pointings, i.e., with small offsets for each NIR filter, and the variation of these sources over the series of frames taken with different pointings can be used to create a high resolution DQE map over the whole detector area in each band. Since a detailed DQE map needs to have a great number of frames, the observations for this purpose demand a large amount of telescope time in nights when the weather allows for photometric observations.

4.2 Dark current

Dark current in image sensors is the result of imperfections and impurities occurring in the bulk material or at the Si-SiO_2 interface of the detector. These defects produce energy levels in the forbidden gap of the semiconductor which can be filled by thermally excited valence electrons. From this intermediate state the electrons with enough thermal energy jump to the

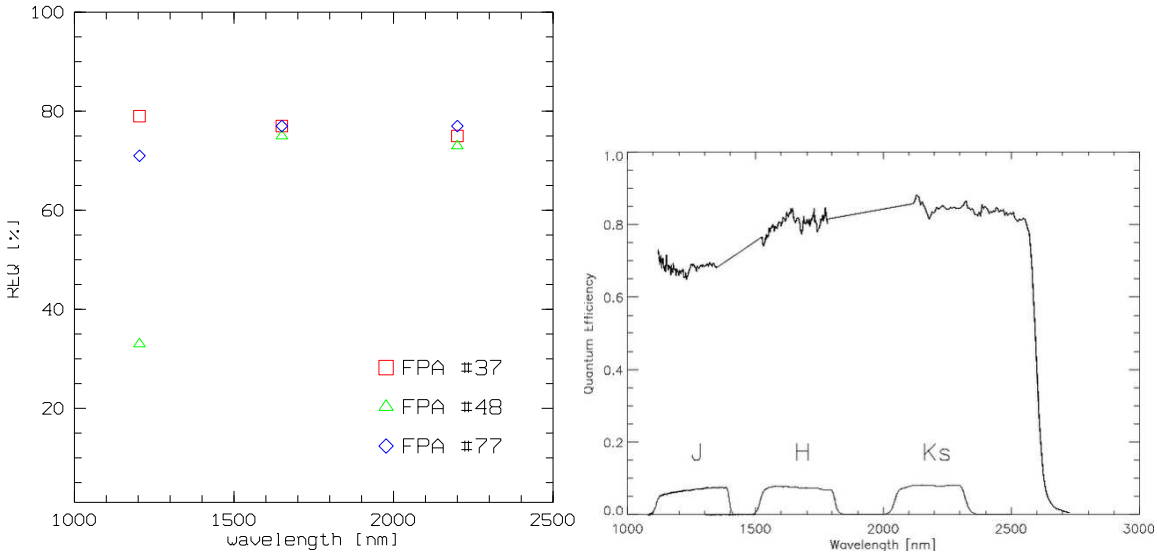

Figure 4.8: The left hand panel shows the average RQE in J, H, and K bands for the HAWAII-2 FPAs #37, #48, and #77 measured by Rockwell. The right hand panel displays the RQE vs. wavelength plot of a HAWAII-2 imager reported by ESO (Finger, 2002).

conductive band and produce a measurable signal in the well of the unit cells even in absence of illumination. The dark current due to the thermal excitation of the electrons located in the valence band strongly depends on the temperature of the detector,

$$I_{dark} = \text{const} \cdot A \cdot I_{300K} \cdot T^{1.5} \cdot e^{-\frac{Eg(T)}{2kT}} \quad , \qquad [e^-/\text{pixel} \cdot \text{s}] \quad , \tag{4.20}$$

where A is the pixel area in cm^2, I_{300K} the reference dark current measured at 300K (nA/cm^2), and E_g is the band gap energy at temperature T. The band gap energy can also be expressed in terms of the cut-off frequency λ_c of the detector material

$$E_g = \frac{hc}{\lambda_c} \quad , \qquad \text{or} \qquad E_g(eV) = \frac{1.24}{\lambda_c(\mu m)} \quad . \tag{4.21}$$

There is an empirical expression for the energy band gap of $Hg_{1-x}Cd_xTe$ as a fit function of temperature and the mol fraction x,

$$E_g(eV) = -0.302 + 1.93x + 5.35 \cdot 10^{-4}T(1-2x) - 0.81x^2 + 0.832x^3 \quad , \tag{4.22}$$

which is valid over the full composition range and for temperatures from 4.2 to 300K (Hansen et al. 1982). Therefore, the band-gap energy and in turn the cut-off wavelength can be adjusted by controlling the mol fraction of Hg and Cd, as mentioned in the previous chapter. For the HAWAII-2 chip the cut-off wavelength λ_c is 2.5 μm, which needs a band-gap energy of 0.496 eV. According to the empirical formula, the mol fraction $x = 0.458$ provides the required energy band gap at 77 K, the operational temperature of HAWAII-2. At $\lambda_c = 2.5\,\mu$m the energy gap of the HgTeCd semiconductor does not exhibit strong temperature dependence, hence E_g can be considered at constant band-gap wavelength (Hodapp et al. 1995). At lower temperatures and longer cut-off wavelengths the tunneling currents between defect states and the HgTeCd valence and conduction

bands increase with decreasing temperature according to the temperature dependence of the HgTeCd band-gap. The tunneling current has, in fact, relatively weak temperature dependence but it depends on bias voltage strongly. Nevertheless, the cut-off wavelength of HAWAII-2 is relatively short and any changing in the bias voltage does not really effect the contribution of tunneling current to total amount of dark current.

In this section we discuss both the temporal and spatial noise associated with dark current. The dark current shot noise, as a random and temporal noise, is negligible for the HAWAII-2 FPA and will be considered briefly. Then we characterize the dark current non-uniformity for the three HAWAII-2 chips. We present the measurements of the dark current statistics for each FPA and explain how to eliminate the contribution of dark current in the frames.

4.2.1 Dark current shot noise

Shot noise arises not only from the photon statistics but also from the presence of thermal electrons within the depletion region. The dark current shot noise also has Poisson statistics, so its amount can be expressed as

$$\sigma_{dark} = \sqrt{n_{dark}} \ , \tag{4.23}$$

where n_{dark} is the integrated dark current over a give time and measured in electrons. It is a temporal noise and averaging of more frames can reduce this effect. As will be seen in this section, the mean dark current of each specimen of HAWAII-2 FPA is about 0.03-0.04 e^-/s which gives σ_{dark}=0.17-0.20 e^-/s. These values are less then one ADU and much smaller than the net current from other noise sources, therefore the shot noise arisen from the statistical fluctuation in the dark current is negligible for integration times on the order of 10 s..

4.2.2 Dark current non-uniformity

On account of the variation in the physical properties of the unit cells, the same thermal energy excites valence electrons in the semi-conductor layer, producing varying amounts of dark current in each pixel. This dark current non-uniformity, due to the global variation of the physical properties of the individual unit cells, has a fixed spatial variation. In other words, the fixed pattern noise is the same in all the frames and can be eliminated by subtracting a dark reference frame from the illuminated image if both of them are taken with same exposure time and at the same temperature. Of course, this method has as an expense that subtraction of two images increases the dark current shot noise by factor of $\sqrt{2}$ and the readout noise.

The left hand panel of Fig. 4.9 shows the dark current histograms for HAWAII-2 FPAs #37, #48, and #77, measured by the Rockwell company. We also present the statistical momenta of the dark current characteristics of these detectors in Tab. 4.4. The dark current of these detectors is reported to be only about 0.02 e^-/s at 77 K (Hodapp et al., 1995) and the median values of the dark current provided by Rockwell for these specimen are in the interval 0.03-0.04 e^-/s, i.e., they are a factor of 1.5-2 larger than the specified value. However, these detectors still have negligible dark currrent contribution for integration times of 1-5 sec, which are in the range of the typical exposure times for scientific imaging. We also determined the dark current statistics for these HAWAII-2 chips under the control of the readout electronics of OMEGA2000. We took

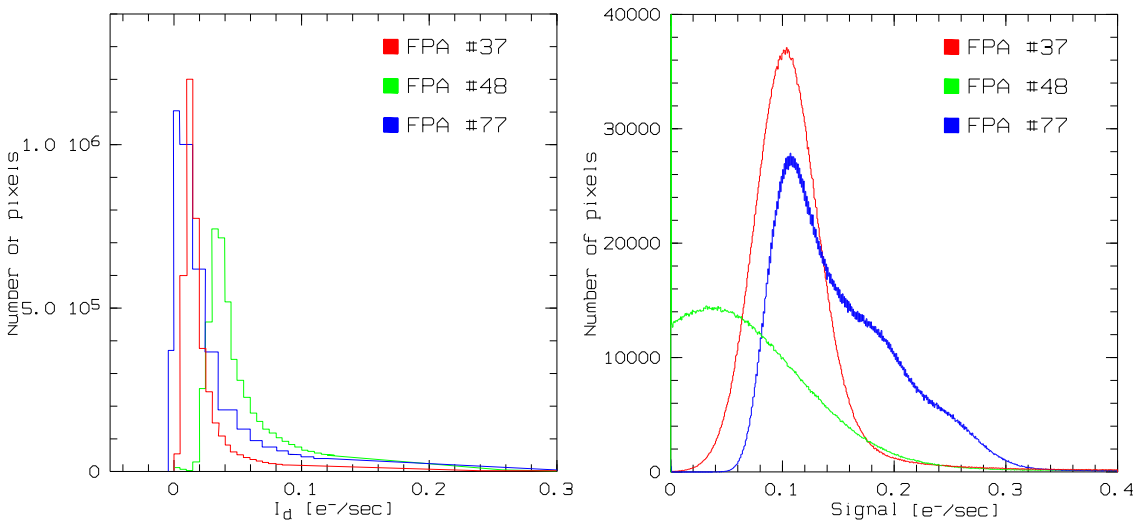

Figure 4.9: The left hand panel shows the dark current characteristics of the HAWAII-2 FPA #37, #48, and #77, measured by the Rockwell company. The right hand panel shows the histograms of dark frames taken with the detectors #37, #48, and #77 installed in the OMEGA2000 camera.

FPA No.	Min. value (e^-/sec)	Max. value (e^-/sec)	Mean value (e^-/sec)	Median value (e^-/sec)	Std. dev. (e^-/sec)
#37	0.000	1.000	0.035	-	0.065
#48	0.000	1.000	0.059	0.043	0.065
#77	-0.50	1.000	0.050	0.032	0.075

Table 4.4: Dark current statistics of the HAWAII-2 FPAs #37, #48, and #77 measured by the Rockwell company.

FPA No.	Min. value (e^-/s)	Max. value (e^-/s)	Mean value (e^-/s)	Median value (e^-/s)	Std. dev. (e^-/s)
#37	-1.11	1.09	0.163	0.15	0.21
#48	0.000	3.35	0.069	0.212	0.075
#77	-4.71	1.22	0.191	0.087	0.09

Table 4.5: Dark current statistics of the HAWAII-2 FPAs #37, #48, and #77 measured by MPIA.

dark frames for each HAWAII-2 imager with different integration times from the minimal frame readout times up to 2000 s by using a blank disk inserted in the filter wheel. As an example, Fig. 4.10 shows a dark frame of the FPA #48, which demonstrates the high uniformity of the dark current generated in the HAWAII-2 detector family. In the color coded figure, the areas with lowest measured counts are represented with dark blue color, while the lighter colors indicate the highest pixel values. The most prominent features are the glowing output transistors of each channel at the borders of the of the pixel array and the group of hot pixels with a dead core in the upper left quadrant. Aside from these artifacts, the dark current has a rather uniform characteristic over the whole array. The histograms of the dark frames, shown in the left hand panel in Fig. 4.9, have different characteristics from the ones specified by the Rockwell company. This is demonstrated with the statistical momenta of the distribution of the measured signal as well, which we present in Tab. 4.5. The median values we measured for the three detectors were one order of magnitude higher than the specified values and the distribution of the dark current histograms are broader than those measured by the Rockwell company. With the median value of dark current of 0.03-0.04 e^-/s for these detectors, the median of the dark signal with the integration time of 2000 s is expected to be 60-80 e^-. However, the median values in the dark frame histograms of each FPA were normally measured to 200 e^- for the integration time of 2000 s. This means the the dark signal of the image sensor was completely dominated by other noise sources (Fig. 4.9). Besides the non-uniformities of dark current, the individual channels building up the quadrant structure were also well discernible due to slightly different offset voltages in amplifier circuits. Other typical noise features were the periodic noise patterns over all the frame caused by a coupling between the pre-amplifiers and the power supply and the glowing of the output transistors. The glowing gave only a small excess on the right wing of dark frame histograms and did not change their mean values, which were determined by the noise of the external amplifiers. In fact, it is possible to eliminate their thermal radiation by switching the output transistors of the HAWAII-2 off during the integration time but a more stable operation of the chip can be ensured without switching the transistors off and on in each readout cycle. The glowing for exposure times of some minutes is small and it can easily be subtracted from the video signal.

There are two basic methods for the subtraction of the dark frame from the raw images. If the exposure time is fixed, it is enough to take a series of dark frames with the same integration time as the scientific frames, average them to reduce the dark current shot noise and the result can be subtracted from the image frames. For raw frames taken with different exposure times, it may be more convenient to produce a *thermal frame* from a stack of dark frames with different

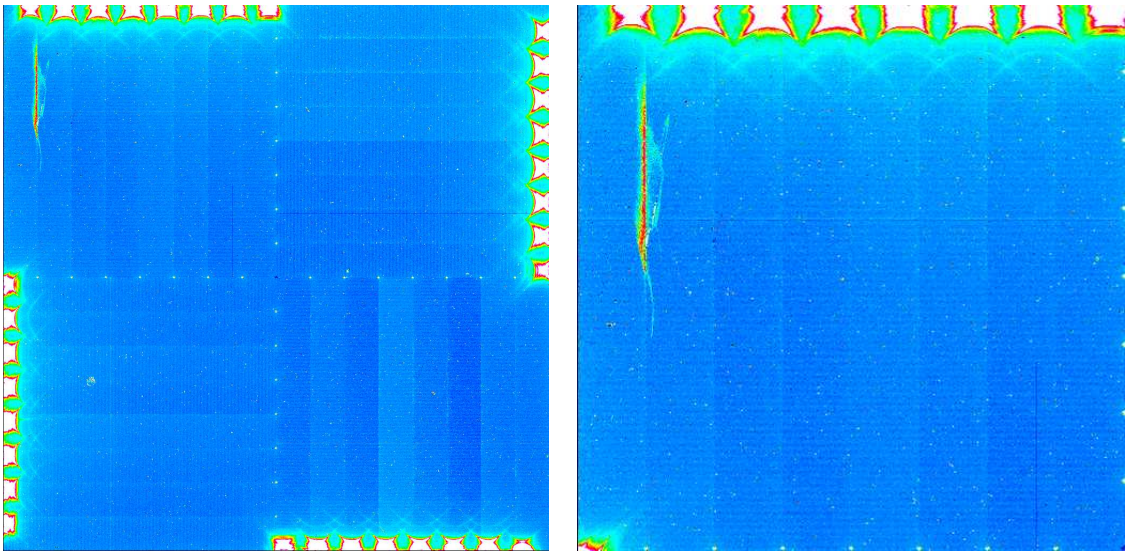

Figure 4.10: A dark frame of the FPA #48 taken with an integration time of 320 s. The left hand panel shows the whole array whereas the right hand one displays the upper left quadrant. The glowing of the eight output transistors can be seen in all the quadrants.

integration times. Since the signal measured in healthy pixels is proportional to the integration time, we can make a linear fit on the series of pixel values of each good pixel in the stack of frames. Then we can produce a map by taking the slope of the linear fit for each pixel. This map is the *thermal frame* of the image sensor, which contains the distribution of its dark current in ADU/(pixel · s).

The linear fit fails for those pixels which exhibit a highly non-linear response to the illuniation. The signal of these pixels will have a large scatter around the linear fit and they can be clipped out from the thermal frame by defining a threshold of the scatter, as we will discuss in the next section. The more dark frames we use for fitting, the more efficiently the dark current shot noise is suppressed in this map as in the case of the averaging dark frames. Then the thermal frame can be scaled according to the different exposure times of the raw images and subtracted from them. For the data reduction in the scientific applications thermal frames were used, which will be described in the next chapter.

4.3 Bad and hot pixels

In scientific-grade imagers the dark current is low and more or less uniform but some photo-sites, called *hot pixels*, always produce a dark current of some orders of magnitude higher than the average value. They are represented by the wider right wing of the dark current histogram in Fig. 4.9. Although the rate of accumulation of the thermal electrons in these photo-sites is much higher than the one of other pixels, it is constant in time. This means the hot pixels have also a linear response, which allows us to subtract the dark level from the photo signal as in the case of the normal pixels. Nevertheless, every image sensor contains a few photo-sites which have a highly non-linear response. They are considered to be *dead* or *bad pixels* because their non-linear behavior prevents us from subtracting the dark level correctly from the photo signal. Hot pixels

scatter in the array of the photo-sites individually or form groups but individual bad pixels are very rare and they compose particularly the cores of hot pixel groups. Sometimes a complete column or line of a quadrant is also dead. These features appear in a typical bias subtracted dark frame of a HAWAII-2 chip taken with long integration time at 77K. The upper left quadrant in Fig. 4.10, there is a large group of hot pixels with dead cores and all the quadrants contain some bad columns and lines.

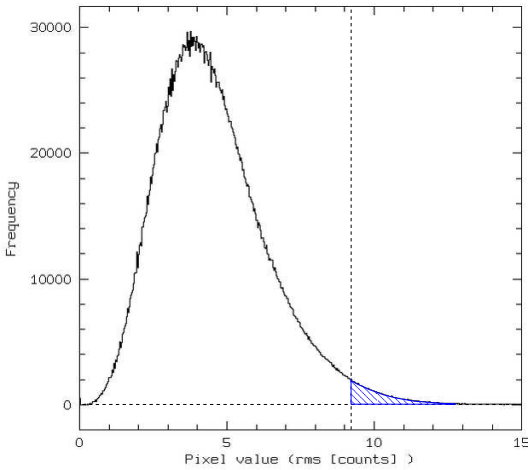

Figure 4.11: The histogram of RMS map calculated form the the fitting of a stack of dark frames taken different integration times for the HAWAII-2 FPA #48. The vertical dashed line denotes the upper limit of the RMS value above which the pixels are defined to be bad pixels. The latter are represented by the blue shaded area of histogram.

Besides the dark current subtraction, the thermal frames of the detectors also served to separate bad pixels from healthy ones. For each pixel in a stack of dark frames taken with different integration times, a root mean square map of the deviation from the values in the scaled thermal frames can be computed. Since a thermal frame is the result of a linear fitting, an RMS map contains the scattering of the signal values around the scaled fit. Its histogram at high values represents the pixels for which the linear fitting failed because of their highly non-linear response, so the map helps to discriminate the bad pixels from the hot and the normal ones. The histogram of the RMS map contains a well pronounced peak of the healthy pixels (Fig. 4.11). The wing of the peak at the right hand side is less steep because the major part of it represents the hot pixels. By defining an upper and lower limit in the histogram so that the chosen interval contains the peak and the wing representing the hot pixels, the pixels which have RMS values out of this interval can be considered as bad ones. The bad pixel masks created by using this method contained about 1000, 3600 and 5000 bad pixels for FPA #37, #48 and #77, respectively. This means more than 99.8% of the pixels could be corrected by dark current subtraction and flatfielding for all the three detectors.

4.4 Linearity

Besides the map containing the slope of the linear fitting, it is also useful to create another one with the additive constant of the fitting and third one with the root mean square describing the

scattering of the pixel values around the fit line. These maps together characterize the linearity of response of the photo-sites satisfactorily and provide a simple method to separate the bad pixels from the healthy ones. The histograms of the slope and the constant maps have a peak representing the great number of well-behaving pixels. Its tails at the left and right hand side consist of the cold, hot and bad pixels. The histogram of the RMS map also has a similar shape but its tail at high values contains only the pixels with very non-linear responses. Therefore this map can be used to estimate the number of pixels which still have a linear response. However, the saturation of the unit cells at high gives a limit, which determines the linear dynamical range of image sensors.

The linearity of the HAWAII-2 detectors is measured by taking flatfields with different integration times and constant illumination through a narrow band filter (NB1083). Since the dark current of the HAWAII-2 chips is very low and the maximal exposure time was 2000 s, the dark current contribution had a negligible effect on the measured signal. We measured the non linearity of the signal with increasing exposure time, i.e., the deviation of the signal value from the linearly scaled values with time. All of the detectors #37, #48 and #77 were linear within 1% of the signal up to about 40000 ADU, which means the linear full well capacity of each FPA is $\sim 200000\ e^-$ (Fig. 4.12).

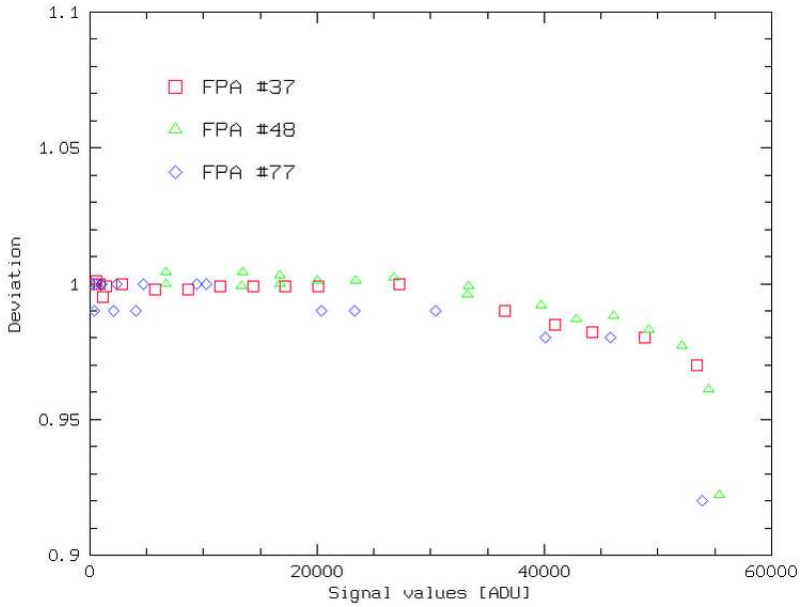

Figure 4.12: Linearity tests for the three HAWAII-2 FPAs.

List of Figures

1.1 The OMEGA2000 NIR camera mounted on front ring (In Röser, 2004). 13
1.2 The OMEGA2000 cryosat mounted on front ring (In Baumeister et al., 2002). . . 14
1.3 Four lens reducer with spring loaded cryogenic lens mount (In Baumeister et al., 2002). 15
1.4 The left hand panel shows the center to corner image distortion of the OMEGA2000 optics (In Röser, 2004) and the right hand panel is a flatfield frame with the ghost image of the primary mirror. 16
1.5 The warm baffles of OMEGA2000 (In Baumeister et al., 2002) and the working principle of the movable warm baffle (In Röser, 2004). 17
1.6 The filter wheel with its spring mechanism for positioning and cooling (a), mechanism locked (b) and unlocked (c) (In Baumeister et al. 2002). 17
1.7 The detector unit with the base plate, fanout board, detector and its cooling mechanism (In Baumeister et al., 2002). 18
1.8 The block diagram of the read-out electronics of OMEGA2000 (In Röser, 2004). . 19
1.9 The conversion range between the analog output of HAWAII-2 detector, 3.5-4.5 V, and digitized data, 0-65535 ADU. 20
1.10 The scheme of the control interface of GEIRS. The two main control panels of GEIRS are shown in the left hand side. The files containing the macros, instruction tables, files for initialization, and variables for the readout electronics are represented with yellow boxes. whereas the blue arrows indicate their dependencies on each other. 21

2.1 HAWAII-2 FPA mounted on its fanout board (Photo: Peter Bizenberger). 24
2.2 Low noise APS Circuits for hybrid and monolithic FPAs. SF detectors (a), CTI Amplifiers (b) and the solution of MOSFET Gate Modulation (c) (In Hodapp, 2000). 25
2.3 The cross-sectional view of HAWAII-2 (in Kozlowski et al., 1998). 26
2.4 The quadrant and channel layout of HAWAII-2 (In Haas, 2002). 27
2.5 HAWAII-2 internal architecture (In Haas, 2002). 28
2.6 Timing diagrams for the readout of the first and second rows of HAWAII-2 FPA quadrant (In Haas, 2002). 31
2.7 Timing diagram for the readout of the last and first rows of HAWAII-2 FPA quadrant (In Haas, 2002). 32

2.8 The timing diagrams of the signal (upper) and the control pattern (lower) for the reset level read (reset-read). 33

2.9 The timing diagrams of the signal and the control pattern for non-correlated sampling (reset-read). 34

2.10 The timing diagrams of the signal and the control pattern for CDS (reset-read-read). 34

2.11 The timing diagrams of the signal and the control pattern for CDS with fast reset (reset-read-read). 35

2.12 The timing diagrams of the signal and the control pattern for the line-interlaced read. 36

2.13 The timing diagrams of the signal and the control pattern for the multiple endpoint read. 36

3.1 The left hand panel displays the normal triggering of the video signal conversion of the first pixel in the FPA and the right hand one the triggering with delay. The clock signal (CLK1) is plotted with green color, the output singal of the video amplifier with yellow, the start signal of the sampling (SCON) with purple, and the frame synchronization signal (FSYNC) with magenta. 43

3.2 The left hand panel shows the drift in the video signal after reset and the right hand one displays it after integration. The clock signal (CLK1) is plotted with green color, the output singal of the video amplifier with yellow, and the frame synchronization signal (FSYNC) with magenta. 46

3.3 The left hand panel shows a frame taken with the FPA #37 with higher incident flux, 20,000 ADU on the average, and the right hand one displays a frame taken with the weakly irradiated detector, producing only $\sim$ 5000 ADU. The latter exhibits drifts at the outer edges of the quadrants. 46

3.4 The deviation of the value of last pixel from those of the previous pixels in an arbitrary row of the array. The the line synchronization signal LSYNC is plotted with green color, the output singal of the video amplifier with yellow. 47

3.5 Dark frames produced by the FPA #37. The left hand panel shows a image taken with fast reset and the right side one displays an image taken in conservative CDS mode. 48

3.6 The two upper panel display the right lower quadrants of the dark frames taken in CDS mode with fast reset (left hand panel) and in conservative CDS mode (right hand panel) with FPA #48. The lower panels give cross sectional views of the summed signal values over the whole arrays for the same frames. 49

4.1 The definition of the noise equivalent bandwidth. The shaded areas are equal. . 53

4.2 The photon transfer curve for each quadrant of the FPA #37. 56

4.3 A series of pots caused by the cross talk during the transfer of the high signal values of saturated pixels. 61

4.4 The left hand panel shows the Responsive Quantum Efficincy (REQ) of the HAWAII-2 FPAs, #37, #48, and #77 measured in J band by the Rockwell company. Theright hand panel displays the histograms of the flatfield images taken in J_1 band with with the same detectors installed in the OMEGA2000 camera. 62

4.5 The left hand panel shows the Responsive Quantum Efficiency (RQE) of the HAWAII-2 FPAs, #37, #48, and #77 measured in H band by the Rockwell company. The right hand panel displays the histograms of the flatfield images taken in H band with the same detectors installed in the OMEGA2000 camera. . 63

4.6 The left hand panel shows the Responsive Quantum Efficiency (RQE) of the HAWAII-2 FPAs, #37, #48, and #77 measured in K band by the Rockwell company. The right hand panel displays the histograms of the flatfield images in K band with the same detectors installed in the OMEGA2000 camera. 63

4.7 Flatfield images of FPA #37 (upper-left), #48 (upper-right) #77 (lower-left) taken with K filter and their histograms (lower-right) 64

4.8 The left hand panel shows the average RQE in J, H, and K bands for the HAWAII-2 FPAs #37, #48, and #77 measured by Rockwell. The right hand panel displays the RQE vs. wavelength plot of a HAWAII-2 imager reported by ESO (Finger, 2002). 66

4.9 The left hand panel shows the dark current characteristics of the HAWAII-2 FPA #37, #48, and #77, measured by the Rockwell company. The right hand panel shows the histograms of dark frames taken with the detectors #37, #48, and #77 installed in the OMEGA2000 camera. 68

4.10 A dark frame of the FPA #48 taken with an integration time of 320 s. The left hand panel shows the whole array whereas the right hand one displays the upper left quadrant. The glowing of the eight output transistors can be seen in all the quadrants. 70

4.11 The histogram of RMS map calculated form the the fitting of a stack of dark frames taken different integration times for the HAWAII-2 FPA #48. The vertical dashed line denotes the upper limit of the RMS value above which the pixels are defined to be bad pixels. The latter are represented by the blue shaded area of histogram. 71

4.12 Linearity tests for the three HAWAII-2 FPAs. 72

5.1 COMBO-17 filter set: Total system efficiencies are shown in the COMBO-17 passbands, including two telecope mirrors, WFI instrument, CCD detector and average La Silla atmosphere. Combining all observations provides a low-resolution spectrum for all objects in the field (In Wolf et al. 2003). 77

5.2 The NIR filter set of COMBO-17+4 NIR: Total system efficiencies are shown in the NIR passbands, including the telecope mirror, OMEGA2000 instrument, CCD detector, and average Calar Alto atmosphere. 83

5.3 The COMBO S11 field (deep R-band image form the COMBO-17 survey) covered by the four OMEGA2000 pointings A, B, C and D. 85

List of Tables

2.1 Nominal Bias Voltages for the HAWAII-2 (In Haas, 2002). 29
2.2 Output Mode Control Signals for HAWAII-2 (In Haas, 2002). 30

3.1 The minimal redout times of the implemented readout modes of HAWAII-2 FPA. * For the single pixel read this value depends on the position of the pixel to read out. Here, we read out the 10.-th pixel located in the 6.-th line of each quadrant. 44
3.2 Observations with two specimen of the HAWAII-2 FPA in the OMEGA2000 camera. 48

4.1 The gain g and the readout noise σ_r measured for each channel of the HAWAII-2 FPA #37. 57
4.2 The gain g and the readout noise σ_r measured for each channel of the HAWAII-2 FPA #48. 58
4.3 The gain g and the readout noise σ_r measured for each channel of the HAWAII-2 FPA #77. 59
4.4 Dark current statistics of the HAWAII-2 FPAs #37, #48, and #77 measured by the Rockwell company. 68
4.5 Dark current statistics of the HAWAII-2 FPAs #37, #48, and #77 measured by MPIA. 69

5.1 Positions and galactic reddening for the three COMBO-17 fields. Fields shown in bold face are already completed in optical regime. 76
5.2 Positions and galactic reddening for the three COMBO-17+4 NIR survey areas. 84
5.3 NIR-band observations in the A 226 and the S 11 fields with 3.5m telescope equipped with the OMEGA2000 camera carried out for COMBO-17+4 NIR survey between September 2003 and April 2004. We used the NIR-band data which were provided by the observations shown in bold face letters. 86

6.1 Co-moving number densities and their Poissonian confidence intervals of 95% for galaxies brighter than $M_B = -20 + 5 \log h$ in the in the COMBO S11 sample with $R < 25.8$ and $H < 21.4$. 124
6.2 The differential number counts and the cumulative surface density for EROs as a function of H magnitude over 0.2 deg^2 of the COMBO S11 field. The quoted errors are Poisson with 95% confidence interval. 134

Acronyms

ADU	-	Analog-Digital Unit
APS	-	Active Pixel Sensor
CDM	-	Cold Dark Matter
CDS	-	Correlated Double Sampling
CITA	-	Capacitive TransImpendance Amplifier
ERO	-	Extremely Red Object
FPA	-	Focal Plane Array
NIR	-	Near Infra-Red
PLE	-	Passive Luminosity Evolution
PPS	-	Passive Pixel Sensor
SED	-	Spectral Energy Distribution
SFD	-	Source Follower Detector
SSP	-	Simple Star Population

Bibliography

[Bailer et al., 2000] C. A. Bailer-Jones, P. Bizenberger, and C. Storz, "Achieving a wide field infrared camera for the Calar Alto 3.5m telescope," in *Optical and IR Telescope Instrumentation and Detectors*, M. Iye and A. F. Moorwood, eds., *Proc. SPIE* **4008**, pp. 1305–1316, 2000.

[Baumeister et al., 2002] H. Baumeister, P. Bizenberger, C.A. Bailer-Jones, Z. Kovács, H.-J. Röser, and R.-R. Rohloff, "Cryogenic engineering for Omega 2000: Desig and performance," in *Instrument Design and Performance for Optical/Infrared Ground-based Telescopes*, *Proc. SPIE* **4842**, pp. 343–354, 2002.

[Bell et al. 2003] E.F. Bell, D.H. McIntosh, N. Katz, and M.D. Weinberg: 2003. The Optical and Near-Infrared Properties of Galaxies. I. Luminosity and Stellar Mass Functions *Astrophysical Journal Suppl.* **149**, 289+

[Bell et al. 2004] E.F. Bell, C. Wolf, K. Meisenheimer, H.-W. Rix, A. Borch, S. Dye, M. Kleinheinrich, L. Wisotzki, and D.H. McIntosh: 2004. Nearly 5000 Distant Early-Type Galaxies in COMBO-17: A Red Sequence and Its Evolution since $z \sim 1$ *Astrophysical Journal* **608**, 752+

[Bergström and Wiklind] S. Bergström, and T. Wiklind: 2004. On the colour-colour properties of the Extremely Red Objects. *Astronomy and Astrophysics* **414**, 95B+

[Bruzual, 1983] A.G. Bruzual: 1983. Spectral evolution of galaxies. I - Early-type systems *Astrophysical Journal* **273**, 105+

[Carlberg et al., 2000] R.G. Carlberg, J.G: Cohen, D.R. Patton, R. Blandford, D.W. Hogg, H.K.C. Yee, S.L. Morris, H. Lin, P.B. Hall, M. Sawicki, and 4 coauthors: 2000. Caltech Faint Galaxy Redshift Survey. XI. The Merger Rate to Redshift 1 from Kinematic Pairs *Astrophysical Journal* **521**, L1+

[Chen et al., 2003] H.-W. Chen, R.O. Marzke, O. Ronald, P.J. McCarthy, Patrick. P. Martini, R.G. Carlberg, S.E. Persson, A. Bunker, C.R. Bridge, and R.G. Abraham: 2003. The Las Campanas Infrared Survey. IV. The Photometric Redshift Survey and the Rest-frame R-band Galaxy Luminosity Function at $0.5 \leq z \leq 1.5$ *Astrophysical Journal* **586**, 745-764

[Cimatti et al., 1999] A. Cimatti, E. Daddi,S. di Serego Alighieri, L. Pozzetti, F. Mannucci, A. Renzini, E. Oliva, G. Zamorani, P. Andreani, and H.J.A. Röttgering: 1999. New clues on the nature of extremely red galaxies. *Astronomy and Astrophysics*, **352**, 45+.

[Cimatti et al., 2002] A. Cimatti, L. Pozzetti, M. Mignoli, E. Daddi, N. Menci, F. Poli, A. Fontana, A. Renzini, G. Zamorani, T. Broadhurst, S. Cristiani, S. D'Odorico, E. Giallongo and R. Gilmozzi: 2002, The K20 survey IV. The redshift distribution of galaxies: A test of galaxy formation models. *Astronomy and Astrophysics* **391**, L1-L5

[Conselice, Blackburne, and Papovich, 2005] C. J. Conselice, J. A. Blackburne, and C. Papovich: 2005. The luminosity, stellar mass, and number density evolution of field galaxeis of known morphology from $z = 0.5 - 3$. *Astrophysical Journal* **620**, 564-583

[Cowie et al., 1996] L.L. Cowie, A. Songaila, E.M. Hu, and J.G. Cohen: 1996. New Insight on Galaxy Formation and Evolution From Keck Spectroscopy of the Hawaii Deep Fields *Astrophysical Journal* **112**, 839+

[Daddi et al. 2000] E. Daddi, A. Cimatti, L. Pozzetti, H. Hoekstra, H. J. A. Röttgering, A. Renzini, G. Zamorani, and F. Mannucci: 2000. Detection of Strong Clustering of Extremely Red Objects: Implications for the Density of $z > 1$ Ellipticals. *Astronomy and Astrophysics* **361**, 535+

[de Vaucouleurs et al., 1991] G. de Vaucouleurs, A. de Vaucouleurs, H.G. Corwin, Jr., R.J. Buta, G. Paturel, and P. Fouqué: 1991. Third Reference Cataloguq of Bright Galaxies, New York: Springer

[Dickinson et al., 2003] M. Dickinson, C. Papovich, H.C. Ferguson, and T. Budavári: 2003. The Evolution of the Global Stellar Mass Density at $0 < z < 3$. *Astrophysical Journal* **587**, 25+

[Doherty] M. Doherty, A.J. Bunker, R.S. Ellis, and P.J. McCarthy: 2005. The Las Campanas Infra-red Survey. V. Keck Spectroscopy of a large sample of Extremely Red Objects. astro-ph/0505119

[Drory et al., 2001] N. Drory, R. Bender, J. Snigula, G. Feulner, U. Hopp, C. Maraston, G. J. Hill, and C. Mendes de Oliveira: 2001. The Munich Near-Infrared Cluster Survey (MUNICS) - Number density evolution of massive field galaxies to $z \sim 1.2$ as derived from the K-band selected survey. *Astrophysical Journal* **562**, L111-L114

[Eggen, Lynden-Bell and Sandage, 2001] O.J. Eggen, D. Lynden-Bell, and A.R. Sandage: 1962. Evidence from the motions of old stars that the galaxy collapsed. *Astrophysical Journal* **136**, 748+

[Elston, Rieke & Rieke, 1988, 1989] R., Elston, G.H. Rieke and M.J. Rieke: 1988. Deep 2 micron imaging of the sky: evidence for a new extragalactic population. *Astrophysical Journal*, **331**, L77-L80.

[Elston, Rieke & Rieke, 1989] R, Elston, G.H. Rieke and M.J. Rieke: 1989. Observations of deep 2 micron survey galaxies: primeval galaxy candidates. *Astrophysical Journal*, **341**, 80-88.

[Finger. 2002] G. Finger: "Test Report on HgCdTe Infrared Focal Plane Arrays", Garching, European Southern Obseravtory. 2002.

[Firth et al. 2002] A. E. Firth, R. S. Somerville, R. G. McMahon, O. Lahav, R. S. Ellis, C. N. Sabbey, P. J. McCarthy, H.-W. Chen, R. O. Marzke, J. Wilson, R. G. Abraham, M. G. Beckett, R. G. Carlberg, J. R. Lewis, C. D. Mackay, D. C. Murphy, A. E. Oemler, and S. E. Persson: 2002. Las Campanas IR Survey. II. Photometric redshifts, comparison with models and clustering evolution. *Monthly Notes R. Astron. Soc.* **332**, 617+

[Fioc & Rocca-Volmerange] M. Fioc, B. Rocca-Volmerange: 1997. PEGASE: a UV to NIR spectral evolution model of galaxies - Application to the calibration of bright galaxy counts. *Astronomy and Astrophysics* **326**, 950-962

[Giallongo et al. 2005] E. Giallongo, S. Salimbeni, N. Menci, G. Zamorani, A. Fontana, M. Dickinson, S. Cristiani, L. Pozzetti: 2005. The B-Band Luminosity Function of Red and Blue Galaxies up to $z = 3.5$. *Astrophysical Journal* **622**, 116-128

[Gear et al. 2000] Authors: W. K. Gear, S.J. Lilly, J.A. Stevens, D.L. Clements, T.M. Webb, S.A. Eales, and L. Dunne: 2000. High spatial resolution observations of CUDSS14A: a SCUBA-selected Ultraluminous galaxy at high redshift. *Monthly Notes R. Astron. Soc.* **316**, L51

[Gil de Paz & Madore] A. Gil de Paz (1,2), and B. F. Madore: 2002 On the Optimization of Broad-Band Photometry for Galaxy Evolution Studies. *Astronomical Journal* **123**, 1864+

[Haas, 2002] A. Haas, "Users Guide for the HAWAII-2 2048x2048 Pixel Focal Plane Array," Rockwell Scientific Company, LLC, 2002

[Hansen et al., 1982] G.L. Hansen, J.L. Schmidt, and T.N. Casselman, Energy gap versus alloy composition and temperature in $Hg_{1-x}Cd_xTe$, *J. Appl. Phys.* **53**(10) pp. 7099-7101, 1982.

[Hodapp et al., 1995] K. Hodapp, D. H. J.L. Hora, L. Cowie, M. Metzger, E. Irwin, T. Keller, K. Vural, L. Kozlowski, and W. Kleinnhans, "Astronomical characterization results of 1024x1024 HgCdTe HAWAII detector arrays," in *Infrared Detectors and Instrumentation for Astronomy*, A. M. Fowler, ed., *Proc. SPIE* **2475**, pp. 8–14, 1995.

[Hodapp, 2000] K. Hodapp, "Near-infrared detector arrays: Current state of the art," in *Optical and IR Telescope Instrumentation and Detectors*, M. Iye and A. F. Moorwood, eds., *Proc. SPIE* **4008**, pp. 1228–1239, 2000.

[Hu & Ridgaw, 1994] E.M. , Hu, and G.H. Ridgaw: 1994. The extremely red galaxies. *Astronomical Journal* **107**, 1030+.

[Kauffmann, Charlot and White] G. Kauffmann, S. Charlot, and S.D.M. White: 1996. Detection of strong evolution in the population of early-type galaxies. *Monthly Notes R. Astron. Soc.* **283**, L117+.

[Kozlowski et al., 1998] L.J. Kozlowski, K. Vural, S.A. Cabelli, A. Chen, D.E. Cooper, C. Cabelli, K. Hodapp, D. Hall, and W.E. Kleinhans, "HgCdTe 2048^2 FPA for Infrared Astronomy Developmewnt Status," in *Infrared Detectors and Instrumentation for Astronomy*, A.M. Fowler, ed., *Proc. SPIE* **3354**, pp. 8-21, 1998.

[Kovács et al., 2004] Z. Kovács, U. Mall, P. Bizenberger, H. Baumeister, H.-J. Röser Characterization, testing, and operation of Omega2000 wide-field infrared camera: in *Optical and Infrared Detectors for Astronomy*, J. D. Garnett, J. W. Beletic, Eds. *Proc. SPIE* **5499**, 432-441, 2004

[Kroupa et al. 1993] P. Kroupa, C. A. Tout, G. Gilmore: 1993. The distribution of low-mass stars in the Galactic disc. *Monthly Notes R. Astron. Soc.* **322**, 231+.

[Landy & Szalay, 1993] S.D. Landy & A.S. Szalay: 1993 Bias and variance of angular correlation functions. *Astrophysical Journal* **412**, 64+

[Lilly et al. 1995] S.J. Lilly, L. Tresse, F. Hammer, D. Crampton, and O. Le Fevre: 1995. The Canada-France Redshift Survey. VI. Evolution of the Galaxy Luminosity Function to z approximately 1. *Astrophysical Journal* **455**, 108L+

[Martini, 2001] P. Martini: 2001. A Deep Multicolor Survey. VII. Extremely Red Objects and Galaxy Formation. *Astronomical Journal* **121**, 2301+

[Marzke et al., 1998] R.O. Marzke, L.N. da Costa, P.S Pellegrini, C.N.A Willmer, and J.M. Geller: 1998. The Galaxy Luminosity Function at $z \leq 0.05$: Dependence on Morphology *Astrophysical Journal* **503**, 617+

[McCarthy et al., 2001] P. J. McCarthy, R. G. Carlberg, H.-W. Chen, R. O. Marzke, A. E. Firth, R. S. Ellis, S. E. Persson, R. G. McMahon, O. Lahav, J. Wilson, P. Martini, R. G. Abraham, C. N. Sabbey, A. Oemler, D. C. Murphy, R. S. Somerville, M. G. Beckett, J. R. Lewis, and C. D. MacKay: 2001. The Las Campanas IR Survey: Early Type Galaxy Progenitors Beyond $z = 1$. *Astrophysical Journal* **560**, 131+

[Moustakas et al., 2004] L.A. Moustakas , S. Casertano, C. Conselice, M.E. Dickinson, P. Eisenhardt, H.C. Ferguson , M. Giavalisco, N.A. Grogin, A.M. Koekemoer, R.A. Lucas, B. Mobasher, C. Papovich, A. Renzini, R.S. Somerville, and D. Stern: 2004. Morphologies and Spectral Energy Distributions of Extremely Red Galaxies in the GOODS-South Field. *Astrophysical Journal* **600**, L131-L134

[Miyazaki et al., 2002] M. Miyazaki, K. Shimasaku, T. Kodama, S. Okamura, H. Furusawa, M. Ouchi, F. Nakata, M. Doi, M. Hamabe, M. Kimura, Y. Komiyama, S. Miyazaki, C. Nagashima, T. Nagata, T. Nagayama, Y. Nakajima, H. Nakaya, A. J. Pickles, S. Sato, K. Sekiguchi, M. Sekiguchi, K. Sugitani, T. Takata, M. Tamura, M. Yagi, and N. Yasuda: 2002. Evolution of Elliptical Galaxies at $z \gtrsim 1$ Revealed from a Large, Multicolor Sample of Extremely Red Objects. *Publications of the Astronomical Society of Japan* **55**, 1079

[Pei, 1992] Y. C. Pei: 1992. Interstellar dust from the Milky Way to the Magellanic Clouds. *Astrophysical Journal* **395**, 130.

[Pierini et al. 2004] D. Pierini, C. Maraston, R. Bender, and A.N. Witt: 2004. Extremely red galaxies: dust attenuation and classification. *Monthly Notes R. Astron. Soc.* **347**, 1+

[Pozzetti & Mannucci, 2000] L. , Pozetti, and F. Mannucci: 2000. Extremely red galaxies: age and dust degeneracy solved? *Monthly Notes R. Astron. Soc.* **317**, L17-L21.

[Pozzetti et al., 2003] L. Pozzetti, A. Cimatti, G. Zamorani, E. Daddi, N. Menci, A. Fontana, A. Renzini, M. Mignoli, F. Poli, P.T. Saracco, S. Broadhurst, S. Cristiani, S. D'Odorico, E. Giallongo, and R. Gilmozzi: 2003. The K20 survey. V. The evolution of the near-IR Luminosity Function. *Astronomy and Astrophysics* **402**, 837+

[Roche et al., 2003] N. Roche, J. Dunlop, and O. Almaini: 2003. The Nature, Evolution, Clustering and X-ray Properties of Extremely Red Galaxies in the CDFS/GOODS field. *Monthly Notes R. Astron. Soc.* **346**, 803+

[Röser, 2004] H.-J. Röser, "OMEGA2000 User's Manual", Heidelberg, Max-Planck-Institut für Astronomie, 2004.

[Röser & Meisenheimer, 1991] H.-J. Röser & K. Meisenheimer: 1991. The synchrotron light from the jet of 3C 273. *Astronomy and Astrophysics* **252**, 485-474.

[Rudnick et al., 2003] G. Rudnick, H.-W. Rix, M. Franx, I. Labbé, M. Blanton, E. Daddi, N.M. Förster Schreiber, A. Moorwood, H. Röttgering, and I. Trujillo: 2003. The Rest-Frame Optical Luminosity Density, Color, and Stellar Mass Density of the Universe from $z = 0$ to $z = 3$. *Astrophysical Journal* **599**, 847+

[Saracco et al., 2001] P. Saracco, E. Giallongo, S. Cristiani, S. D'Odorico, A. Fontana, A. Iovino, F. Poli, and E. Vanzella: 2001. Deep near-IR observations of the Chandra Deep Field and of the HDF-South - Color and Number Counts. *Astronomy and Astrophysics* **375**, 1+

[Smail et al., 1999] I. Smail, R.J. Ivison, J.-P. Kneib, L.L. Cowie, A.W. Blain, A.J. Barger, F.N. Owen, and G.E. Morrison: 1999. The Discovery of ERO Counterparts to Faint Submm Galaxies. *Monthly Notes R. Astron. Soc.* **308**, 1061+

[Soifer et al. 1999] B.T. Soifer, K. Matthews, G. Neugebauer, L. Armus, J.G. Cohen, S.E. Persson, and I. Smail: 1999. Near-Infrared Observations of the Extremely Red Object CL 0939+4713B: An Old Galaxy at $z \sim 1.58$? *Astrophysical Journal* **118**, 2065+

[Spinrad et al. 1997] H, Spinrad, A. Dey,D. Stern, J. Dunlop, J. Peacock, R. Jimenez, and B.T. Windhorst: 1997. An old, red Galaxy at $z = 1.552$. *Astrophysical Journal* **484**, 581+..

[Thomson et al. 1999] D. Thomson, S.V.W. Beckwith, R. Fockenbrock, J. Fried, H. Hippelein, J.-S. Huang, B. von Kuhlmann, Ch. Leinert, K. Meisenheimer, S. Phleps, H.-J. Röser, E. Thommes, and Ch. Wolf 1999. The surface density of extremely red objects. *Astrophysical Journal* **523**, 100+.

[van den Bergh et al. 2001] S. van den Bergh, J. G. Cohen, C. Crabbe: Caltech Faint Galaxy Redshift Survey XV: Classification of Galaxies with $0.2 < z < 1.1$ in the Hubble Deep Field (North) and its Flanking Fields. *Astronomical Journal* **122**, 611

[White & Frenk, 1991] S.D.M. White, and C.S. Frenk: 1991. Galaxy formation through hierarchical clustering *Astrophysical Journal* **379**, 52+

[Wolf et al. 2001] C. Wolf, K. Meisenheimer, and H.-J. Röser: 2001. Object classification in astronomical multi-color surveys *Astronomy and Astrophysics* **365**, 660+

[Wolf et al. 2003] C. Wolf, K. Meisenheimer, H.-W. Rix, A. Borch, S. Dye, and M. Kleinheinrich: 2003. The COMBO-17 survey: Evolution of the galaxy luminosity function from 25 000 galaxies with $0.2 < z < 1.2$ *Astronomy and Astrophysics* **401**, 73+

[Wolf et al. 2005] C. Wolf, M. Gray, and K. Meisenheimer: 2005. The cluster Abell 901/902 seen with COMBO-17: Dusty star-forming galaxies in the red-sequence. astro-ph/0506150

[Yan et al., 2000] L. Yan, P.J. McCarthy, R.J. Weymann, M.A. Malkan , H.I. Teplitz, L.J. Storrie-Lombardi, M. Smith, and A. Dressler: 2000. Extremely Red Objects from the NICMOS/HST Parallel Imaging Survey. *Astronomical Journal* **120**, 575+

Acknowledgements

I would like to express my special gratitude to Prof. Klaus Meisenheimer for being my supervisor for the last two years of this study.

I also acknowledge the support of my former supervisor, Dr. Hermann-Josef Röser.

I am deeply indebted to Prof. Dietrich Lemke and the directors Prof. Thomas Henning and Prof. Hans-Walter Rix for given my the opportunity to work at MPIA.

I would like to thank Christian Wolf and Siegfried Falter for their invaluable help during my study in astronomy.

I am grateful to Peter Bizenberger, Ulrich Mall, Harald Baumeister, Clemens Storz, Florian Briegel and René Fassbender for their guidance and support related to the OMEGA2000 project.

Final thanks go to Fabiola Zelada-Gonzales, Jeffrey Mark Burkhartsmeyer, and Ernest Krmpotic for their encouragement, language expertise, and helpful remarks.